Electromagnetic Nanopositioner

by

David P. Cuff

B.S., Mechanical Engineering, University of Utah (2004)

Submitted to the Department of Mechanical Engineering
in partial fulfillment of the requirements for the degree of

Master of Science in Mechanical Engineering

at the

MASSACHUSETTS INSTITUTE OF TECHNOLOGY

June 2006

Author ....
Department of Mechanical Engineering
May 19, 2006

Certified by .....
David L. Trumper
Professor of Mechanical Engineering
Thesis Supervisor

Accepted by ....
Lallit Anand
Chairman, Department Committee on Graduate Students

Electromagnetic Nanopositioner

by

David P. Cuff

Submitted to the Department of Mechanical Engineering
on May 19, 2006, in partial fulfillment of the
requirements for the degree of
Master of Science in Mechanical Engineering

Abstract

This thesis presents the analysis, design, and control of a new class of magnetic nanopositioner. Applications for this class of positioner include sample positioning for scanning microscopy and interferometry, nanofabrication, vibration cancellation, biological cell tracking/positioning, and beam focusing/steering. The nanometer-resolution positioning required in these applications is often provided using piezoelectric ceramic actuators. The drawbacks to using piezoelectric actuators include high hysteretic heating, lightly damped structural resonances, the need for preload on the actuator stack, as well as the requirement for a high voltage amplifier.

This thesis demonstrates an electromagnetically driven nanopositioner that is suspended on rubber bearings as a promising, low cost alternative to the piezoelectric nanopositioners. Several key features of the electromagnetic nanopositioner are the flux-steering actuator that applies a force linear in both coil current and displacement, replacement of the conventional metal flexures with rubber bearings, as well as power and sense electronics that can be easily integrated into a compact package. A prototype of this class of nanopositioner with 100μm of travel and a maximum force output of 460 N was built and tested. A closed-loop bandwidth of 580 Hz was obtained using capacitance distance sensor feedback.

The feasibility and procedure for casting rubber bearings was investigated. Several room-temperature vulcanizing (RTV) rubbers were considered for low volume, in-lab production of test specimens. A compression specimen was cast from a two-part RTV silicone rubber that was found to be suitable. A compression fixture that was previously used to test bonded rubber pads was modified to accept the cast rubber bearings. The cast rubber bearing was found to have the predicted DC stiffness and the stiffness increased with frequency as expected. Casting of rubber bearings was demonstrated as a feasible method for putting rubber bearings into devices such as nanopositioners.

Thesis Supervisor: David L. Trumper
Title: Professor of Mechanical Engineering

Acknowledgments

First and foremost, I would like to thank Professor Trumper. He has offered endless knowledge and patience with me as I have proceeded through this work. He has always been willing to offer a new perspective on the problems encountered and I am a much better engineer from my time working with him. He opened my eyes to many of the examples of novel thinking that we encounter everyday, yet most never stop to think about. I very much appreciate the opportunity I have had to work with him in the Precision Motion Control Lab.

Next I would like to thank Leslie Regan for her patience and the help she offered during my time at MIT. She has made many issues effortlessly and I know they would have been quite painful otherwise. I would also like to thank Laura Zaganjori and Denise Moody for helping me get the materials I needed and taking care of the paperwork I did not.

I would also like to thank the many lab rats that have toiled away with me in the PMC. These would include (in order of appearance) Rick Montesanti, Marty Byl, Aaron Mazzeo, Xiaodong Lu, Mart Corbijn van Willenswaard, Twan Thomassen, Dave Otten, Larry Hawe, Augusto Barton, Joe Cattell, Dan Kluk, Emre Armagan, Ian Mackenzie, and Kevin Miu. Many of these guys at least made me feel like I wasn't yet insane.

I would like to thank the many other students at MIT, that were taking a course with me or were suffering through one with me as TA, for always being willing to share their experience with me.

I would also like to thank the many members of my family and my in-laws. They have been a great source of support over the years and I am very grateful for it.

Finally, I would like to thank my wife Heidi for joining me on many adventures, putting up with our first year apart, and continuing to find new adventures for us.

THIS PAGE INTENTIONALLY LEFT BLANK

Contents

List of Figures

THIS PAGE INTENTIONALLY LEFT BLANK

List of Tables

THIS PAGE INTENTIONALLY LEFT BLANK

Chapter 1

Introduction

The advancements of nanotechnology have proliferated into nearly all fields of science within the last decade. This spread has increased the need for devices that can be used to observe or interact with mechanisms and events at the nanoscale. Generally, devices that operate at these small scales are expensive which prevents some researchers from being able to fully explore their science [16].

The new class of nanopositioner developed in this thesis presents a solution to the prohibitive cost of nanopositioning devices by employing low cost bearing systems, solid magnetic material construction, requires minimal control processing power, and utilizes low voltage amplifiers. It is expected this new class of nanopositioner will be applicable in a large variety of devices currently served by piezoelectric devices, which require large, high voltage amplifiers and expensive motion guidance systems.

Several results of this thesis that are useful for constructing this new class of nanopositioner include the rubber bearing casting technique, the electromagnetic actuator configuration, and the bearing/actuator packaging of the single degrees of freedom (DOF) demonstration positioner. What may be considered the lower bound on system performance for these nanopositioners is also presented and demonstrates the high level of promise for allowing further proliferation of nanotechnology in science through low cost access to necessary equipment.

1.1 Background

This section will serve as a brief introduction to nanopositioning and present the natural extensions to the technologies most relevant to this thesis. The first topic to be covered is drawbacks of piezoelectric actuation. The next topic is metal flexures, followed by a brief discussion of rubber bearings and how they solve some of the issues presented by metal flexures.

1.1.1 Nanopositioning

A critical concept in nanopositioning systems is that, in general, all six DOF must be constrained. Current nanopositioning systems typically approach the task from either a fully-actuated approach where all six DOF are controlled in static or low-frequency operation or from a constrained-motion approach where unactuated DOF are constrained by bearing systems. The constrained-motion approach limits the number of actuators/sensors needed in applications that do not require active control in all six DOF. The proposed new class of nanopositioner would fall under the constrained motion approach. Chapter 2.1 presents many examples of nanopositioners that fall into both categories of positioning systems.

Applications for the new class of positioner in this thesis include sample positioning for scanning microscopy and interferometry, nanofabrication, vibration cancellation, biological cell tracking/positioning, and beam focusing/steering. The nanometer-resolution positioning required in these applications is often provided using piezoelectric ceramic actuators. The drawbacks to using piezoelectric actuators include high hysteretic heating, intolerance to bending moments, lightly damped structural resonances, the need for preload on the actuator stack, as well as the requirement for a high voltage amplifier.

1.1.2 Piezoelectric Actuation

The high hysteretic heating of the piezoelectric actuator occurs at high operating frequencies and becomes a thermal source in the precision machine. The associated

thermal deformations can lead to positioning errors, actuator damage, or may require limited high frequency operation and possibly an active cooling system. The piezoelectric actuator also requires contact with the specimen being positioned. This contact provides a direct heat transfer path from the actuator to the specimen if protective design features are not included.

Lightly damped structural resonances limit the maximum frequency at which the positioner may operate as trying to control the actuator near resonance will put the crystal under tensile loading. Piezoelectric actuators are very sensitive to tensile loads and could be destroyed. Magnetic actuators enable control of positioners above structural resonances as long as the structure of the positioner can tolerate passing through the resonance.

The bearing system for nanopositioners utilizing piezoelectric drives must eliminate bending loads on the drive, while preloading the it. This actuator preload allows a pull force to be applied to the stage while not allowing a tensile load on the piezoelectric stack. The bearing solution often implemented requires wire electrical discharge machining (EDM), that increases the system manufacturing cost. The rubber bearing alternative presented in this thesis has the potential to replace these more expensive bearing systems in many applications, although the wire EDM bearing system would continue to be used in harsh/high-temperature environments that rubber is ill-suited to endure.

A major drawback to piezoelectric systems is the expensive, high voltage amplifier required for operation. A single DOF, piezoelectrically actuated nanopositioner with 120 μm of travel is commercially available for \$1700 and requires a \$5400 high voltage amplifier [26]. The amplifier costs over three times as much as the positioner itself, while the amplifier for an equivalent electromagnetic actuator would be around \$100.

1.1.3 Flexures

The elastic deflection of materials can be used to provide guided motion without the disadvantages of rolling or sliding bearing systems such as friction, stiction, and vibration. Systems that provide motion guidance through the stretching of a rela-

tively compliant member are referred to as flexures. Flexure systems have become a ubiquitous technology and can be found in precision machines for manufacturing or measurement, as well as sporting goods and automobiles. To date, the dominant material for flexure systems in precision machines has been metals, typically spring steel; although this body of work will show rubber flexures also have a place in precision machines.

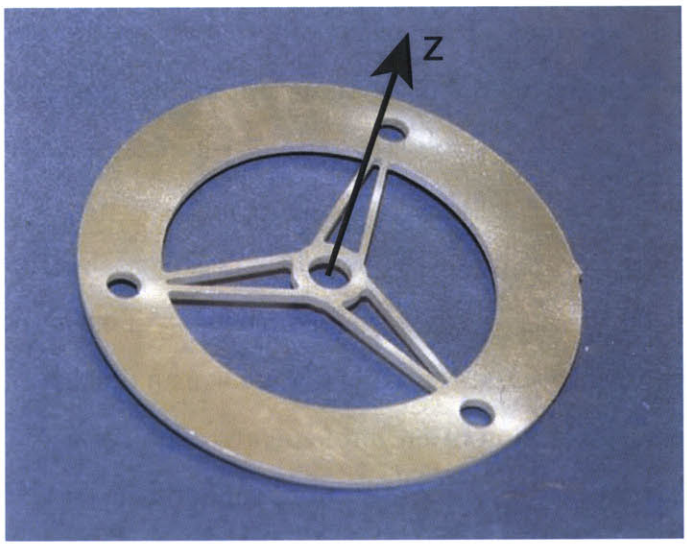

Figure 1-1: Prototypical axially-compliant flexure which constrains three DOF.

Typical metal flexures consist of long, wire-like beams that are only stiff in tension. An example of such a metal flexure in shown in Figure 1-1. This flexure constrains the motion of the center hub from translating perpendicularly to the shown z-axis and also from rotating about the z-axis. Several disadvantages of this style of flexure include sensitivity to overload as permanent deformation occurs at relatively low strains, structural resonances due to the flexible wire-like structure and low damping of the structural metals, and the large area needed to accommodate a flexure that has little travel.

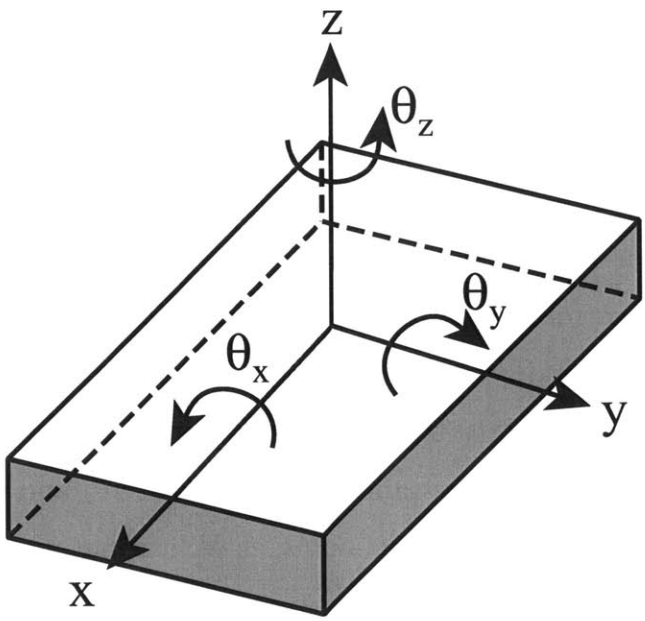

Figure 1-2: Displays the 6 degrees of freedom of a rubber sheet.

An interesting alternative to the metal flexures are elastomeric flexures or rubber bearings. The typical structure of rubber bearings involves a rubber pad, as shown in Figure 1-2, being sandwiched between two rigid plates. The plates would be placed against the two faces of the rubber sheet lying in the xy-plane. The compliant motions of the rigid plates relative to one another with reference to the coordinates of the figure, could be a rotation, θ_z, or translations in the x- or y-directions. While the constrained motions would be translation in the z-direction or rotations about the x- and y- axes.

One important question yet to be discussed is what determines whether an axis is constrained or compliant. The determination of constraint versus compliance for a flexure system is found by comparing the stiffness of the flexure in one direction to the expected forces that will cause deflection in that direction. Rivin found the compression-to-shear stiffness ratio for ultra thin sheets of rubber to approach 1000 as the layer thickness approached 0.1mm [41]. This translates into the rubber sheet shown in Figure 3-6 allowing a displacement 1000 times greater in the x-

or y-directions than in the z-direction for the same force. The terminology to describe this situation is that the x- and y-direction are compliant and the z-direction being constrained. These compliance determinations may not apply in cases where forces in one direction are several orders of magnitude greater than forces in the other directions.

The determination of compliant versus constrained for θ_x, θ_y, and θ_z can proceed by realizing that these rotations are a reflection of compression and shear of the rubber about the x-, y-, and z-axes. The rotations θ_x and θ_y cause a tilting load on the bearing that causes half of the bearing to be in compression, while the other have is in tension. So the bearing is constraining motions in the θ_x and θ_y directions. The bearing will be compliant for rotations about θ_z as the it is put under a shear loading.

1.2 Thesis Overview

A few basic principles of nanopositioning were covered in the previous section of Chapter 1. Chapter 2 will introduce more concepts important in nanopositioning through a review of prior art nanopositioners and their performance. Prior art electromagnetic configurations and applications of the rubber bearing concept in a number of diverse fields will also be covered in Chapter 2. A strong foundation in the analysis of rubber bearing configurations will be established in Chapter 3. This foundation will allow one to determine the stiffness of an object suspended in all six DOF by rectangular rubber bearings. The principles involved in analyzing flux-steering actuators with permanent magnet biases will be presented in Chapter 4. The goal of presenting these principles is to allow one to determine the force as a function of current and position of these actuators, as well as the voltage relations needed to properly size an amplifier.

The following subsections will present the primary content of Chapters 5 through 7.

1.2.1 Casting Rubber Bearings

An investigation of cast in-place rubber bearings is given in Chapter 5. These cast rubber bearings are formed by filling the volume between two rigid supports with a liquid rubber and allowing it to vulcanize and adhere to the supports. Casting bearings directly in-place has many advantages which include good adhesion, can conform to any surface geometry, is a scalable production method, and a wide variety of liquid rubber materials are available. The apparatus designed for casting a rubber bearing is shown in Figure 1-3 with the four valves across the front panel, the liquid rubber reservoir, the overflow chamber front left, and the mold in the back. The casting system employed a single vacuum pump and only required disposal of plastic tubing, a plastic cup, and a plastic overflow liner each time a bearing was cast. Figure 1-4 shows the bearing in the compression test fixture configuration ready to be tested. The test results show the casting process can produce a quality rubber bearing.

Figure 1-3: Physical implementation of the bearing casting apparatus.

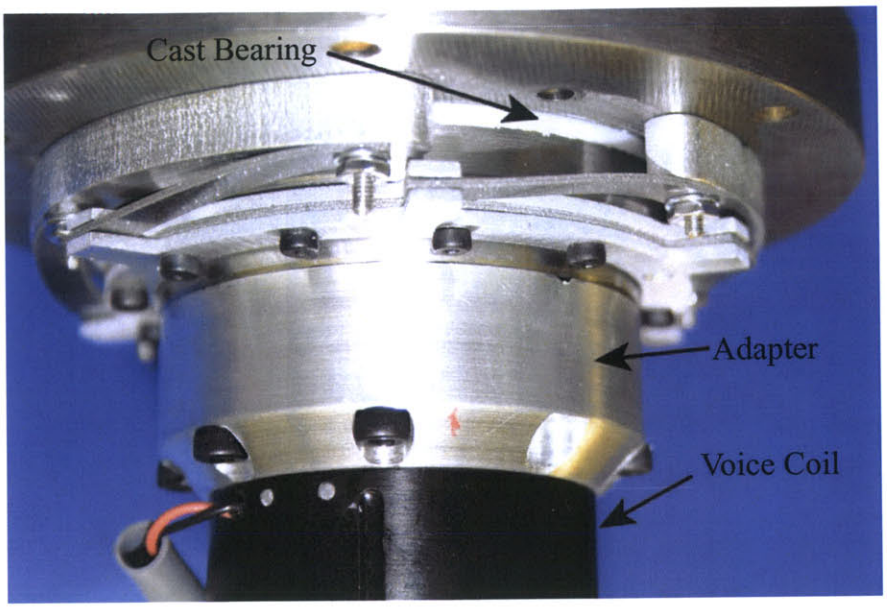

Figure 1-4: Photo of the cast rubber bearing in the compression configuration for testing.

1.2.2 Nanopositioner Design

The nanopositioner design details are presented in Chapter 6 starting with an investigation of an o-ring stacking concept for constructing a rubber bearing. The result of this investigation was that an o-ring stacking construction technique would only provide sufficient stiffness in a precision machine application if there were bulging interference between adjacent o-rings. Following this investigation is a comparison of several hard-linearized magnet actuator configurations. The best configuration for this nanopositioning application was suggested by Professor Trumper and is shown in Figure 1-5. The selected magnetic configuration provided very compact packaging of the permanent magnets, coils, rubber bearings, and support structures, as shown in Figure 1-6. The nanopositioner was designed to provide 680 N of force for a current of ± 4 A from a total nanopositioner package 42 mm x 35 mm x 35 mm.

Other topics covered in Chapter 6 are the force as a function of current and displacement, stage stiffness in all six DOF, modeling the magnetic and mechanical stiffnesses together, and several alternative nanopositioner concepts.

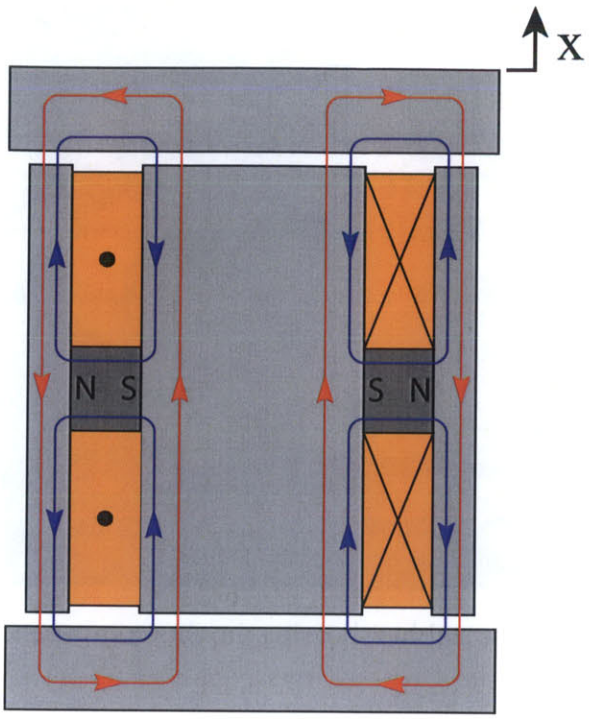

Figure 1-5: Diagram of the coil and magnetic flux paths in the nanopositioner.

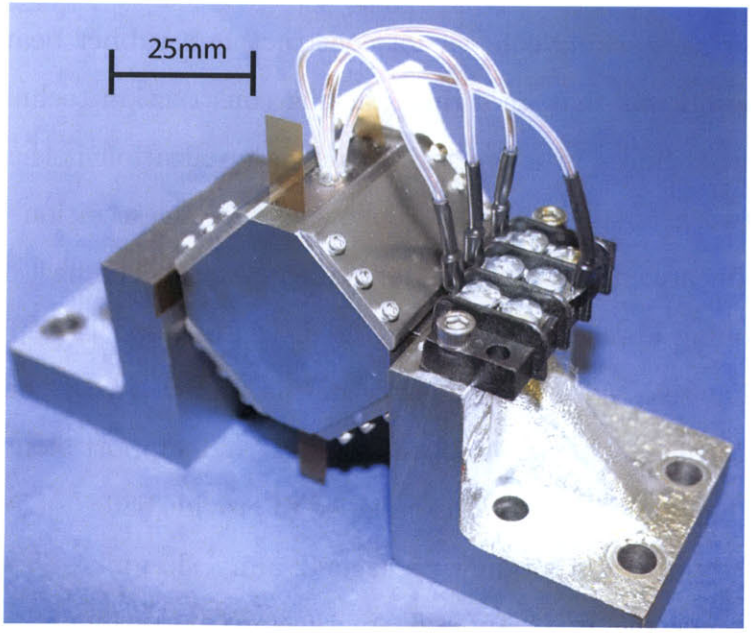

Figure 1-6: Photo of the fully assembled nanopositioner with shims still in the air gaps.

1.2.3 Nanopositioner Control

The control system configuration and system performance are presented in Chapter 7. The final system performance had a maximum force output of 460 N and a system bandwidth of 580 Hz. Figure 1-7 is a comparison of the open loop frequency response measured by both laser interferometry and capacitance gage feedback. The capacitance gage feedback response was much more smooth and was the motivation for permanently changing the position sensor from the laser interferometer to the capacitance gage. The final closed-loop system response is shown in Figure 1-8

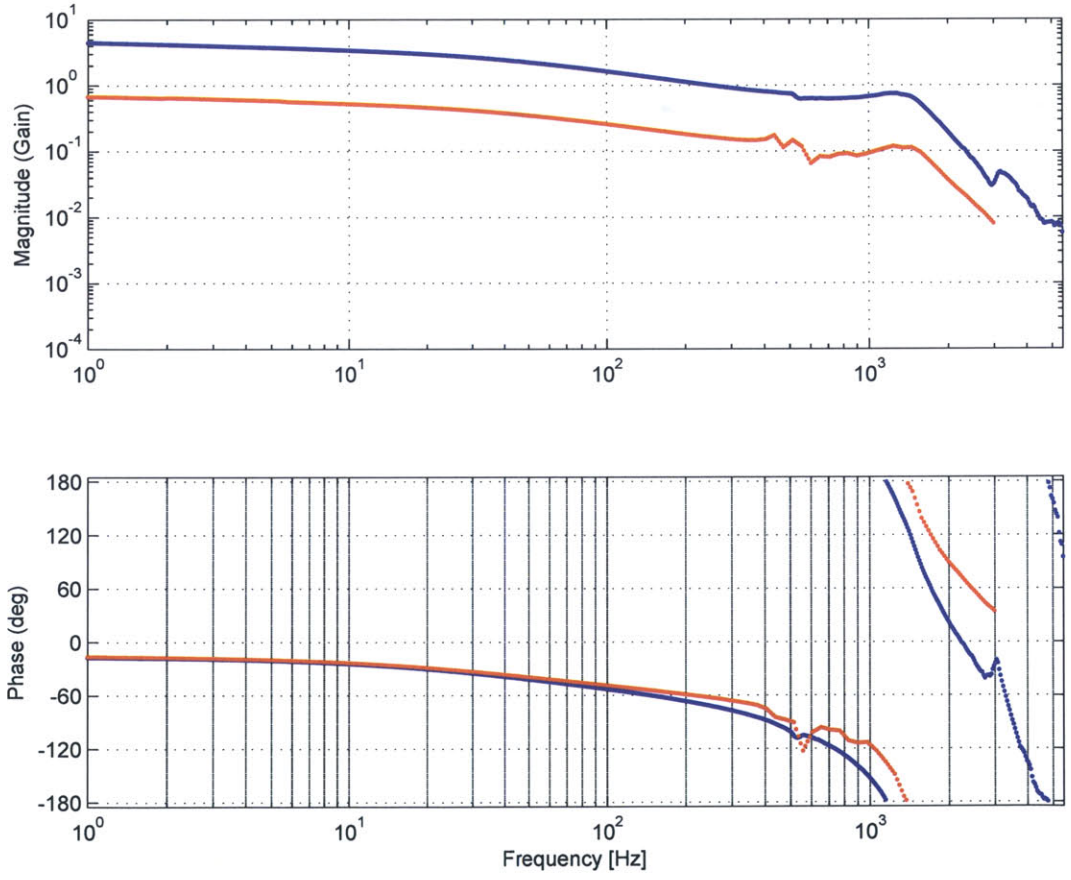

Figure 1-7: Comparison of the open-loop plants acquired by laser interferometry (red) and capacitance gage (blue) feedback.

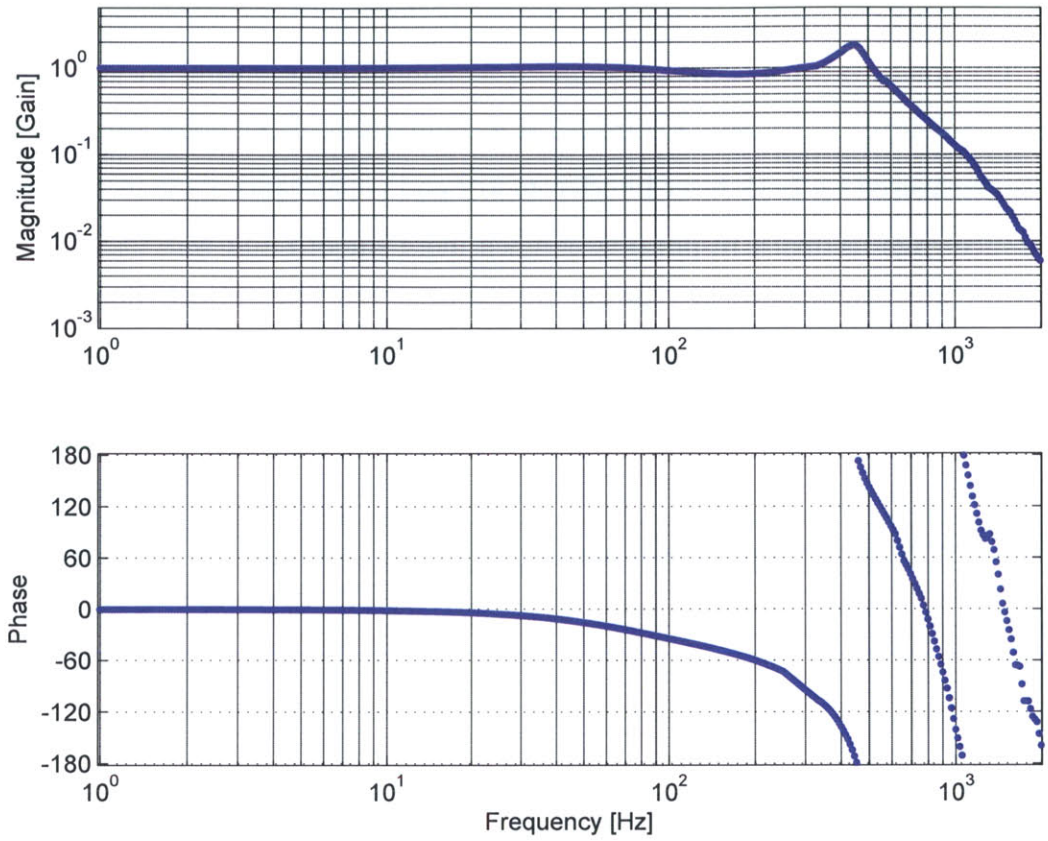

Figure 1-8: Plot of the final closed-loop system response.

Other issues addressed in Chapter 7 are two integral-lead compensator designs, an alternative block diagram implementation of the integral-lead compensator that allows anti-windup limits to be placed on only the integral term, presentation of a 1 μm and 4 μm step responses, and two positioner trajectories that demonstrate the hysteresis in the system.

Chapter 2

Literature Review

The prior art relevant to the new class of nanopositioner is reviewed in this chapter. This includes different types of actuation available for nanopositioning, information on magnetic actuation configurations, and the history and applications of rubber and rubber bearings in modern machines.

2.1 Nanopositioning Prior Art

Many different methods for classifying current nanopositioning systems could be used and this section classifies them according to the method of actuation. Nanopositioners utilizing a magnetic actuator in either a normal-stress configuration, shear-stress configuration, or Lorenz force configuration are reviewed first. Three common forms of piezoelectrically driven positioners will then be reviewed with emphasis on the performance trade-offs associated with these positioners. Alternative actuation methods are briefly presented and for more information see the following references [24, 46].

2.1.1 Magnetic Devices

Elimination of mechanical connection between inertial ground and the positioning stage is a direction many magnetically driven stages have taken. This approach has advantages such as stage stiffness can be infinite at low frequencies, elimination of

mechanical wear, and decoupled control in all six DOF is possible.

A magnetic linear bearing suspension that utilized seven magnetic actuators to constrain the bearing in five DOF was developed by Trumper [52]. Analog controllers were designed to push the crossover on the stage roll, pitch, and heave control loops over 100 Hz. The actuators used were in a permanent magnet biased, normal-stress configuration with independent magnetic circuits for the permanent magnet and coil fluxes. The sixth stage DOF would allow up to 50 mm of travel with a position stability of 5 nm peak-to-peak in the other five DOF, which was the highest position stability demonstrated in a magnetic suspension at that time.

Sub-nanometer positioning noise was achieved with the development of the Angstrom Stage [36, 23]. The extremely low level of positioning noise was achieved by floating the positioning stage in oil, decoupling each of the six stage DOF through feedback linearization, and implementation of a bias estimator that used a detailed plant model to predict disturbance forces. Actuation was achieved using 12 electromagnets in standard E-I magnetic core pairs with 50 N force capability. The resulting system had a 6σ peak-to-peak positioning noise of 0.3 nm when position measurements were taken with a 1 Hz sensor bandwidth.

While the previous nanopositioning systems relied on magnetic actuators for the non-contact suspension of the stage, Chen utilized metal flexures in addition to six electromagnets for positioning in three DOF (x, y and θ_z) [5]. The advantages of metal flexures in this work was to increase the system natural frequency, disturbance rejection, and system bandwidth over an equivalent magnetically levitated system by increasing system stiffness in the controlled DOF mechanically. The steel flexures provided very little damping so viscous damping was added by designing a parallel disk shear damper into the stage. Motions of the stage in the three controlled directions result in shearing of a high viscosity oil that fills a gap between mechanical ground and the disk attached to the stage. This nanopositioning system achieved a system bandwidth of 90 Hz with 100 μm of travel in x- and y-directions and ± 2.2 milliradians in θ_z.

An example of a magnetically actuated stage that utilizes a shear configuration was

developed by Kim to provide all stage movement required for photolithography [29]. Four Halbach permanent magnet arrays provided magnetic flux for the operation of four, three-phase linear motors that are mounted to mechanical ground. The positioner had a planar travel range of 50 mm square with vertical range of ± 200 μm and a maximum stage acceleration of 10 m/s^2 with the laser interferometer slew rate limiting the maximum velocity to 254 mm/s.

Other researchers have focused on six DOF compliant mechanisms that can be employed for quasi-static manipulations while maintaining low cost. One such device is the *HexFlex*^{TM} developed for precision fiber optic alignment at a cost of US$2000 [12]. These positioners utilize open-loop control of normal stress magnetic actuators without iron cores to produce small and highly predictable displacements of the stage on the flexure suspension.

A five DOF, flexure based micropositioner that utilized Lorentz, moving coil type actuators was developed by Wang [54]. The 12-bit D/A board is cited as being the most significant limitation that results in open-loop resolution of 50 nm in the x- and y-directions and 150 nm in the z-direction. The closed-loop system resolution was found to be 0.3 μm in translation and 2.73 x 10^{-6} radians in rotation. The maximum force available to deflect the flexures and move the payload is 3.7 N in the x-direction.

2.1.2 Piezoelectric Devices

Piezoelectric actuators are typically integrated into positioning systems in one of three basic designs: direct-drive, use of travel amplifying levers, or in less conventional long-travel configurations.

Commercially available piezoelectrically actuated nanopositioning stages are available that utilize either the direct drive or lever configurations to generate the desired displacements [26]. Some literature refers to both of these basic designs as elastic deformation stages. Common characteristics of the direct drive configuration include minimal parasitic motions, limited travel, higher force capability, higher stiffness and higher resolution for a given amplifier. The higher stiffness in the controlled direction results in a higher system resonant frequency and useable system bandwidth is on

the order of 1/4 to 1/3 of the resonant frequency in commercial systems [27].

Travel amplification can be achieved using levers at the expense of force capability, stiffness, and bandwidth. The system stiffness is the piezoelectric element stiffness divided by the lever transmission ratio squared in addition to the lever stiffness which can be modeled as a second spring in series with the system stiffness. The Physik Instrumente product catalog has much more information on lever and direct driven nanopositioners for those interested [26].

The third design category for piezoelectric positioners are long-travel configuration and can be further divided into stick-slip friction drives and clamp-release inchworm drives. An example of each of these long-travel configurations are now presented.

A long-travel nanopositioning stage was developed by Chu that could operate in either a scanning mode or stepping mode [7]. The straightness of the 10 mm of stage motion is provided by running along two high-precision cylindrical guide rails. The piezoelectric actuator acts as an elastic deformation actuator to move the stage through displacements less than 50 μm with a resolution of 10 nm. The long-travel of the stage is provided by passing a 100 V sawtooth waveform to the piezoelectric stack. A friction tip "sticks" to the stage on the slowly rising ramp and "slips" on the sudden drop from 100 V to 0 V. When the slip occurs the stack moves approximately 35 μm relative to the friction tip along the guide rails.

The inchworm pursued by Tenzer was composed of two piezoelectric actuators that alternately clamp the moving stage to a guide rail, while a third actuator moves the unclamped actuator relative to the clamped actuator [51]. Two drawbacks to the inchworm configuration is discontinuous motion and reduced system stiffness. The system stiffness is reduced as the contact stiffness of the clamped actuator to the guide rail and the third actuator stiffness are placed in series. An obvious advantage is that travel is only limited by the length of the guide way.

2.1.3 Other Actuation Methods

Magnetic and piezoelectric actuation is the method most often used in macroscopic machines where larger forces and machine volumes are necessary. Other types of

actuation become attractive as the machine size and force requirements decrease such as electrostatic and thermal mechanical actuators.

An example of how a thermal mechanical actuator (TMA) can replace an electromagnetic actuator as the device size decreases is presented in the μHexFlex [6]. The *HexFlex*^{TM} Project presented in Section 2.1.1 utilized electromagnetic actuators that were separate assemblies, while the TMA's employed in the μHexFlex were integrated directly on the μHexFlex during deep reactive ion etching fabrication. The resulting device had natural frequencies above 4 kHz, an actuator bandwidth of 100 Hz, a device sensitivity of 10 Å/mV, and a device range of approximately 10 μm and 20 mrad in the three translational and rotational DOF, respectively. Although the actuator and mechanical structure are not ideal compliments, this work shows TMA are a viable actuation technology as the machine scale decreases.

2.2 Electromagnetic Actuator Prior Art

The class of electromagnetic actuators of the most utility for positioning applications that require high forces and relatively short strokes are hard-linearized, normal-stress configurations that apply a force that is linear in both current and position[1]. Excellent reviews of flux-steering actuators and hard-linearized configurations are provided by Montesanti and Lu in their theses on fast-tool servos [38, 35].

The prior art configuration most relevant to the work in this thesis is provided by Studer in a design for a radial magnetic bearing [47]. The permanent magnet provided equal biasing fluxes to both gaps when the rotor was in the centered position. Deviations from the centered position would be corrected by passing a current through the coil so as to increase the magnetic flux through the larger gap and decrease the flux through the smaller gap. The flux imbalance creates a restoring force that pulls the rotor back to the centered position. Figure 2-1 shows the permanent magnet bias flux in blue and the coil flux for a positive coil current in red. Note that for the positive current direction of Figure 2-1 the flux addition occurs in the right gap and

[1]Further explanations of hard-linearized electromagnetic actuator found in Section 6.2.

flux subtraction occurs in the left gap resulting in a force that pulls the rotor to the left relative to the stator.

Studer's magnetic configuration gives a force that is linear in current and linear in position as a result of the invariant total gap length, constant permanent magnet biasing flux, differential excitation, and natural subtraction, which are all features Lu [35] gave as characteristics of the hard-linearized magnetic actuator configurations.

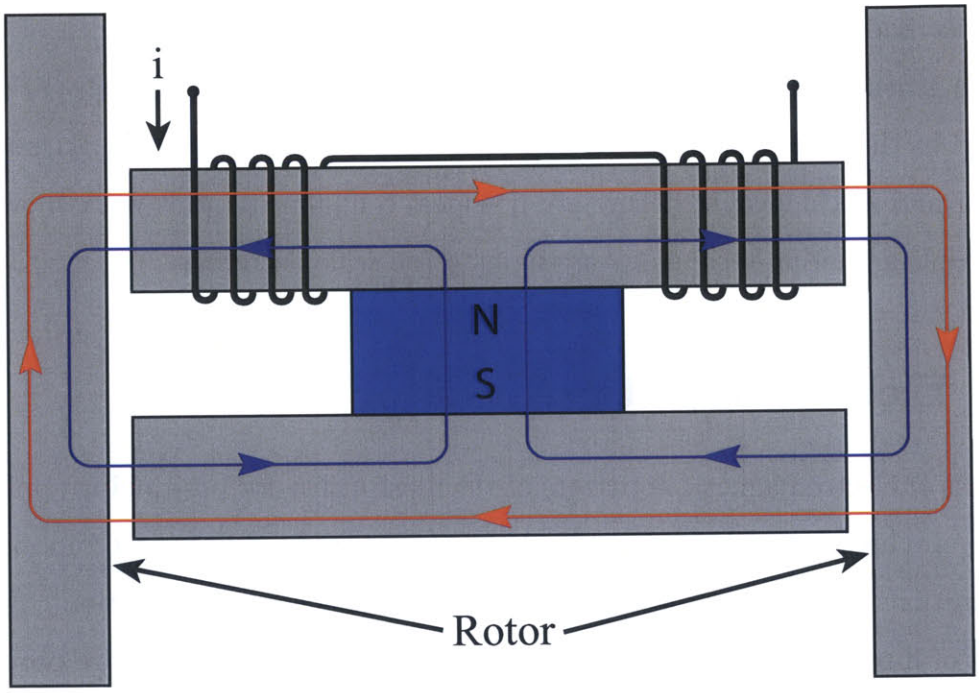

Figure 2-1: Hard-linearized magnetic configuration proposed by Studer where the force is linear in current and position [47].

2.3 Rubber Bearings Prior Art

Rubber has been applied as a motion guidance system in a number of diverse devices in industries ranging from aerospace and automotive to precision machines. This section reviews these diverse applications, including the varied naming conventions each industry employs.

2.3.1 Structure Support

Rubber bearings have been used as support and isolation systems for bridges, heavy machinery, and buildings since the 1960's. An early, failed attempt to isolate a 40-story building from ground vibrations caused by Grand Central Station was constructed in 1915 [17]. The building was mounted on a lead/asbestos composite structure which was much too stiff to reduce the ground vibration transmitted to the building. It wasn't until the 1960's that increased traffic congestion and land scarcity in industrial cities forced a renewed interest in building isolation.

Albany Court in London, England was apparently the first building to be successfully isolated from ground vibrations. Albany Court was an apartment building constructed in 1966 directly above the St. James' Park Station of the London Underground [30]. Many ground vibration isolation projects have been completed since Albany Court and have included for instance a concert hall in Glasgow, Scotland and the International Convention Center in Birmingham, England [30].

Rubber bearings have also been used to create earthquake-resistant buildings in many earthquake-prone regions. The first use of rubber bearings for protecting a building from seismic activity is reported to be at an elementary school in Skopje, Macedonia with construction completed in 1969 [30]. The school rests on large blocks of unreinforced natural rubber. During an earthquake, the school will oscillate up and down as well as side to side because the vertical and horizontal stiffness of the bearings are nearly the same. Today, rubber bearings for limiting seismic damage are designed to have a high vertical stiffness to support the load, while having a low horizontal stiffness to decouple the building from the ground motion. The low horizontal stiffness of the isolator is to ensure the first dynamic mode of the structure only involves deformation of the isolator. The dynamic modes of the upper building structure are then subject to much lower excitation displacements due to the -2 dec/dec rolloff of the first mode. The amplitude of the excitation to the higher modes of the flexible structure are then reduced.

The first seismically isolated building in the United States is reported to be the

Foothill Communities Law and Justice Center (FCLJC) in Rancho Cucamonga, CA shich was completed in 1985 [9]. Several other buildings have since been built or retrofitted with seismic isolation in California including Oakland City Hall, Los Angeles City Hall, and the Los Angeles County Fire Command and Control Facility.

A modern seismic isolation bearing can support a 1600 kN axial load, with a diameter approaching 1 m, shape factor around 30, while composed of 30+ laminated layers of rubber and steel [9, 31]. The high shape factor causes the bearing to be almost rigid in the axial direction, while allowing nearly 50 percent strain in the lateral directions. The rubber compounds used are often either a high damping formulation or a special formulation that has relatively high shear modulus at low strain, low modulus at moderate strains, followed by a rapid stiffening at high strains to prevent the isolated building from oscillating at too high an amplitude.

Multiple issues involved in bridge design also drove increased interest in rubber bearings for bridges. Advancements in braking, acceleration, and payload capacity for large trucks, as well as building bridges with larger spans between supports pressed the roller bearings previously used for bridge support beyond their limits in many applications [17]. A primary bridge design challenge is the need to minimize forces in the superstructure and supports while accommodating bridge expansion/contraction, rotation due to bending of bridge elements, as well as supporting varying loads due to vehicle traffic. Rubber bearing design has evolved to the point that only bridge applications requiring very low horizontal stiffness use the alternative sliding bearing composed of PTFE and stainless steel.

2.3.2 Helicopter Rotor Hub

Another practical application of rubber bearings has been in the rotor hub of helicopters. The rotor blades of a helicopter in flight undergo high loads in conjunction with a complex series of rotations that can be nicely accommodated by combinations of laminated bearings. Antifriction (roller) bearings were originally used to provide the guided motion needed with the drawbacks of short lifetime of service, required frequent servicing, and were relatively heavy compared to a similar rubber

bearings [13, 17, 21].

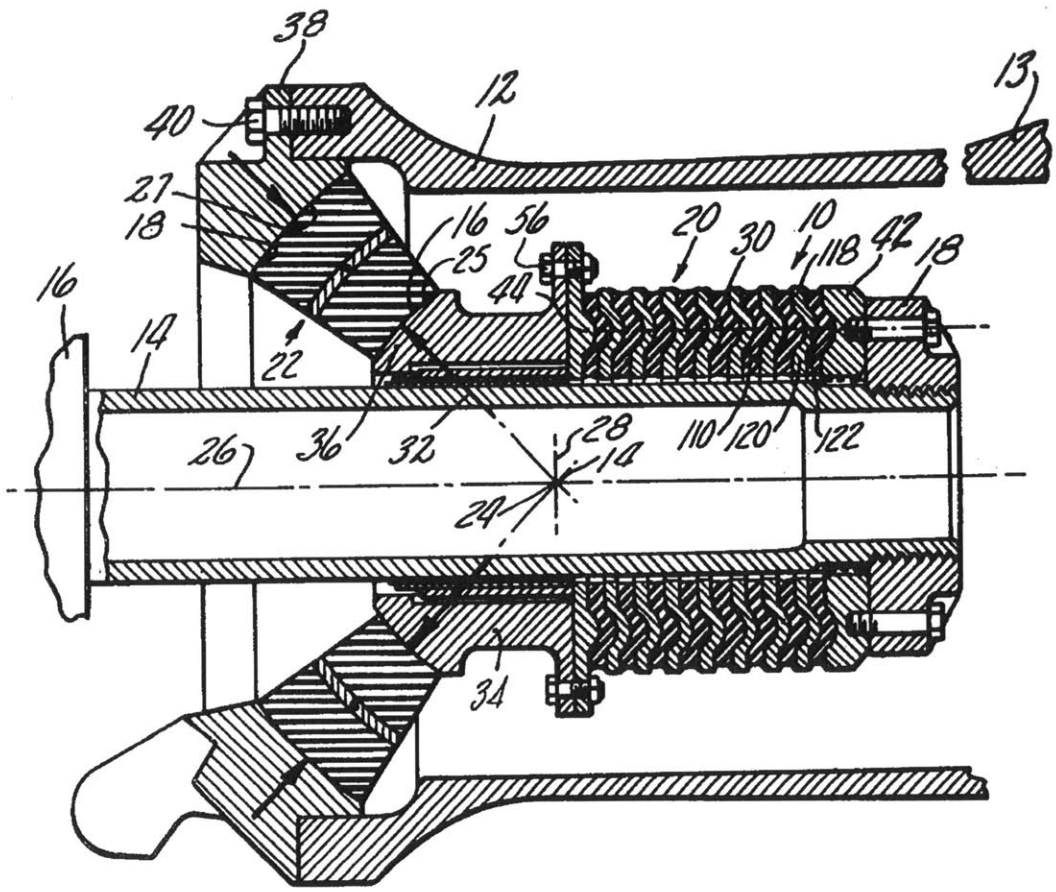

Figure 2-2: Configuration of rubber bearings employed as a rotor hub bearing that allows pitch, flapping, and lead-lag rotations [43].

However, early efforts to replace the antifriction bearing with laminated rubber bearings were met with failure of the metal shims used in the laminations [43]. It was determined the stresses causing the failure were from eccentricity of the rotor reaction forces and a correction of this eccentricity would solve one of the primary difficulties in the use of laminated rubber bearings. This eccentricity was found to be present in many of the early efforts to design rubber bearings for use in rotor hubs. Rybicki [43] presented one particular implementation of a spherical rubber bearing where the centers of hydrostatic pressure in the rubber from each side of the bearing are not aligned and result in a moment applied to the laminate. Figure 2-3

demonstrates the correct practice for laminated rubber bearing design as presented by Rybicki [43].

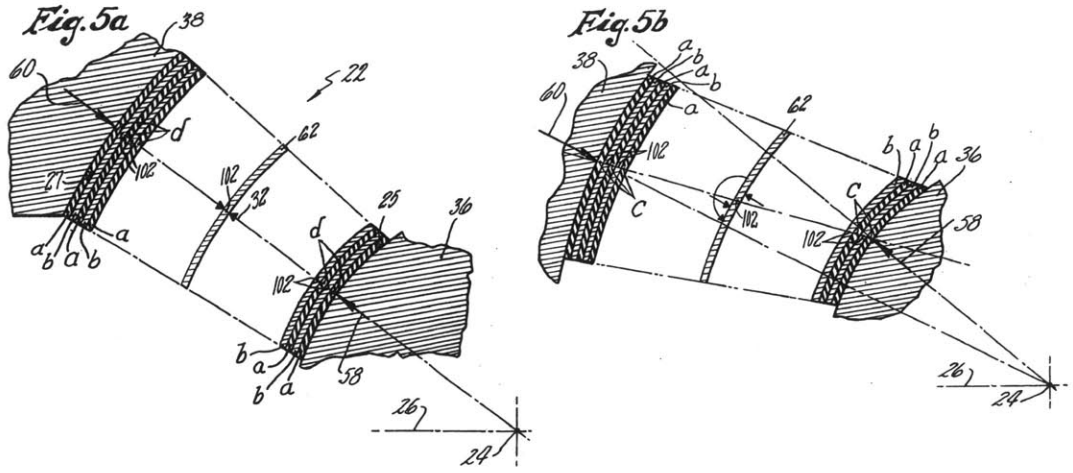

Figure 2-3: Fig. 5a and 5b demonstrates the proper and improper alignment of the centers of hydrostatic pressure in bearing laminates [43].

A Boeing Company news release from 1999 stated:

> The current CH-47D rotor hub was designed with significant growth capability but contains 400 parts in the hub system assembly, including nine critical bearings that require lubrication. These bearings contain drain points that allow lubricants to escape, requiring inspection, repair and replacement of seals and other parts while creating additional support and operating costs.
>
> The new technology design, used on other advanced rotorcraft such as the Boeing AH-64D Apache Longbow and the Boeing Sikorsky RAH-66 Comanche armed reconnaissance helicopter, replaces lubricated or "wet" bearings with elastomeric "dry" bearings that require no additional lubrication. The elastomeric rotor hub eliminates at least 10 days of unscheduled maintenance each year for every Chinook fielded with the new system [10].

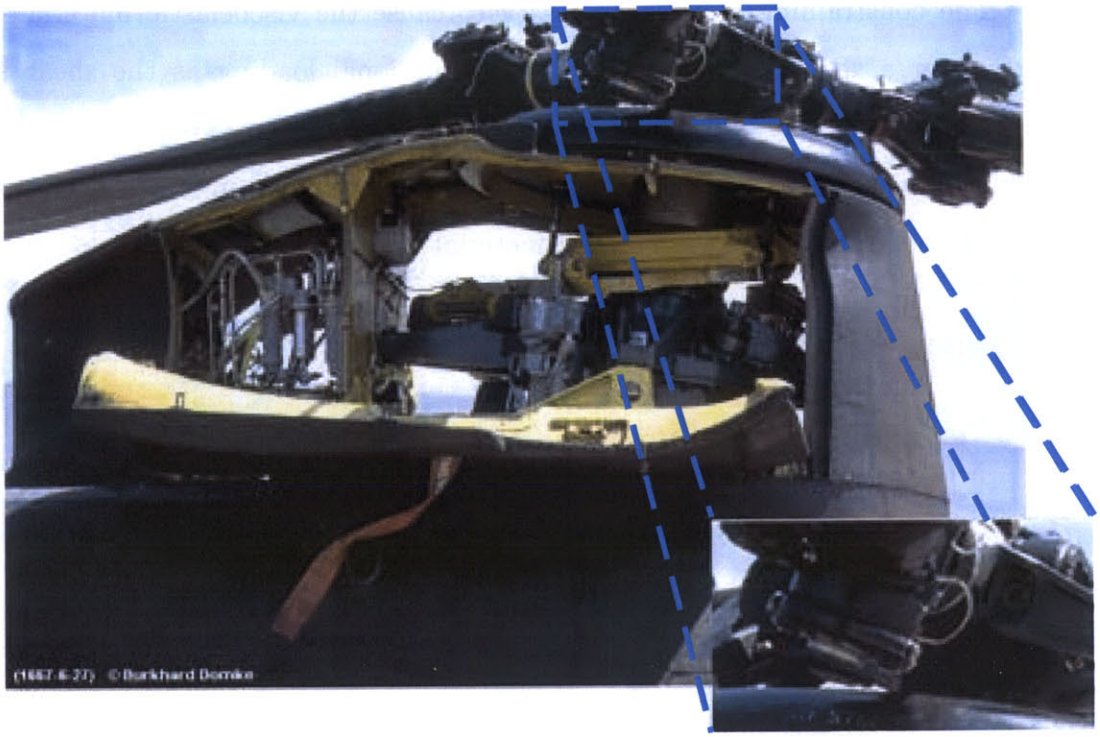

Figure 2-4: Photo of the "wet" bearing system of the CH-47D Chinook front rotor hub. Photo courtesy of Burkhard Domke.

The original roller bearing rotor hub of the Chinook is shown in Figure 2-4. The inset allows close examination of the rotor hub at the blade attachment which shows the oil lines required for keeping the previous generation lead/lag roller bearing submerged in oil.

2.3.3 Precision Machines

Typical precision machines are composed of extremely rigid elements of steel, aluminum, or other metals, all of which have very low internal damping. Typical methods for increasing the damping in precision machines include viscoelastic constrained-layer damping, tuned-mass damping, and squeeze-film damping [20]. Only the constrained-layer damper will be discussed here as it is pertinent to this body of work.

Constrained-layer dampers are constructed by sandwiching a viscoelastic material

between the structure that needs damping and another relatively rigid constraining layer. The constraining layer is necessary to cause the viscoelastic material to be placed under a shear loading rather than extensional loading as the shear strain provides higher levels of damping [17]. Figure 2-5 demonstrates how the constraining layer promotes shear in the viscoelastic material that results in strain energy being released as heat due to the viscoelastic material hysteresis.

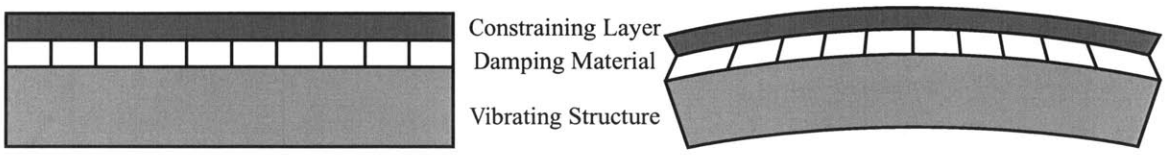

Figure 2-5: Configuration and deformation of constrained-layer damper.

Rivin describes many applications of rubber sheets in precision machines where the relative compliance of the rubber is useful in smoothing power transmission and accommodating motor/gearbox misalignment [42]. A more complex rubber mechanism for accommodating motor/gearbox misalignments was developed by Sweeney that provides dual spring rates that are each linear while limiting the maximum torque through the coupling [49]. This coupling is novel in that each rubber spring is placed in shear resulting in dual linear spring rates. Prior art in this field often employed rubber in shear to provide a low-stiffness, linear spring with rubber overload pads that would be loaded in compression (nonlinear).

An accessory to some extremely high precision machines that employs rubber in a critical fashion is the STACIS® 2100 Piezoelectric Vibration Control System [44, 3]. The STACIS system has three mutually perpendicular piezoelectric actuators that enable active vibration isolation in x-, y-, and z-directions. A critical issue arises when these three piezoelectric actuators, which are very intolerant to bending loads, are attached to the same rigid object while controlling perpendicular axes. The normal force applied by one actuator would appear as bending loads on the other two, unless the motion is decoupled by a medium that is stiff in compression and compliant in shear. This issue was solved through the use of high shape factor rubber bearings

that can stiffly support the normal force applied by each actuator while remaining compliant in the other two actuators controlled DOF.

A second novel use of rubber in the STACIS system is to couple an intermediate mass within the isolator to the payload mass. This feature is key to enabling higher system performance than prior art active vibration isolation systems. See the following reference for a in-depth discussion of the prior art problem and rubber spring solution [44].

2.3.4 Passive Vibration Isolation

The field of passive vibration isolation takes a different approach than rubber stiffness in designing rubber elements. The frequency axis of the system response is normalized by the driving frequency while the vibration amplitude is modified to a transmissibility. Transmissibility is the ratio of transmitted vibration amplitude to imposed vibration amplitude for fixed displacement systems or the ratio of transmitted force to the imposed force for fixed force systems. Figure 2-6 presents plots of transmissibility with the frequency axis normalized by the driving frequency.

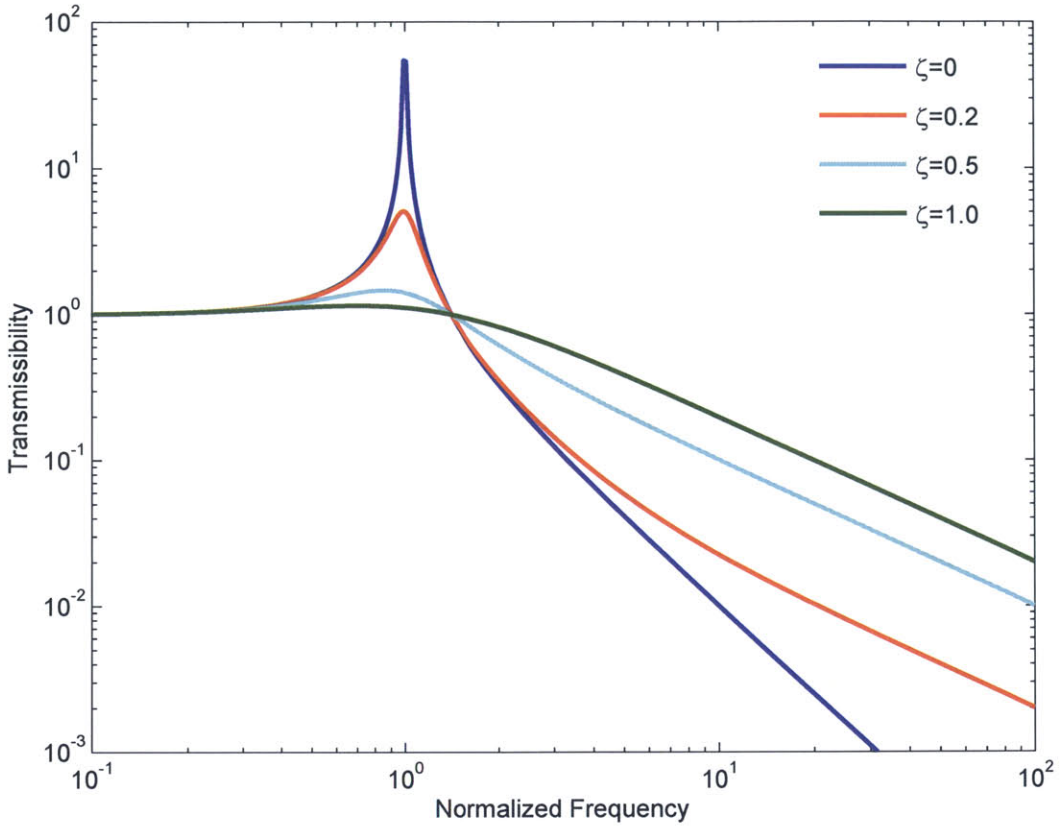

Figure 2-6: Examples of transmissibility with varying damping ratios.

The typical goal of an isolator design will be to reduce the system natural frequency far below the driving frequency so the transmissibility at the driving frequency is low. The system natural frequency is manipulated by mounting the system on rubber mounts of the proper stiffness.

Damping ratio plays an important role in isolator design in that high damping is desirable below a normalized frequency of 1.414 to control the resonant peak, while at frequencies higher than 1.414 the transmissibility is increased by high damping. For more information on damping and other issues in isolator design see the following references [17, 15, 19].

An issue that can arise in passive vibration isolation is internal rubber resonances or the wave effect [14]. The internal resonances are due to the inertia existing within

practical vibration isolators and degrades the expected isolator performance. This issue becomes more relevant as the rubber isolator dimensions decrease or frequencies of operation increase.

2.3.5 Automobiles

Chrysler carried out work on rubber mounts for suspending the automobile engine as early as 1929 [17]. The concept for suspending the engine on rubber mounts became known as the floating power principle and made its debut in the 1931 Plymouth PA [2]. The smoothness provided by the floating power principle became a trademark of the Plymouth and other automobile makers paid royalties to use the concept in their own vehicles.

The primary elements for employing the floating power principle are rubber mounts. Rubber is used almost exclusively for these mounts as it supports static and low-frequency loads while suppressing vibration and shock transmission. The static and low-frequency loadings are a result of the engine weight, longitudinal/lateral vehicle accelerations, engine acceleration reaction moments, and thermal expansions. Higher frequency loads that should be attenuated across the mount are combustion vibration/shock, and reciprocal/rotary unbalance vibration caused by inherent engine imbalance.

Advances in automotive engine mounts have led to hydraulic engine mounts that utilize a rubber spring and restricted viscous fluid flow [45]. The hydraulic circuit in these engine mounts are tuned for a specific frequency and provide increased damping at the tuned frequency. The simplified explanation of the physics behind the hydraulic engine mount is that fluid exchange between two chambers absorbs energy at the tuned frequency. The channel is referred to as the inertial track and is the primary means for tuning the damping of the hydraulic engine mount to a desired frequency.

When compared to a conventional engine mount, a hydraulic engine mounts can provide a lower spring rate for improved isolation at lower frequencies while providing much higher damping for adequate control of resonances. The advantage of increased damping only near near the resonant frequency is evident after the discussion of

damping in passive vibration isolation above.

2.4 Summary

The field of precision positioning devices were surveyed to give the reader a sense of the metrics used to rate device performance and to the common principles often encountered in this field. The prior art actuator configurations most relevant to the actuator designed in this thesis was presented to introduce the class of actuator that is ideal for high force, short stroke applications.

Applications of rubber in several diverse fields were presented to showcase the usefulness of employing rubber as a guidance system. Several design tips can also be extracted from this review such as the idea of the center of pressure, stress or fatigue in the rigid supports, the effect internal rubber resonances can have on system performance, and the role of damping in these systems.

Chapter 3

Rubber Bearings

This chapter develops the issues which are fundamental to the development of the nanopositioner rubber bearing system. One method for finding the static stiffness of rubber bearings is developed in detail to provide insight into some the common assumptions and ideas necessary for designing rubber bearings for static loads. Equations for determining the stiffness of square rubber pads on rigid supports in all six DOF are provided, as well as the axial compression of rectangular annuli and solid rubber rollers. Dynamic models for rubber bearings are reviewed and the minimum useful model for analyzing the nanopositioner configuration is established.

3.1 Infinite Strip Approximation and Circular Pads

Consider a rectangular block of incompressible ($\nu \approx 0.5$) rubber that is considered infinite in length, with width b, bonded to rigid supports, and under uniaxial compression as shown in Figure 3-1(a). Any vertical strain will result in bulging in the horizontal direction as the material is incompressible and the strain in the length direction into the page is zero. The thin strip approximation is applicable to cases where the length is at least three times greater than the width and the compressional strains are less than 10% [33, 32]. The stiffness analysis begins by considering homogeneous compression where the rubber in contact with the rigid supports is allowed to slide laterally. The force per unit length required to maintain this homogeneous

deformation is given by Equation 3.1, where E_o is Young's modulus of the rubber and δ is the vertical deflection [17].

$$F_1 = \frac{4}{3}\frac{E_o b \delta}{t} \tag{3.1}$$

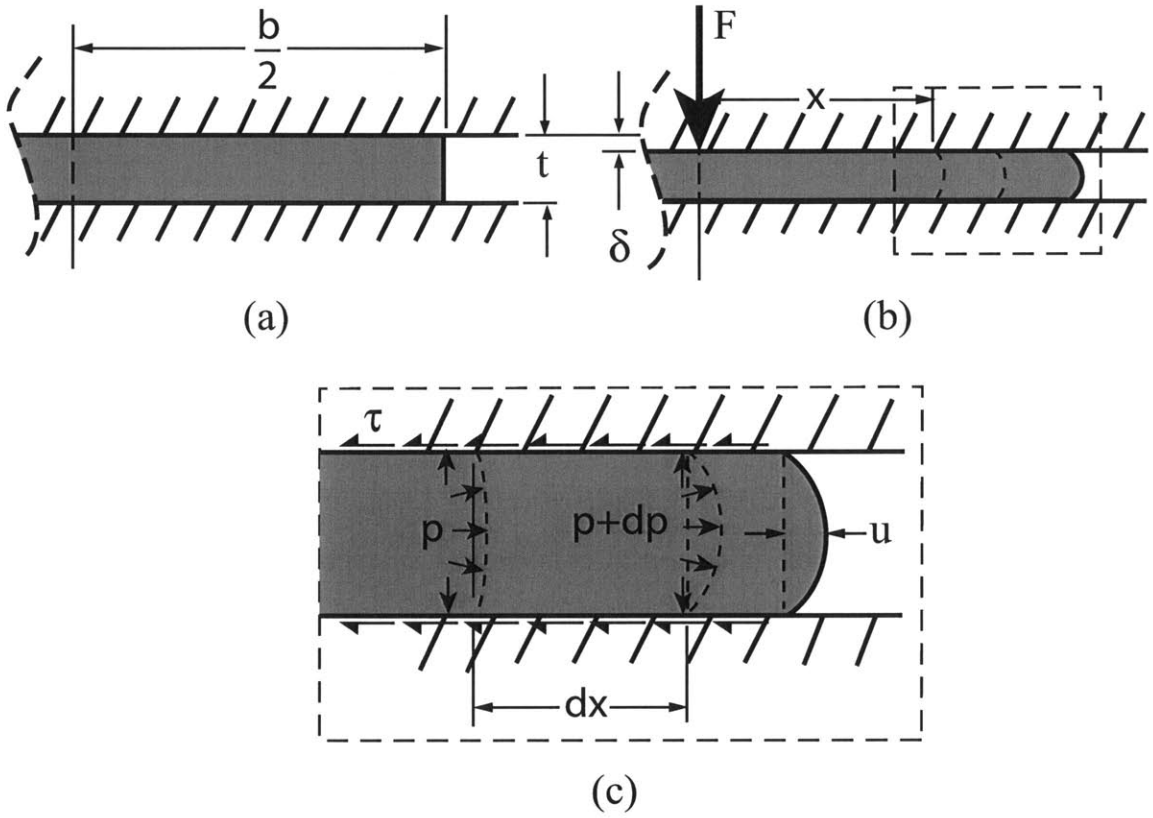

Figure 3-1: Infinitely long rubber strip of width b. (a) Undeformed state with plane of symmetry at $b/2$. (b) Strip that has deflected by δ due to the loading F. (c) A magnified view of the loaded strip showing the difference in internal pressure between two planes located at a distance dx apart. Figure adapted from Lindley [33]

Now consider the case where the rubber is bonded at the solid interfaces. The bonded joint of the rubber/support contact results in a shear stress τ along the interface with the support as shown in Figure 3-1(c). The addition of the shear stress to the homogeneous compression results in an additional force per unit depth, F_2, that is required to maintain the deflection, δ. This additional force can be found with

the assumptions that horizontal planes remain plane and the vertical sections assume the parabolic form shown in Figure 3-1(b-c).

The maximum horizontal displacement of the parabolic section, u, is found using the equivalence of volumes from the undeformed state to the final deformed state as the total rubber volume will not change. Said in a different way, the volume of the rubber displaced by the deflection, δ, will be identical to the volume of the parabolic bulging at the at the free surface.

The deflected rubber pad volume per unit depth is $x\,(t-\delta)$ plus the volume per unit depth in the bulge, where x is the distance from the central vertical plane of the rubber pad, t is the undeformed pad thickness, and δ is the vertical deflection of the pad. The first-order approximation for the volume of rubber per unit depth in the bulge is $2ut/3$, where u is the peak horizontal displacement of the bulge and is shown in Figure 3-1(c). Equivalence of volumes in the undeformed and deformed states leads to Equation 3.2 that is solved for the maximum horizontal displacement as shown in Equation 3.3.

$$xt = x\,(t-\delta) + \frac{2ut}{3} \tag{3.2}$$

$$u = \frac{3}{2}\frac{x\delta}{t} \tag{3.3}$$

An analogy of the bulging rubber with fluid being expelled from between parallel plates allows the pressure profile across the interface of the rubber and support to be determined using fluid mechanics. The fluid expulsion analogy gives us the hydrostatic pressure as a function of position required to maintain the parabolic bulge profile. This incremental pressure is a well known solution often utilized in the theory of elasticity and is given in Equation 3.4 in the theory of elasticity form and also with u of Equation 3.3 substituted for the maximum horizontal displacement [17].

$$dp = -\frac{8E_o u}{3t^2}dx = -\frac{4E_o \delta x}{t^3}dx \tag{3.4}$$

The total pressure as a function of position is determined by integrating the in-

cremental pressure between the position x and the force free surface at $x = b/2$. The force free surface at $x = b/2$ gives the zero pressure boundary condition that allows the hydrostatic pressure at all positions x to be determined by integrating the incremental pressure from the zero pressure point to the location x. The resulting hydrostatic pressure profile is given in Equation 3.5 as a function of position within the rubber pad.

$$p = \int_{x=b/2}^{x=x} -\frac{4E_o\delta x}{t^3}dx = \frac{2E_o\delta}{t^3}\left(\frac{b^2}{4} - x^2\right) \tag{3.5}$$

The hydrostatic pressure, p, acts equally in all directions and the force per unit depth due to the bulging is found by integrating the hydrostatic pressure along the interface of the bearing and the rigid support, as shown in Equation 3.6.

$$F_2 = \int_{-b/2}^{b/2} \frac{2E_o\delta}{t^3}\left(\frac{b^2}{4} - x^2\right) = \frac{E_o\delta b^3}{3t^3} \tag{3.6}$$

The result of this hydrostatic pressure is only the bulging of the rubber at the free surface and does not take into the homogeneous compression of the rubber pad. The total force per unit depth needed to displace the top support by δ relative to the bottom support is the homogeneous compression force (Equation 3.1) plus the force resulting from the hydrostatic pressure (Equation 3.6). The total force per unit depth is given in Equation 3.7 in a simplified form.

$$F_{total} = \frac{4}{3}\frac{E_o b\delta}{t} + \frac{E_o\delta b^3}{3t^3} = \frac{4}{3}\frac{E_o\delta b}{t}\left(1 + \frac{b^2}{4t^2}\right) \tag{3.7}$$

The calculation of total force per unit depth shown in Equation 3.7 is applicable in cases where the depth of the bearing, d, is greater than three times the width, b, and compressional strains are less than 10%. The theory for analyzing rubber pads that do not have a depth to width ratio greater than three is covered in Section 3.2.

A useful quantity to now define is the compressive modulus, E_c. The compressive modulus is the effective modulus of the rubber pad when viewed from the conventional linear stiffness, Hooke's Law, view of compression shown in Equation 3.8 where E is Young's modulus, A is the area of the material, and t is the thickness.

$$k = \frac{F}{\delta} = \frac{EA}{t} \tag{3.8}$$

This conventional form for compression stiffness also becomes accurate for rubber when Young's modulus is replaced by the compression modulus that will now be derived from Equation 3.7 by solving for $F_{total}d/\delta$ and comparing to Equation 3.8. Note that multiplying by d eliminates the per unit depth of the calculation allowing direct comparison of $F_{total}d/\delta$ with Equation 3.8 and the area of the bearing is bd.

$$k = \frac{F_{total}d}{\delta} = \frac{4}{3}E_o\left(1 + \frac{b^2}{4t^2}\right)\frac{A}{t} \tag{3.9}$$

The compression modulus for an infinite strip is then:

$$E_c = \frac{4}{3}E_o\left(1 + \frac{b^2}{4t^2}\right) \tag{3.10}$$

An analysis of a circular disk of rubber with thickness, t, and radius, a, using the same approach as that for the infinite strip leads to the following (see [33] pages 45-46 for details):

$$p = \frac{E_o\delta\left(a^2 - r^2\right)}{t^3} \tag{3.11}$$

$$F_1 = E_o\pi a^2\delta/t \tag{3.12}$$

$$F_2 = \frac{\pi E_o\delta a^4}{t^3} \tag{3.13}$$

$$E_c = E_o\left(1 + a^2/2t^2\right) \tag{3.14}$$

The theoretical compression stiffnesses for the infinite strip and circular rubber pads provided the footing for the development of the shape factor approach to designing practical rubber bearings in the following section.

3.2 Shape Factor

A particularly useful quantity to now define is the shape factor, S. The shape factor is taken as the ratio of the area of one loaded surface to the total force-free area on the periphery of the pad. Substitution of the shape factor into the compression modulus equations for both the infinite strip and circular disk results in a very useful form. The shape factor for the infinite strip is $b/2t$, while the shape factor for the circular disk is $a/2t$. Substitution of each shape factor into its respective compression modulus, Equations 3.9 and 3.14, results in the following:

$$(E_c)_{strip} = \frac{4}{3} E_o \left(1 + S^2\right) \tag{3.15}$$

$$(E_c)_{disk} = E_o \left(1 + 2S^2\right) \tag{3.16}$$

The form of the compression modulus for circular disks also turns out to have greater utility, as the compression modulus for rectangular pads of length d and width w is obtained by substituting the shape factor for the rectangular pad into Equation 3.16 [33]. The shape factor for the rectangular pad is given as the following with the loading condition shown in Figure 3-2:

$$S = \frac{dw}{2t\,(d + w)} \tag{3.17}$$

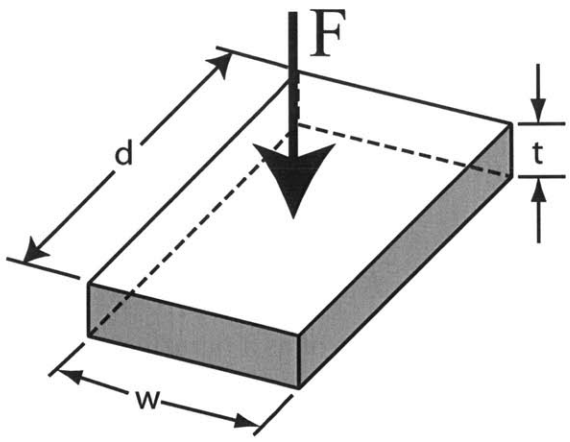

Figure 3-2: Rectangular pad showing the compressional loading direction [33]

Two important modification parameters are needed before Equations 3.15-3.16 can be applied due to the rubber having a finite bulk modulus, referred to as K. One parameter required to keep the compression modulus equations accurate over a broad range of bulk moduli and Young's moduli is a modification factor k. The second term of the compressional moduli have been found to be smaller than the theory predicts due to the actual Poisson's ratio being less than the idealized 0.5 and the shear stiffness of the rubber/support interface being finite.

The modification factor is a function of rubber hardness and is tabulated in Table 3.1, along with other general material properties. The properties of Table 3.1 were originally tabulated by Lindley for used in designing natural rubber bearings with carbon black used as a reinforcing agent, but have been used throughout this work and by Barton with good results in cases where more accurate values for other rubbers were unavailable [37]. The modified compressional modulus equations are shown here:

$$(E_c)_{strip} = \frac{4}{3} E_o \left(1 + kS^2\right) \tag{3.18}$$

$$(E_c)_{disk} = E_o \left(1 + 2kS^2\right) \tag{3.19}$$

The second modification parameter needed to keep the compressional moduli accurate for a range of shape factors is E_∞, which is identically the bulk modulus for Poisson's ratio equal to 0.5. Lindley [17] defines the ratio of E_∞ to bulk modulus as a function of Poisson's ratio as given here:

$$\frac{E_\infty}{K} = \frac{3(1-\nu)}{1+\nu} \tag{3.20}$$

This new term, E_∞, can be thought of as a derating of the compressional modulus due to the rubber having finite bulk modulus. It is effectively a second spring in series with the spring described by the compressional modulus. The effect of the derating is shown mathematically in Equation 3.21 and graphically in Figure 3-3 where the final form of the compressional modulus is plotted versus shape factor.

$$E_c = \left[\frac{1}{E_o(1+2kS^2)} + \frac{1}{E_\infty}\right]^{-1} \tag{3.21}$$

The effect of the bulk modulus is the plateau in compressional modulus as the shape factor approaches 50. The code for generating Figure 3-3 is found in Appendix A. It should be noted that the compressional stiffness defined here also applies in tension, although tensile loadings dramatically increase the importance of proper bonding between the rubber and the supports. All bearing in this work are under a compressive preload as adhesion of the bearing to the support was not investigated.

Table 3.1: Approximate material properties for rubbers of known Shore A hardness (adapted from [33] using chart from [25])

Shore A	**Hardness IRHD**	**Young's Modulus** E_o[MPa]	**Shear Modulus** G[MPa]	**k**	E_∞ [MPa]
30	30	0.92	0.30	0.93	1000
36	35	1.18	0.37	0.89	1000
40	40	1.50	0.45	0.85	1000
45	45	1.80	0.54	0.80	1000
50	50	2.20	0.64	0.73	1030
55	55	3.25	0.81	0.64	1090
61	60	4.45	1.06	0.57	1150
66	65	5.85	1.37	0.54	1210
69	70	7.35	1.73	0.53	1270
76	75	9.40	2.22	0.52	1330

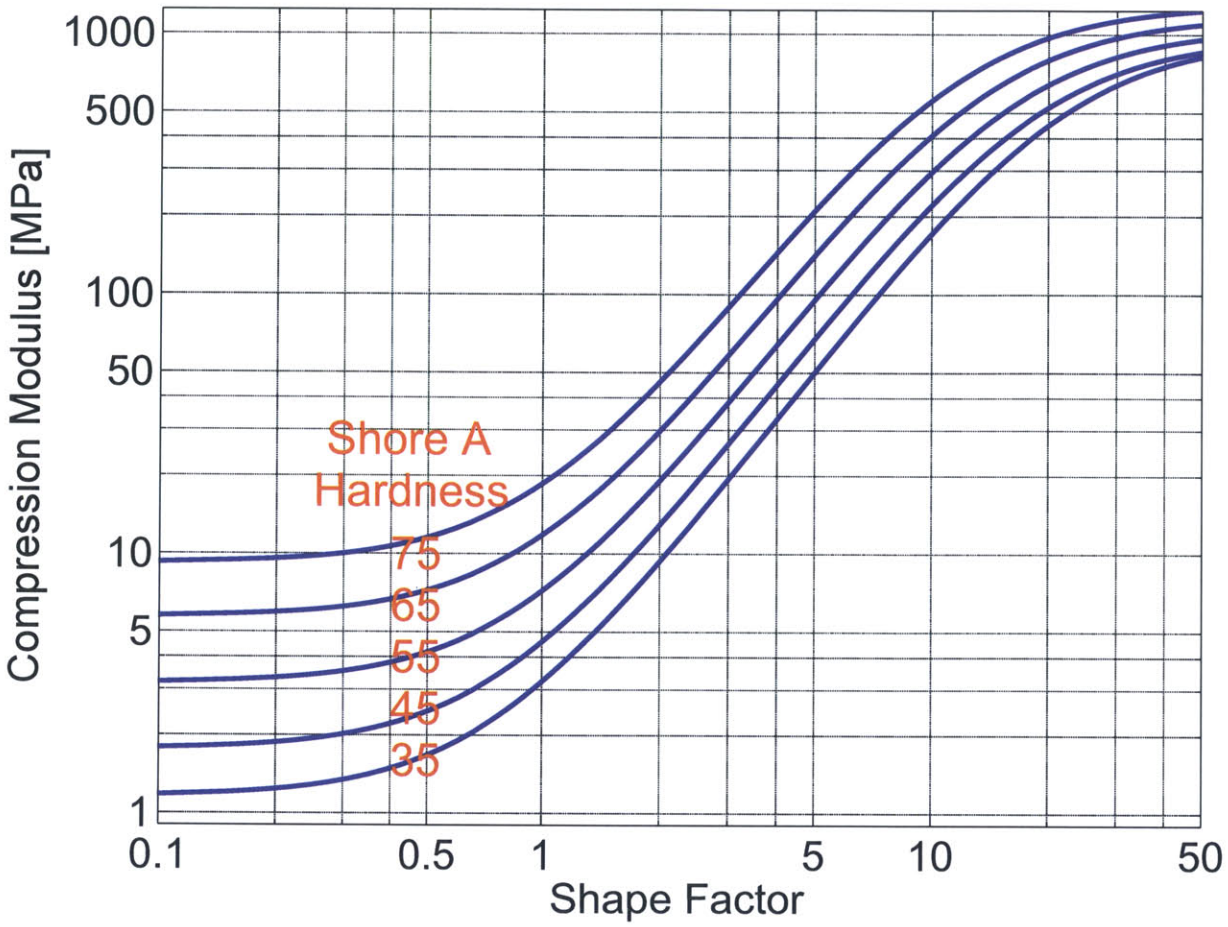

Figure 3-3: Variation of compression modulus with shape factors parametric on rubber hardness.

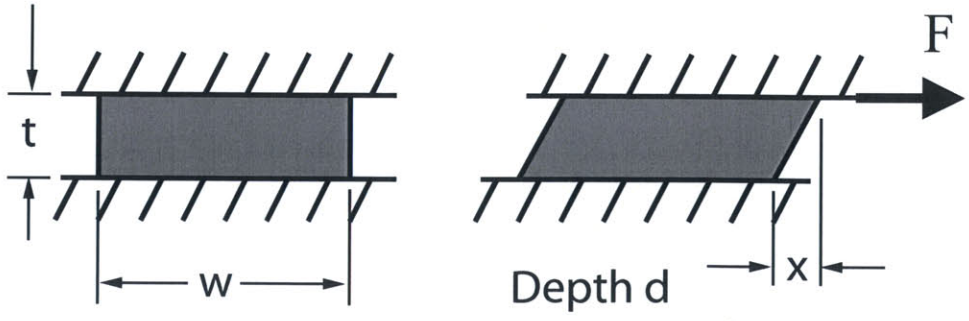

Figure 3-4: Rectangular rubber pad under shear.

3.3 Shear Loading

Shear loading is the second most important loading for rubber bearings, with compressional loading being the first, as shear loading of the bearing is the compliant loading direction that is the servo direction in a positioning device. The stiffness of rubber pads under compression has been shown to be a strong function of geometry and departs from classical linear elasticity that applies so well to most other materials. Fortunately determination of the shear stiffness does not require a special analysis and exactly mirrors linear elasticity for shear strains less than 50%, although shear mountings have been shown to survive shear strains greater than 300% [33]. Equation 3.22 is used to determine the shear stiffness of a rectangular rubber pad with the variable definitions of Figure 3-4 and G is the material shear modulus.

$$k_{shear} = \frac{F}{x} = \frac{Gwd}{t} \tag{3.22}$$

An approximate value for the rubber shear modulus required in Equation 3.22 can be found by referring to Table 3.1 in cases where the Shore A hardness is known. These values were shown to be reasonably accurate for several commercially available rubbers [37], although high accuracy values can be obtained through testing the materials with the appropriate equipment. Testing is recommended for nonconventional formulations, cast bearings, and cases where precise control of shear stiffness is desired (i.e. matching magnetic stiffness to spring stiffness).

One of the promising aspects of employing rubber bearings in precision machines is shown in Figure 3-5 where the ratio of compression to shear moduli are plotted versus rubber thickness for a 25mm by 25mm cross-section of 50 Shore A hardness. The ratio E/G approaches 1000 as the rubber thickness decreases. This translates into lower bearing shear stiffness while maintaining high compression stiffness when implemented as a laminated rubber bearing.

Rivin had published a figure similar to that of Figure 3-5 that clearly demonstrated the promise of rubber bearings although the limits of the relationship were not specified [41]. The lower limit for E_c/G comes from the relation shown in Equa-

tion 3.23 and the fact that at very low shape factors the compressional modulus approaches Young's modulus ($E_c \rightarrow E$). The upper limit is E_∞/G due to the compressional modulus approaching the bulk modulus for high shape factors. Note that the upper limit is only representative of a few rubber compounds and can be pushed higher using other compounds, composite structures, or custom formulations. The tire industry uses a combination of these methods in different sections of tires in trying to decouple some performance parameters such as lateral acceleration from road vibration transmission [34].

$$E = 2\,(1+\nu)\,G \tag{3.23}$$

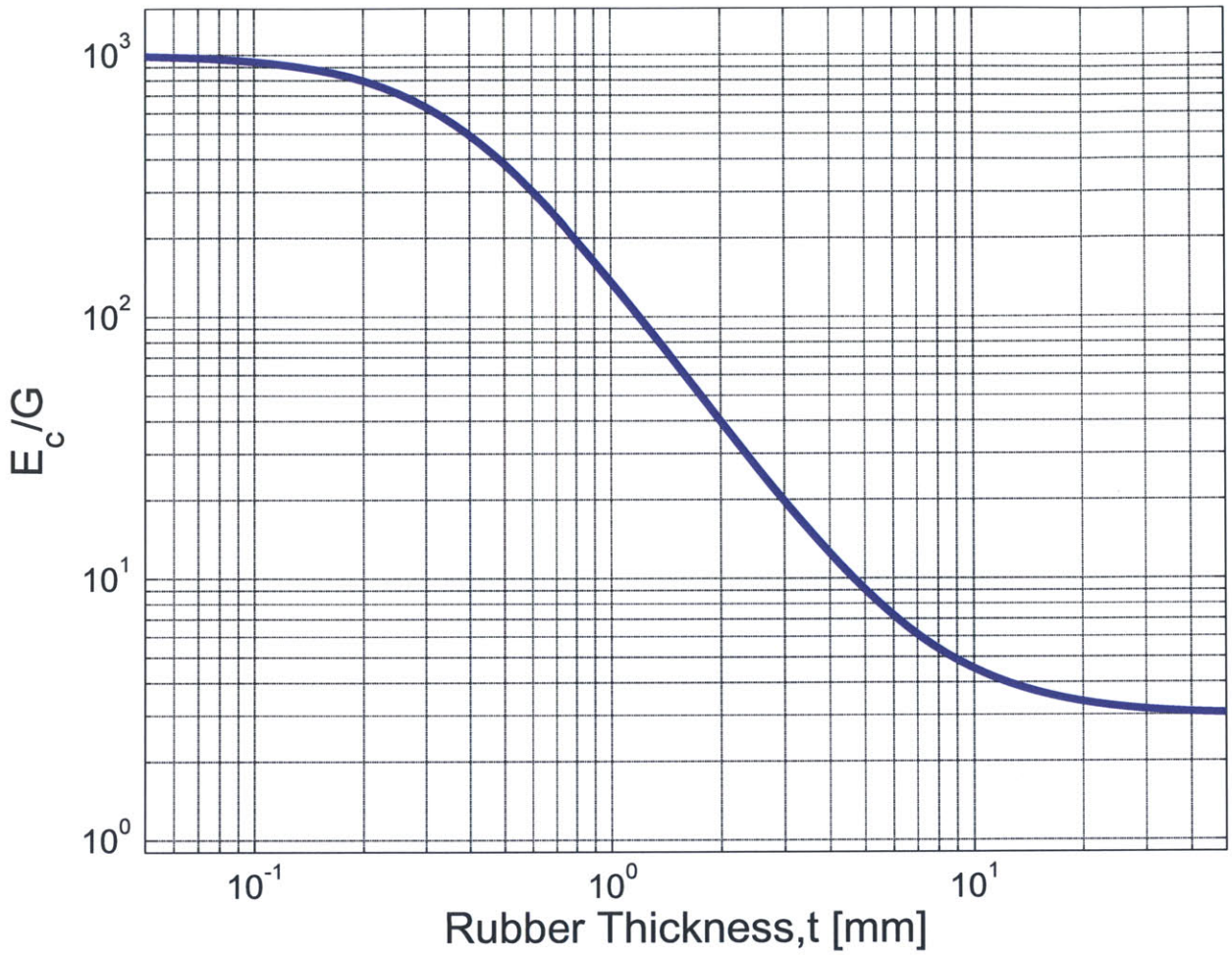

Figure 3-5: Plot of compressional modulus to shear modulus ratio for varying rubber thicknesses and rubber hardness of 50 Shore A (modified form of figure found in Rivin [41])

3.4 Rectangular Pads Under Other Loadings

Compression and shear loadings only account for the three translational DOF of the rubber pad shown in Figure 3-6. The remaining three DOF are θ_x, θ_y, and θ_z that correspond to bending, bending, and torsion loadings of the rubber pad, respectively.

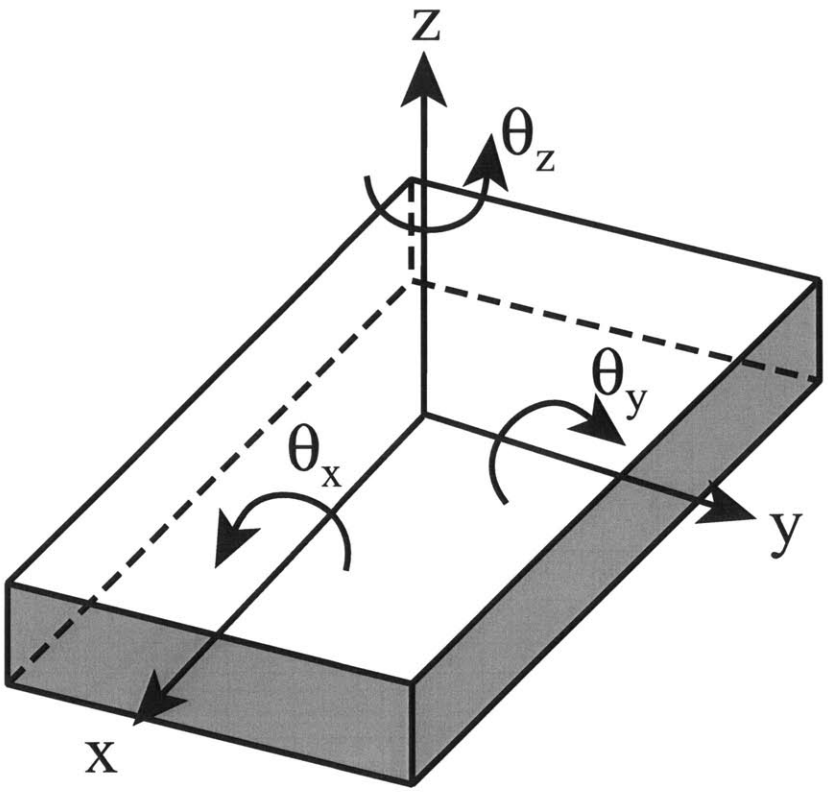

Figure 3-6: Displays the 6 degrees of freedom of a rubber sheet.

Bending of the rubber pad will result from a moment M being applied to one of the rigid supports and causing a misalignment of ϕ as shown in Figure 3-7. Rotations about the x- and y-axes of Figure 3-6 will result in such a configuration and one can expect a shape factor analysis to be required as this bending is effectively a distributed compression and tension. The approach often taken for determining bending stiffness is to come up with an effective bending stiffness, $(EI)_{eff}$, that can be directly substituted into the linear elasticity equation for bending in place of EI, as shown in Equation 3.24. Many different closed-form solutions have been proposed for the effective bending stiffness and the one used in the design of the nanopositioner was proposed by Gent and Meinecke for square rubber layers of side length w in Equation 3.25 [18, 53]. Bending is considered one of the constrained loadings of the rubber bearings.

$$k_{bending} = \frac{M}{\phi} = \frac{EI}{t} = \frac{(EI)_{eff}}{t} \tag{3.24}$$

$$(EI)_{eff} = 3G\left(\frac{w^4}{12}\right)\left(1 + 0.7424\left(\frac{w}{4t}\right)^2\right) \tag{3.25}$$

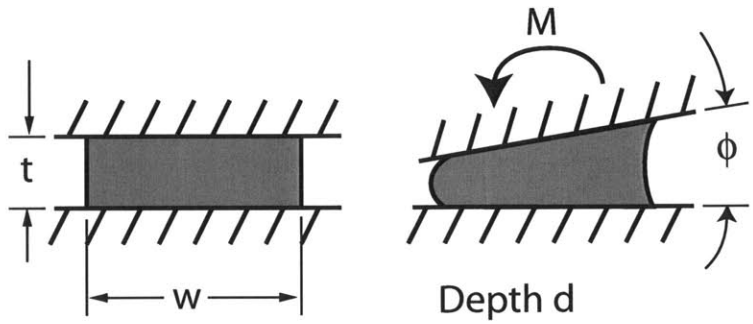

Figure 3-7: Rectangular pad showing the bending moment and the resulting deformation.

A visualization of the bending deflection was created through an FEA analysis with the resulting deformation shown in Figure 3-8. An FEA model of the 25 mm square by 0.8 mm thick rubber bearings was set-up in ADINA to provide the visualization of the deflection lines when a bending moment is applied[1]. The shear modulus and Poisson's ratio were set to 0.64 MPa and 0.49, respectively, for the analysis. Before the load was applied all lines were vertical or horizontal. The loading has now caused bulging of the previously vertical lines except for the two vertical planes at the locations specified by the arrows. The plane on the left is located at the center of compressional pressure and the plane on the right is at the center of tensile pressure. The FEA analysis also found the stiffness of the rubber bearing to be within 10% of the value found using the analytical equations of Gent and Meinecke.

[1]Dan Kluk provided a great deal of assistance with defining and solving the model in ADINA

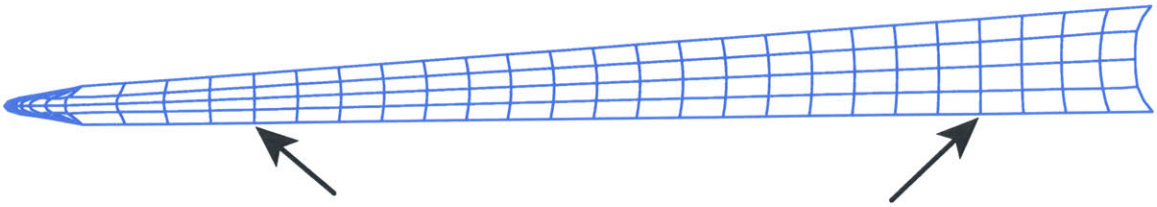

Figure 3-8: Side view of rubber bearing under a bending load.

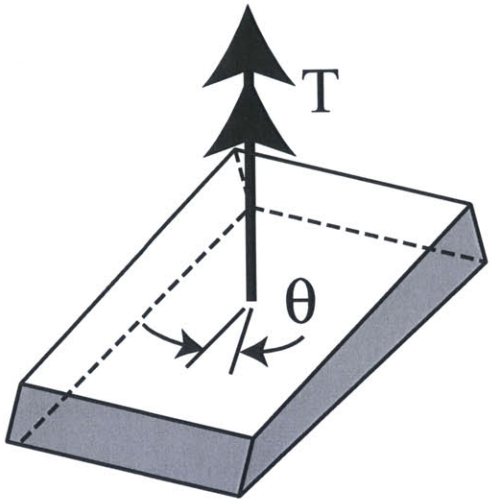

Figure 3-9: Rectangular pad showing the torsional loading direction.

The final loading of interest for the design of the nanopositioner is the θ_z rotation, shown in Figure 3-6. This loading is referred to as the torsional loading loading of the bearing through the rest of this work. This torsional loading is placing the rubber in axisymmetric shear about the z-axis and can be analyzed using linear elasticity. The torsional stiffness of the bearing is determined by employing Equation 3.26 where I_p is the polar moment of inertia and the resulting deformed configuration is shown in Figure 3-9. The angular misalignment of the upper and lower supports is specified as θ in the figure.

$$k_{tor} = \frac{GI_p}{t} \tag{3.26}$$

In summary, a rubber pad bonded between two rigid supports will constrain three DOF and leave three DOF compliant. The constrained DOF with respect to Figure 3-6 will be z-translation, θ_x and θ_y rotations while the less-constrained motions are θ_z rotation, x-translation and y-translation. All six DOF of a rubber bearing support system may now be determined using the stiffness results defined above.

3.5 Rectangular Annuli and Rubber Rollers

Two additional rubber pad configurations that are of engineering importance are the rectangular annulus and solid rubber roller. The rectangular annulus configuration is the shape of the rubber specimen that was cast and tested in the compression fixture in this work. More on the cast bearing can be found in Chapter 5. The stiffness of the cast bearing was accurately predicted using Equation 3.27 with the definitions of Figure 3-10 and D_m equal to the average diameter and b is the radial width of the section found as $(D+d)/2$ and $(D-d)/2$, respectively.

$$k_{annulus} = \frac{F}{x} = \frac{4}{3} E_o \pi D_m \frac{b}{t} \left[1 + \frac{kb^2}{4t^2} \right] \tag{3.27}$$

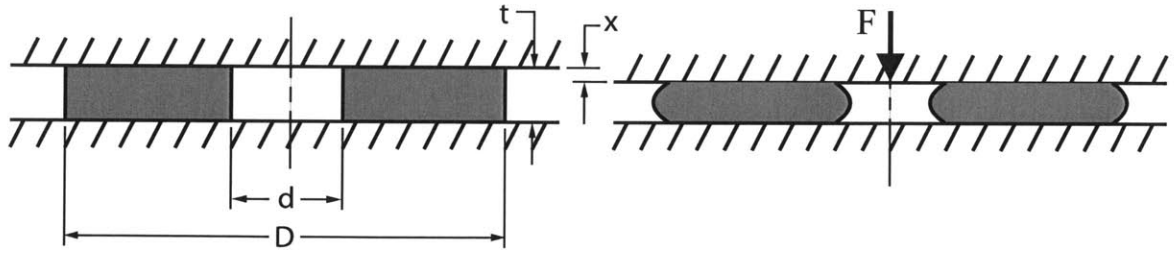

Figure 3-10: Cross-sectional view of an uncompressed and compressed rectangular annulus of rubber.

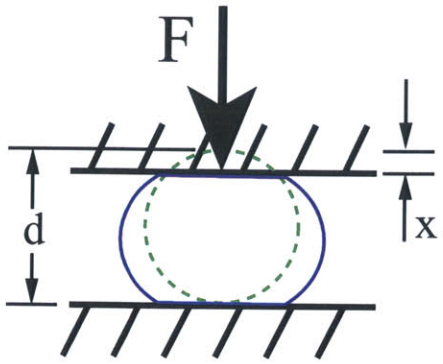

Figure 3-11: Rubber roller in a deformed configuration.

The solid rubber roller load-deformation relationship is very nonlinear due to the contact area increasing as the deflection increases. Figure 3-11 shows a deformed configuration of a solid rubber roller and Equation 3.28 describes the force-compression relationship where F_L is the force per unit length [33]. Equation 3.28 was developed using the plain strain condition which makes the relationship below useful for analyzing a positioner bearing configuration that utilizes stacked o-rings (see Section 6.1) [33]. Solid rubber rollers are most commonly encountered as o-ring seals and Figure 3-12 shows the normalized compression force for an o-ring of major diameter, D, versus squeeze ratio for axial compression. The dotted line in Figure 3-12 is the first term of Equation 3.28 and is very accurate up to squeeze ratios of 20%, which happens to be the maximum squeeze recommended for most o-ring applications.

$$\frac{F_L}{dE_o} = 1.25\left(\frac{x}{d}\right)^{3/2} + 50\left(\frac{x}{d}\right)^{6} \tag{3.28}$$

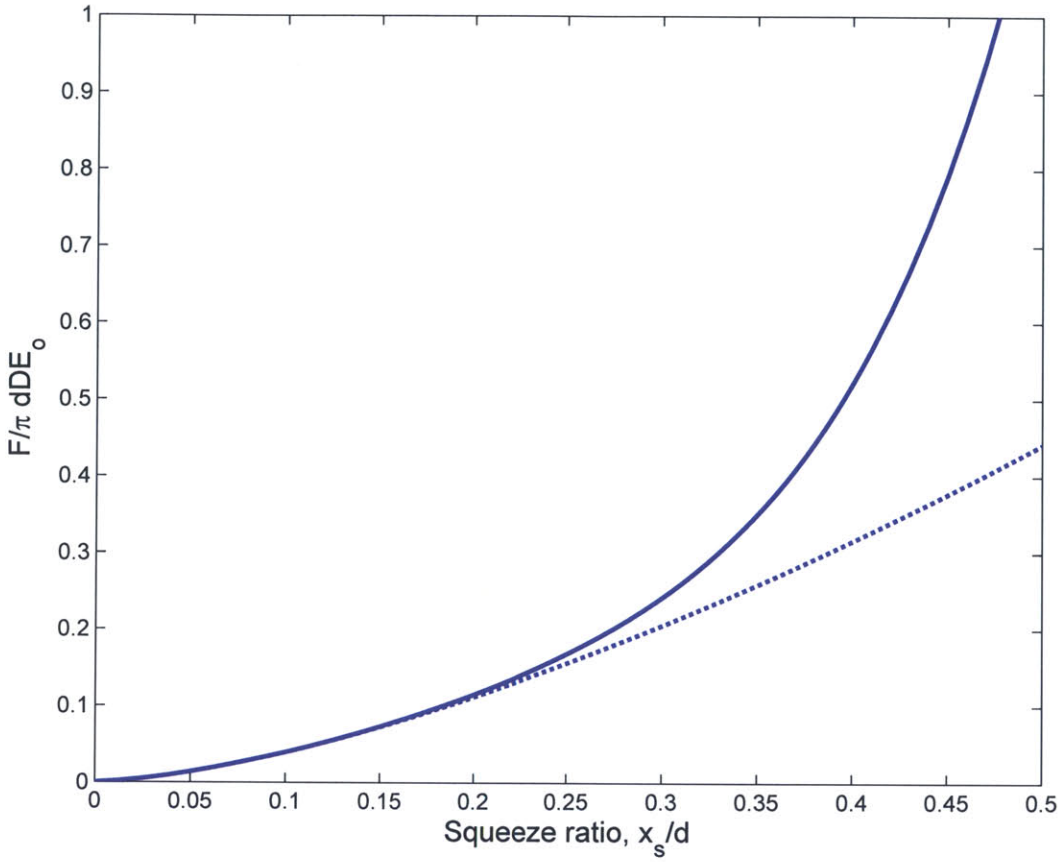

Figure 3-12: Normalized compression force for a given squeeze ratio.

3.6 Dynamic Rubber Models

Many simple models have been proposed to model the viscoelastic nature of rubber springs. The most straightforward models consist of different configurations of springs and dampers as shown in Figure 3-13. The simplest model of viscoelastic behavior are the Maxwell and Voigt models. These two models give some insight into the step response behavior of rubber pads, but are too simplistic to be useful as a design tool in the frequency domain. The Maxwell model is a useful tool for internalizing the rubber relaxation over long periods of time, while the Voight model can be used to represent the finite response time of the rubber near the step. The dynamic stiffness of each model is shown in Table 3.2 and note the dynamic stiffness for the multiple

standard elements model is in a different, but equivalent, form to that found in the literature [28, 1, 37]. The negative terms of the form in the table can effectively be viewed as derating factors for each spring that is in series with a damper.

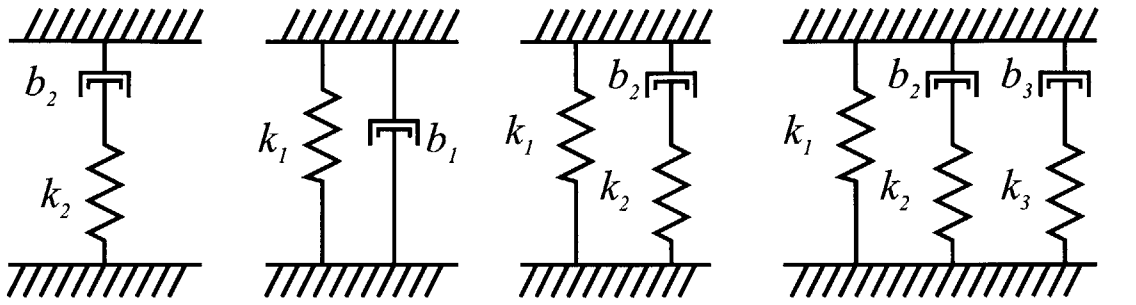

(a) Maxwell model (b) Voigt model (c) Standard model (d) Multiple standard element model

Figure 3-13: Classic models for viscoelastic behavior of rubber.

Table 3.2: Dynamic stiffness for classical viscoelastic models.

Model	**Dynamic Stiffness**
Maxwell	$\frac{sK_2B_2}{K_2+sB_2}$
Voight	K_1+sB_1
Standard	$K_1+\frac{sK_2B_2}{K_2+sB_2}$
Multiple standard element	$K_1+K_2+K_3\ldots-\frac{K_2^2}{B_2s+K_2}-\frac{K_3^2}{B_3s+K_3}-\ldots$

An important parameter that these classic models do not explicitly show that is absolutely critical in designing a positioning system is the mass suspended on the spring/damper arrangements. A more accurate view of these models for the nanopositioner application is shown in Figure 3-14. The stiffness transfer function for this complete model is shown in Equation 3.30 and Figure 3-15 shows the agreement

of the model with experimental data for a cast silicone rubber pad in compression. The transfer function overlayed the data is given in Equation 3.29.

$$K = \frac{239.7s^3 + 4.315e005s^2 + 7.343e010s + 3.69e012}{s + 30000} \tag{3.29}$$

While the agreement of the model with the experimental data is not sufficient for control design, it is the simplest model that gives useful qualitative frequency response information. More accurate frequency domain models can be developed by fitting a transfer function to experimental data. The transfer function forms can be found using multiple standard element configurations with progressively more elements or through an ad hoc method of adding poles and zeros.

$$K = ms^2 + (k_1 + k_2) - \frac{k_2^2}{b_2 s + k_2} = \frac{mb_2 s^3 + mk_2 s^2 + (k_1 + k_2)\, b_2 s + k_1 k_2}{b_2 s + k_2} \tag{3.30}$$

The notch in Figure 3-15 is a result of the mass resonating on the rubber spring. Even though the rubber has a complex stiffness, the resonance still exists at the particular frequency where the transfer of the spring potential energy to kinetic energy of the mass and back to the spring occurs with very little loss. Note that this resonance of the mass on the spring results in zeros of the stiffness transfer function whereas it appears as poles in the more conventional controls view with the displacement transfer function.

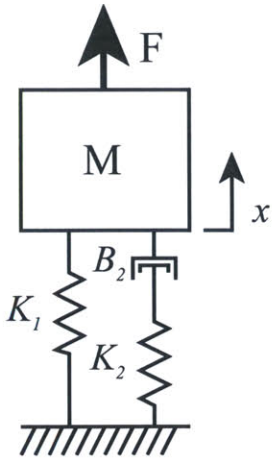

Figure 3-14: Proper standard model view of rubber stiffness for bearing applications.

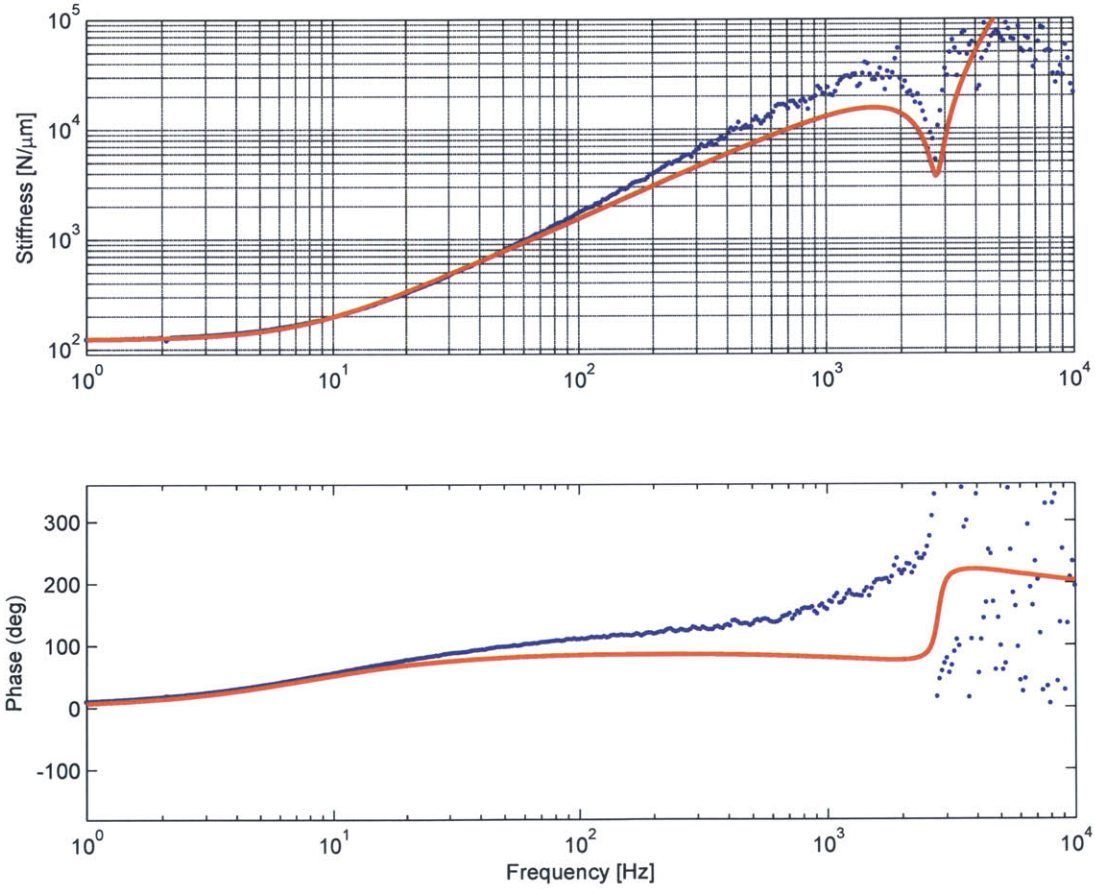

Figure 3-15: Experimental data (blue) with a model derived from Figure 3-14 overlayed (red).

3.7 Summary

Methods for determining the static stiffness of important rubber geometries that will be encountered later in this work have been reviewed. The theory behind these methods was developed for the infinite strip approximation to reveal the basic assumptions and limitation of these static rubber pad analyzes. Dynamic rubber stiffness models were presented and extended to forms useful for positioning applications.

THIS PAGE INTENTIONALLY LEFT BLANK

Chapter 4

Electromagnetics Review

The chapter provides a review of Maxwell's equations and the reluctance method in the context of analyzing magnetic circuits with permanent magnets and coils. The goal of this chapter is present the methods used in analyzing magnetic circuits with coil currents and permanent magnets as magnetic field sources. Magnetic forces at pole faces can be determined once the magnetic field intensity and magnetic flux density have been determined.

Several different methods for analysis are available for quasi-static magnetic systems. Each method has advantages and a combination of the two methods presented here were utilized in the development of the nanopositioner. The ultimate goal of each analysis is to determine the magnetic force versus current relationship for a given configuration. Useful by-products of this process include determination of the vector quantities magnetic flux density ($\underline{B}$) and magnetic field intensity ($\underline{H}$), as well as scalar quantities coil inductance (L) and speed voltage. Other quantities that are computed during the analyzes include current density ($\underline{J}$), magnetization density ($\underline{M}$), magnetic permeability (μ), and flux linkage (λ).

The magnetic circuits of Figures 4-1 and 4-2 will be analyzed using both of the analysis methods. Note the terms magnetic flux density and magnetic field intensity will be used interchangeably with B-field and H-field throughout this work.

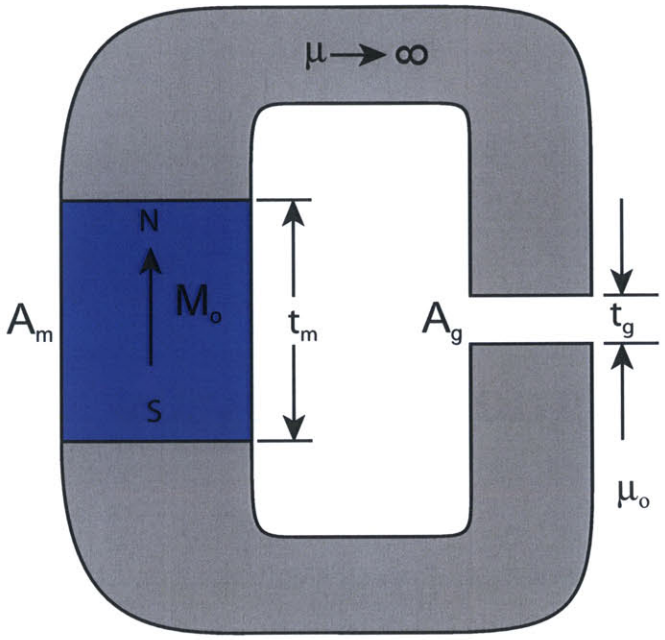

Figure 4-1: Permanent magnet in a magnetic circuit with an infinite permeability core and an air gap.

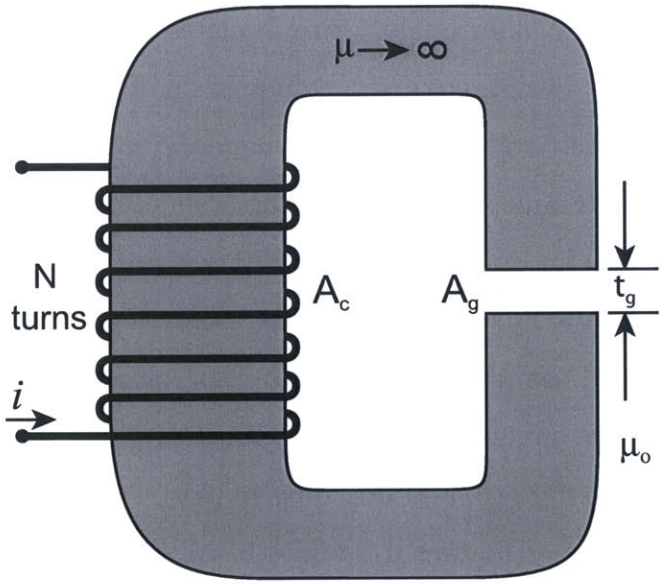

Figure 4-2: Coil driving flux through infinite permeability core with an air gap.

Figure 4-1 shows a permanent magnet in a magnetic circuit with an infinitely

permeable core that has an air gap of length t_g. The magnetic flux density in the magnet face is assumed uniform as $\underline{B}_m$ and is dependent upon the reverse magnetic field intensity, $\underline{H}_m$, as well as the permanent magnet material property magnetization density $\underline{M}_o$. A permanent magnet that is captured in a solid, infinitely permeable core would have no resistance to the magnetic potential provided by the magnet and the flux density in the magnet would be $\underline{B}_m = \mu_o \underline{M}_o$. Once an air gap is introduced to the core, as in Figure 4-1, a reverse magnetic field intensity $\underline{H}_m$ will oppose the permanent magnet flux and the magnetic flux through the core and air gap will be reduced from $\mu_o \underline{M}_o$. Figure 4-2 shows an infinitely permeable core with a drive coil of N turns and an air gap of length t_g. A current in the coil acts as a magnetic field intensity source and the magnetic flux density in the air gap can be determined. The magnetic force applied across the pole faces of each example can be calculated once the magnetic flux density has been determined.

4.1 Maxwell's Equations

Maxwell's equations are the primary tool for analyzing general electromagnetic systems. Several simplification to Maxwell's equations can be made when the system does not operate at high frequencies or on very short time scales. In the case of magnetic-field dominated systems, these simplifications stem from the assumption that the displacement current $\frac{\partial \epsilon E}{\partial t}$ is negligible where E is the electric field and ϵ is the electrical permittivity [22]. The quasistatic form of Ampere's and Gauss's Laws are summarized in Equations 4.1 and 4.2, respectively, with the constitutive relation for magnetic fields in media in Equation 4.3.

$$\oint_C \underline{H} \cdot \underline{dl} = \int_S \underline{J} \cdot \underline{n} \, da \tag{4.1}$$

$$\oint_S \underline{B} \cdot \underline{n} \, da = 0 \tag{4.2}$$

$$\underline{B}_m = \mu_o \left(\underline{H}_m + \underline{M}_o \right) \tag{4.3}$$

Application of Equation 4.1 around a contour allows one to find the H-field along the contour resulting from the current passing through the surface the contour bounds. The current is then a direct H-field source. The H-field delivered by a permanent magnet to a magnetic circuit is dependent upon the resistance the magnetic circuit has to flux. The resistance to magnetic flux of a circuit is reflected by the the magnet H-field, H_m. These two points are important and will be clear after working through the examples.

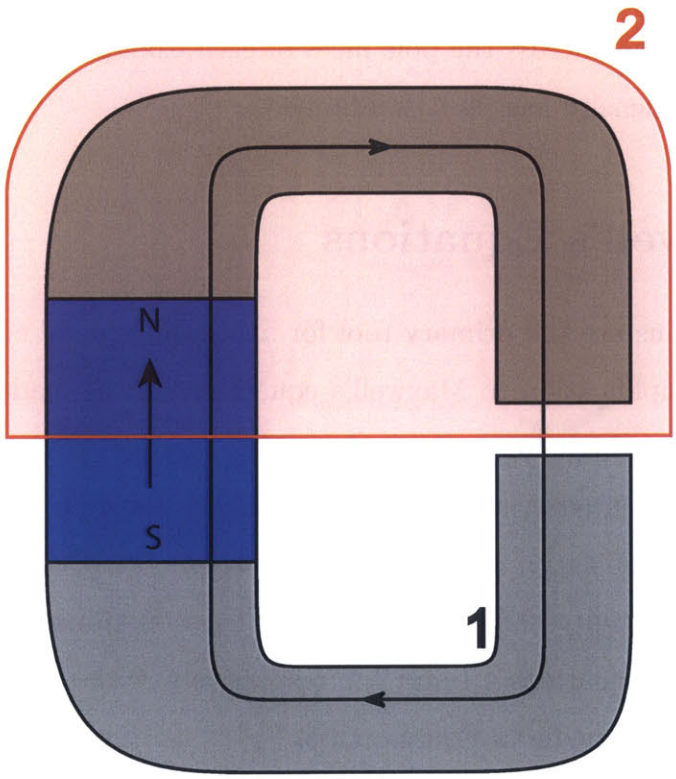

Figure 4-3: The contour 1 for applying Equation 4.1 and the closed surface 2 for applying Equation 4.2.

The first case to be analyzed is the permanent magnet in the magnetic circuit. Figure 4-3 shows Contour 1 and Surface 2, which Equations 4.1 and 4.2 are evaluated with respect to. Applying Ampere's Law around contour 1 and assuming the H-field

in both the magnet and the gap are defined with a positive sense relative to the arrowheads on the contour results in Equation 4.4 as the magnetic field intensity is zero in the infinitely permeable media. H_g is the magnetic field intensity in the air gap caused by the permanent magnet and H_m is the reverse magnetic field intensity inside the magnet due the increased magnetic reluctance caused by the air gap.

$$H_g t_g + H_m t_m = 0 \tag{4.4}$$

Application of Gauss's Law to Surface 2 of Figure 4-3 with the assumption the permanent magnet flux entering through the magnet area, A_m, is positive and the air gap flux leaving the surface through the pole face area, A_p, is negative results in Equation 4.5. Substitution of the constitutive law for magnetizable media (Equation 4.3) into Equation 4.5 is shown in Equation 4.6.

$$B_m A_m - B_g A_g = 0 \tag{4.5}$$

$$\mu_o \left(H_m + M_o\right) A_m - B_g A_g = 0 \tag{4.6}$$

The reverse H-field in the magnet, H_m, can then be solved for in terms of the pole face area, magnet area, H-field in the gap, and the magnetization density of the permanent magnet, as shown in Equation 4.7.

$$H_m = \frac{H_g A_g}{A_m} - M_o \tag{4.7}$$

Equations 4.4 and 4.7 form a system of two equations with unknowns H_m and H_g that can be solved as shown in Equation 4.8 and 4.9.

$$H_g = \frac{M_o t_m A_m}{A_m t_g + A_g t_m} \tag{4.8}$$

$$H_m = M_o \left(\frac{A_g t_m}{A_m t_g + A_g t_m} - 1 \right) \tag{4.9}$$

Note that for this system H_m is always negative relative to the assumed positive direction the same as M_o of Figure 4-1 and therefore reverse biases the magnet and reduces the flux provided to the circuit by the magnet.

The H-field in the air gap of the coil-driven core is simpler to determine. Application of Ampere's Law around a curve similar to Curve 1 of Figure 4-3 yields:

$$H_g = \frac{Ni}{t_g} \tag{4.10}$$

Once the H-field in an air gap is determined in both the permanent magnet and coil-driven configurations, the magnetic force on the pole face is determined using the normal component of the Maxwell stress tensor. For the normal-stress actuator geometries encountered throughout this work this gives:

$$F = \frac{B^2 A_p}{2\mu_o} \tag{4.11}$$

4.2 Reluctance Method

The complexity of applying Maxwell's equations to magnetic configurations quickly compounds as the number of flux paths increase, but luckily an alternative approach has been developed that is analogous to electrical circuit analysis and is referred to as the reluctance method. The term used to describe the motivating force for flux to move around a magnetic circuit is the magnetomotive force (MMF), and is analogous to the electromotive force of electrical circuits. Magnetic resistance is referred to as reluctance and is proportional to the mean flux path and inversely proportional to the cross sectional area of the flux path. There is also a scaling factor of $1/\mu$ that is analogous to the electrical conductivity. The definition of magnetic reluctance is given in Equation 4.12. A flux is due to some MMF, denoted $\mathcal{F}$, being supplied across a reluctance and the amount of flux is governed by Equation 4.13.

$$R = \frac{l}{\mu A} \tag{4.12}$$

$$\Phi = \frac{\mathcal{F}}{R} \tag{4.13}$$

The reluctance method allows the rules of circuit analysis to be used to simplify and solve reluctance models for flux through the magnetic circuit. The method also allows the reluctance of a non-infinitely permeable magnetic core to be easily taken into account as the core reluctance is easily folded in with the other terms as the reluctance term R_{core}. The core reluctance can be included in the Maxwell method, although the extra term requires more care than when using the reluctance method.

Analysis of the magnetic circuit of Figure 4-1 using the reluctance method, and not neglecting the core reluctance, results in one of the two magnetic circuits of Figure 4-4 where R_g is the air gap reluctance and R_m is the internal magnet reluctance. The internal magnet reluctance is found by evaluating Equation 4.12 with l_m the length of the magnet in the magnetization direction, μ as the permeability of free space μ_o and the magnet area A_m. The configuration of the internal magnetic reluctance with the source portion of the magnet is dependent on whether the magnet is viewed as a flux source or MMF source. Figure 4-4(a) results by modeling the permanent magnet as a flux source where the total flux, Φ_{pm}, is found by assuming $\underline{H}_m$ of Equation 4.3 is equal to zero.

$$\Phi_{pm} = B_m A_m = \mu_o M_o A_m \tag{4.14}$$

It is stated on Page 74 that the H-field in the magnet is a measure of the magnetic circuits resistance to flux, or reluctance. Setting the magnet H-field to zero eliminates the internal dependence of the magnet flux on the magnetic circuit reluctance, which is instead reflected by the reluctance elements that are external to the magnet. This is analogous to finding the short-circuit current for use in Norton equivalent circuits.

Current divider equations and resistive network rules can then be used to determine the flux through each branch of the network. The air gap magnetic flux density is then determined by dividing the flux through the branch containing the air gap reluctance by the pole face area. Application of Equation 4.11 then gives the attractive magnetic force at the pole faces.

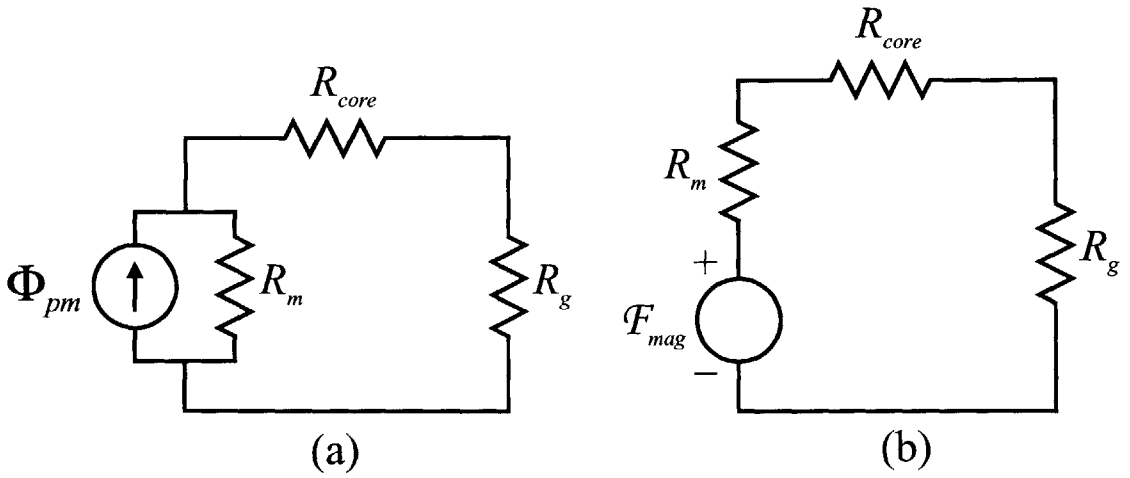

Figure 4-4: Reluctance models for the permanent magnet in the core.

An alternative model available for use with the reluctance techniques is to view the permanent magnet as an MMF source, analogous to the Thevenin equivalent circuits. Determination of the "open" circuit equivalent MMF source is easily found by multiplying the magnet thickness in the magnetization direction with the magnetization density as shown in Equation 4.15. The magnetic circuit becomes that shown in Figure 4-4(b) when the magnet is viewed as a MMF source.

$$\mathcal{F}_{mag} = M_o t_m \tag{4.15}$$

Voltage divider equations can then be used to determine the MMF across R_g, defined as $\mathcal{F}_g$. The flux through the gap is then determined by $\Phi_g = \mathcal{F}_g / R_g$. Once the flux through the circuit is found, the force on the pole face is once again found using the normal-stress form of the Maxwell stress tensor and $B_g = \Phi_g / A_p$.

The analysis of the coil-driven core could be quickly performed by replacing $\mathcal{F}_{mag}$ of Figure 4-4(b) with an MMF source of magnitude Ni and deleting the internal magnet reluctance from the circuit.

4.3 Flux Linkage

The magnetic calculations in this chapter have neglected time-varying conditions in Ampere's Law as their contribution to the analysis in magnetic-field dominated systems is small. However, the contribution of time-varying effects in the evaluation of Faraday's Law of induction is critical and provides a means for analyzing the coil voltage requirements in coil-driven systems. The magnetically-dominated system form of Faraday's Law is given in Equation 4.16 where C is an open contour that traces the coil conductor path from one terminal to the other and S is the surface bounded by the contour and an imaginary line between the coil terminals. Note the line between the coil terminals is not important as the terminals should be chosen in a region free of time-varying B-field.

$$\oint_C \underline{E} \cdot \underline{dl} = -\frac{d}{dt} \oint_S \underline{B} \cdot \underline{n}\, da \tag{4.16}$$

Evaluation of the electric field integral in Equation 4.16 leads to a voltage v between the terminals. This voltage can be induced by passing a time-varying B-field through the surface of the coil or a time-varying voltage source applied to the terminals will produce a B-field. Definition of the flux linkage, λ, as the surface integral of the B-field, Equation 4.17, allows the terminal voltage to be written as shown in Equation 4.18.

$$\lambda = \oint_S \underline{B} \cdot \underline{n}\, da \tag{4.17}$$

$$v = \frac{d\lambda}{dt} \tag{4.18}$$

The flux linkage in a magnetic actuator is typically a function of constant geometric parameters and material properties and time-varying current and position. For cases where this is true, the time-variance of the flux linkage can be simplified into the form shown in Equation 4.19 where L is the coil inductance and $\dot{x}$ is the mechanical velocity.

$$v = \frac{d\lambda}{di}\frac{di}{dt} + \frac{d\lambda}{dx}\frac{dx}{dt} = L\frac{di}{dt} + \dot{x}\frac{d\lambda}{dx} \tag{4.19}$$

Evaluation of the terminal voltage for the coil-driven core emphasized an important simplification for the calculation of the flux linkage. The N turn coil results in a surface that passes through the core N times. Several useful forms of the flux linkage with this simplification are shown in Equation 4.20 where A_{core} is the cross-sectional area of the core, B_{core} is the flux density in the core and Φ_{core} is the flux carried in the core.

$$\lambda = \oint_S \underline{B} \cdot \underline{n}\, da = N \int \underline{B} \cdot d\underline{A}_{core} = NB_{core}A_{core} = N\Phi_{core} \tag{4.20}$$

The resulting flux linkage for the coil-driven core is shown in Equation 4.21 and leads to the terminal voltage shown in Equation 4.22 as the mechanical velocity was zero.

$$\lambda = \frac{\mu A_{core} N^2 i}{t_g} \tag{4.21}$$

$$v = L\frac{di}{dt} = \frac{\mu A_{core} N^2}{t_g}\frac{di}{dt} \tag{4.22}$$

Flux linkage is covered in more detail in Section 6.3.3 where the magnet circuit is more complex with flux linkage contributions from the permanent magnet and dependence on stage velocity.

4.4 Summary

The methods for determining magnetic flux density, magnetic field intensity, and force due to coil currents and permanent magnets have been presented while working through two examples. A method for finding the coil voltage was presented and showed the dependence of coil voltage on inductance and mechanical speed. The methods presented here will be employed in Chapter 6 on the magnetic actuator configuration that drives the nanopositioner.

THIS PAGE INTENTIONALLY LEFT BLANK

Chapter 5

Casting Rubber Bearings

This chapter reviews standard rubber processing techniques that are used for large production and casting techniques that can be easily scaled from in-lab prototype production up to commercial production runs. The advantages of using the casting technique are covered, followed by a description of the rubber material selection process. The cast rubber bearing was to be tested in an existing compression fixture that had to be modified to accept the cast bearing [37]. This chapter concludes with a brief description of the novel vacuum casting method employed to cast the bearing and a comparison of the experimental stiffness results with the expected performance.

5.1 Standard Rubber Processing

Rubber that is classically suitable for application as rubber bearings is often a complex formulation of natural and/or synthetic rubber and additives. Thorough mixing of a formulation is required to ensure uniform properties throughout the material while the temperature is carefully controlled to prevent vulcanization.

Two primary techniques for combining the ingredients of the rubber formulation are mills and internal mixing machines [8]. Figure 5-1 shows a schematic view of a mill in operation. Each ingredient of the rubber formulation is placed above the mill nip and a shearing force is applied to the mixture as it is pulled in by the rolls that are rotating at slightly different speeds. The speed difference is referred to as the friction

ratio and causes the rubber to stick to one roll in a relatively uniform thickness. Several advantages of mill mixing is that a visual measure of mixture homogeneity is available while the mill is still running and the sheets directly off the mill roller are ideal when calendaring is the final process.

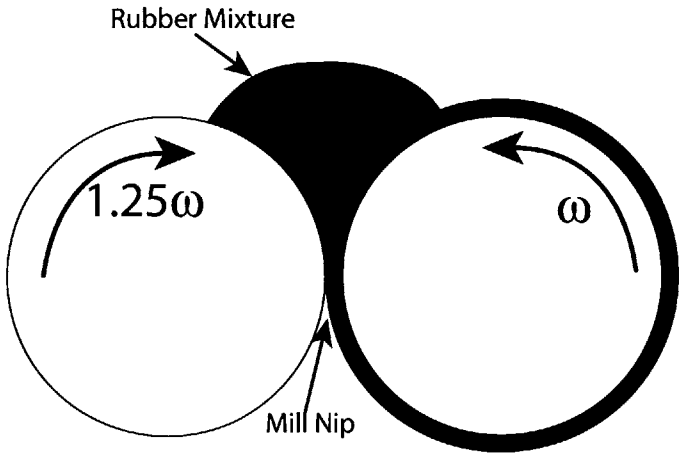

Figure 5-1: Schematic view of mill mixing.

The second mixing method is the internal mixer and has replaced the mill for most compounding operations. The internal mixer uses a combination of a rotors to mix ingredients, a ram to force ingredients into the nip, and discharge door for removing the mixture when it is ready for finally processing. The advantages of the internal mixer is that it is faster, uses less floor space, is less operator sensitive, and cleaner as the powdery materials are not open to the surrounding environment [8].

The shearing forces of the mill and internal mixer result in thorough dispersion of the ingredients and, as a byproduct, heat. Excessive heat during the mixing process can initiate vulcanization so cooling is critical and the vulcanizing agent is not usually added until the other ingredients are mixed and at the proper temperature.

The final rubber product form is typically obtained by calendaring, extruding, or molding. Calendaring is a series of vertically stacked rolls that can produce sheets of rubber of precise thickness, where thicker sheets are constructed by plying the thinner sheets. Rubber extrusions are formed by forcing the rubber mixture through a die that

gives it shape and can be a continuous process. The extrusion process is often used to wrap wire with rubber insulation, create hose, or more complex weatherstripping-type profiles. Vulcanization of calendered or extruded rubber is then performed in an autoclave or oven.

The last process that is typically used to give rubber its final form is molding. The final rubber product is obtained after forcing the rubber mixture into a mold and heated to initiate vulcanization. Once the part has reached the proper temperature, there is typically a hold time, after which the part is ejected and the process repeated.

These three rubber component production methods typically require large initial investments in equipment that is only justified by high volume production.

5.2 Why Casting?

While the rubber component production methods of Section 5.1 are sufficient for high volume production of components or general purpose rubber material, they are not well suited to the integration of rubber bearings into precision positioning devices. An alternative production method that is employed successfully in many diverse fields is casting. Casting of rubber components is a simple process that can be performed by hand and is scalable to mass production.

The casting process involves creating a mold that will restrain the liquid rubber in the desired shape until after after vulcanization occurs. Vulcanization of the liquid rubber can be initiated in a number of ways and is an important feature of the casting process. Other important features include the ability to create a preload on the bearing, conform to any surface exactly, variations in setting time can be easily obtained, and, most importantly for this work, can be easily used to create just a few parts.

5.3 Materials for Casting

The prime material candidates for use as cast rubber bearings have been developed for other applications such as rapid prototyping molds, medical device production, sealing applications, and many more. A few of the liquid rubber families that are available and possess good general characteristics for use as rubber bearings include silicones, polyurethanes, polysulfides, and polyethers. Each rubber has advantageous characteristics and the number of possible materials in the four families is almost endless. The number of families of liquid rubbers to be investigated for use in a bearing system was reduced to silicone and polyurethane to make the issue of material selection more tractable. Polysulfides and polyethers were excluded based on the general family characteristics of bad recovery from stress and very fast cure rates, respectively.

Liquid rubber properties that are desirable for the casting of rubber bearings are low viscosity, good surface wetting, good adhesion, and low shrinkage. Liquid rubber properties that are desirable in a research setting include medium working time (>2 hrs.) and short demold time. Liquid silicone rubber and polyurethane are available in a wide variety of hardness values so hardness was not of prime importance in the initial search for a suitable material. The material datasheets for many silicone rubbers and polyurethanes often do not include Young's modulus so it was estimated using the Shore A hardness that is included in most rubber material specifications and Lindley's table of material properties 3.1.

Dow Corning® 3110 RTV silicone rubber was chosen and the relevant material properties are included in Table 5.1. The 3110 RTV is a two part silicone moldmaking material for rapid prototyping and Dow Corning has a compatible primer coat that was used to ensure a strong bond with the steel bearing supports of the compression fixture.

The availability of a compatible primer coat was a major advantage for the Dow Corning product as all of the stiffness equations become invalid should the rubber separate from the supports. The supports in the compression fixture were 4112 steel

and would not have presented bonding problems. However, the cast bearing was being evaluated for use in a positioner constructed entirely of stainless steel. Stainless steels often present adhesion problems due to the low surface energy and a primer coating would be the easiest method to increase bond strength [40].

Another method that improves adhesion and should always be performed on stainless steels to maximize corrosion resistance is passivation. Passivation is a process by which a uniform protective oxide film is created on the exposed surfaces of stainless steels and all containments are removed from the surface. Passivation should be performed on all nanopositioner components prior to the application of the primer coat in all commercial applications of cast rubber bearings.

Table 5.1: Dow Corning® 3110 RTV Silicone Rubber Properties with 10:1 Catalyst 1 mix ratio.

Property	**Value**	**Units**
Hardness	45	Shore A, points
Young's Modulus	1.8	MPa
Shear Modulus	0.6	MPa
E_∞	1.0	GPa
Base Viscosity	130	Poise
Tensile Elongation	175	%
Cure	Tin Catalyst	
Working Time	2	hours
Demold Time	7	hours

5.4 Test Fixture Modifications and Mold Design

The test fixture in which the cast rubber bearing was to be tested was developed by Augusto Barton [37] for testing laminated rubber bearings in both compression and shear. The fixture accepts both a compression configuration or shear configuration and could apply compression or shear force, while measuring the displacement across the rubber bearing using a capacitance position sensor. The complete assembly that

is suspended on the rubber bearing is shown as both a CAD model and photograph in Figure 5-2. The rubber bearing can be clearly seen in Figure 5-2 with the annular geometry that was required to allow the capacitance position sensor to measure displacement at the geometric center of the bearing. Refer to Figure 3-10 for the rectangular annulus geometry definitions. A cross-sectional view of the original fixture configuration is shown in Figure 5-3 with the important parts labeled.

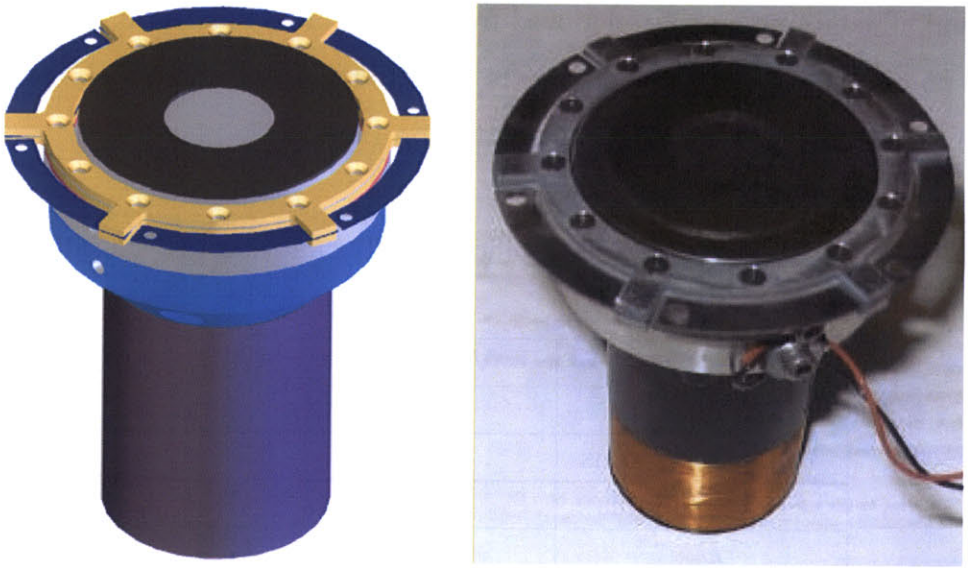

Figure 5-2: Barton's compression configuration for rubber bearings constructed by cutting the rubber pads [37].

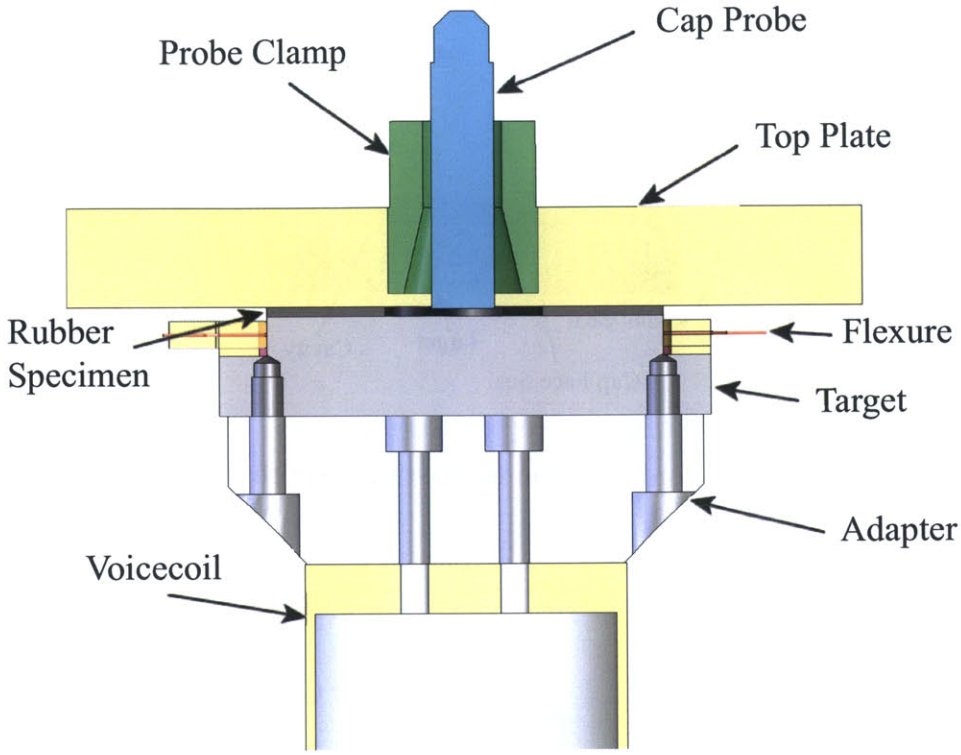

Figure 5-3: Cross-sectional view of Barton's original compression configuration including part names [37].

The cast bearing had to be compatible with the compression test fixture with as little modification to the original fixture as possible. This constraint meant the available force, approximate geometry, and measuring method were all predetermined and any molded bearing would have to conform. A series of concepts for sealing a casting chamber and fixing the bearing in the fixture were developed. Some critical issues during concept selection were the required compression force for o-ring face seals, extraction of o-rings after casting, how quickly the mold could be reworked to produce different bearing thicknesses, the determinism of the bearing thickness and whether the flexure was removable without destroying the flexure. The concepts where then evaluated and the molding configuration employed is shown in Figure 5-4, with testing configuration in Figure 5-5. The axisymmetric mold volume is shown in Figure 5-4 with the red outline.

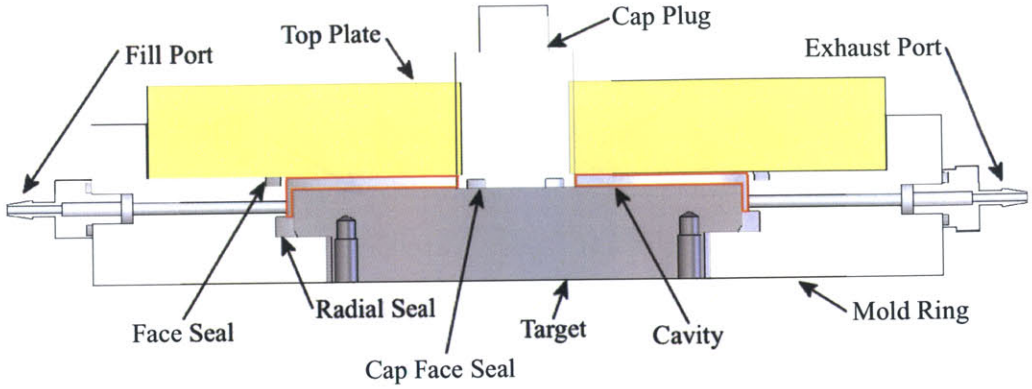

Figure 5-4: Mold configuration for casting compression specimens.

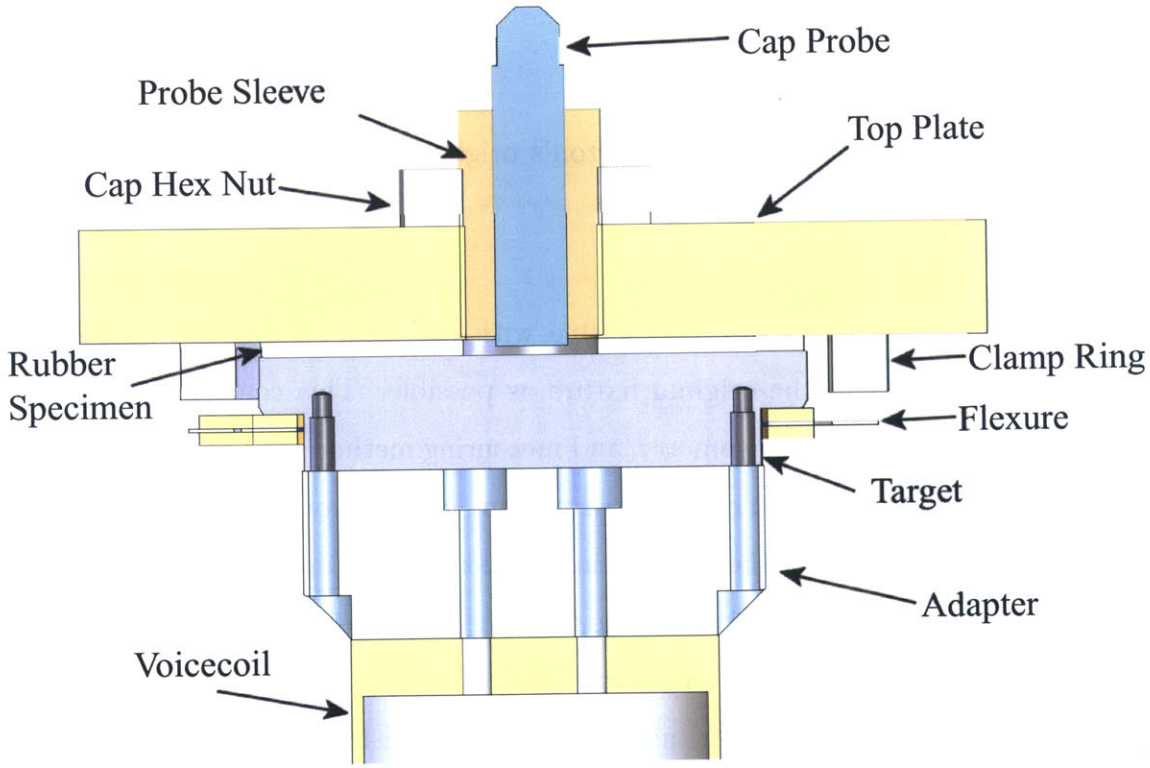

Figure 5-5: Cast bearing compression testing configuration.

The inner and outer diameters of the cast compression specimen were determined by the preexisting fixture and molding method, leaving the thickness of the cast

layer as the only remaining variable for determining the cast bearing stiffness. The mold ring could be quickly modified for casting thicker sections for more compliant bearings so the thinnest bearing (highest stiffness) of practical interest using the available equipment was cast first. Barton [37] found that the maximum stiffness that could be reasonably measured in the fixture was 2000 N/μm so the first cast bearing was designed to have a DC stiffness around 100 N/μm, which would allow the stiffness to increase with frequency up to 20 times and still be measurable. The cast compression bearing had a thickness of 1.8 mm and theoretical static stiffness of 110 N/μm.

5.5 Casting Process

The primary goal of the casting process is to create a rubber sheet that is firmly adhered to the supports and is devoid of any air bubbles. Accomplishing this goal requires priming the supports to promote adhesion, removing all trapped air bubbles from the liquid rubber mixture, and filling the mold completely.

The first step in preparing the supports for adhesion was to abrasively clean them with sandpaper to remove any rust or other adhered contaminates. Next was a soap and water bath to rinse away dust and machine oil. Rubbing alcohol was then used to prepare the support surfaces for the application of a thin layer of adhesion promoter supplied by Dow Corning® for use with liquid silicone rubbers. The layer adhesion promoter can be seen in Figure 5-5 as the white layer on the top plate that extends well beyond the edge of the rubber bearing.

The removal of air and complete mold filling were accomplished through the use of a vacuum pump and bell jar. A liquid rubber reservoir was placed under the bell jar with all the necessary plumbing for filling the mold in place, as shown in Figure 5-6. The bell jar and mold were then evacuated simultaneously to 25" Hg below atmospheric, which allowed most of the air trapped in the liquid rubber to escape. Valve 3 was then closed while Valve 4 was opened which allowed atmospheric pressure to slowly fill the bell jar, although the mold and buffer were still evacuated. Liquid

rubber was then forced by air pressure to flow from the reservoir to the bottom of the mold. The rubber was allowed to continue flowing until it slightly filled a buffer container in order to assure filling of the mold. The vacuum on the mold side of the reservoir was then replaced by atmospheric pressure using Valves 1 and 2. The buffer was important to ensure the mold would remain filled after the vacuum was removed as the rubber expands approximately 30% while vacuum is applied. With air pressure applied, any voids in the mold are collapsed. The rubber vulcanized under atmospheric pressure for 24 hours before the mold was opened.

The first attempt to fill the mold failed due to the liquid rubber viscosity being too high for 1/16" tubing as around 5% of the mold was filled with rubber. Upgrading all tubing that rubber flowed through to 1/8" tubing solved the problem.

Figure 5-7 shows the upgraded molding system just after the silicone rubber compression specimen was cast. The 1/16" tubing that was previously used everywhere can still be seen leading from the buffer to the aluminum platform. The small amount of rubber that flowed into the buffer is also visible in the bottom of the plastic liner inside the glass vacuum chamber.

The cast bearing is shown in Figure 5-9 just after the mold was disassembled and the compression setup removed. The two o-rings that sealed the chamber can be seen, as well as the excess rubber that had to be trimmed from around the target. The layer of adhesion promoter can also be seen in Figure 5-5 as the white layer on the top plate that extends well beyond the edge of the rubber bearing.

The compression test specimen has been attached to the adapter, flexure, and voice coil and is ready to be placed in the unmodified portion of Barton's fixture and tested.

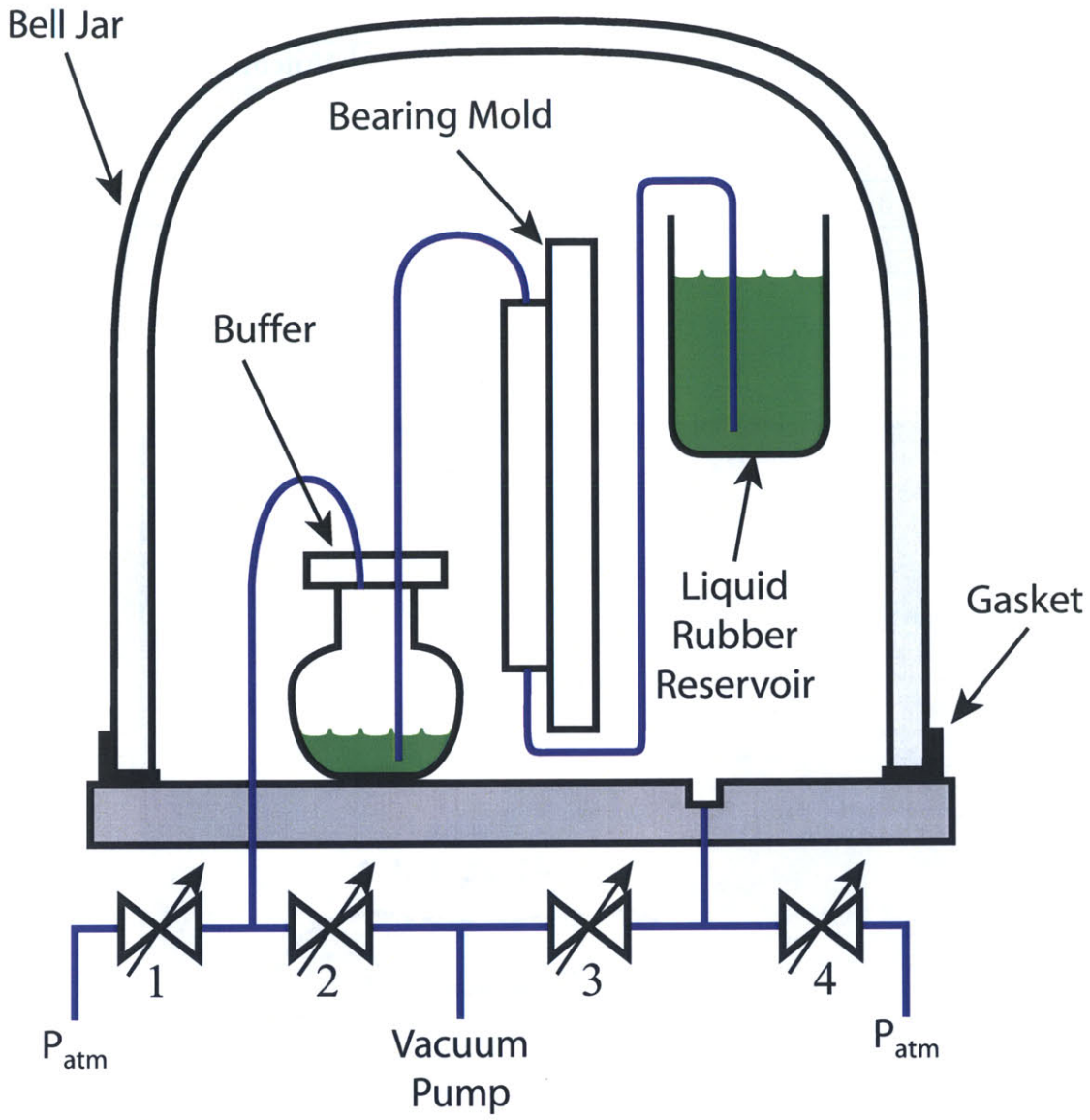

Figure 5-6: Bearing casting apparatus.

Table 5.2: Valve configurations during the different steps in the casting process.

Valve Number	**Degassing**	**Mold Filling**	**Vulcanization**
1	Closed	Closed	Open
2	Open	Open	Closed
3	Open	Closed	Closed
4	Closed	Open	Open

Figure 5-7: Physical implementation of the bearing casting apparatus of Figure 5-6

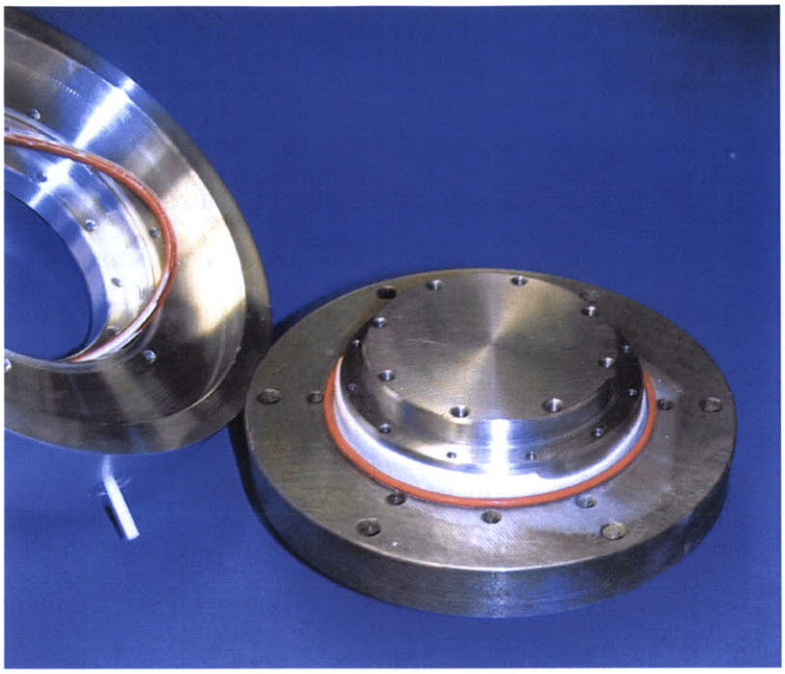

Figure 5-8: Cast silicone rubber compression bearing immediately after removal from the mold.

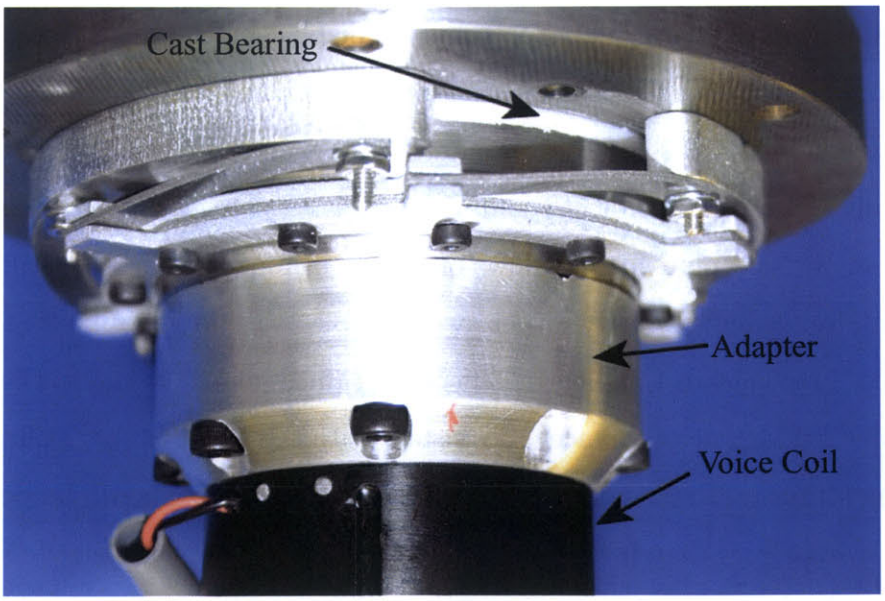

Figure 5-9: Photo of the cast rubber bearing after being fixtured in the compression configuration of Figure 5-5.

5.6 Experimental Results for Cast Bearing

A BEI LA24-33 voice coil was used to drive the compression fixture with a peak-to-peak force of 14.2 N as the current was limited to 1 amp to keep resistive heating in the coils low. The equipment available for measuring the specimen stiffness included an ADE 2805 capacitance position sensor, ADE 3800 cap sensor electronics, Kepco BOP 50-4M current amplifier, an HP 35665A Dynamic Signal Analyzer (DSA), and a Tektronix 502A Differential Amplifier. The DSA was used to sweep the driving frequency of the voice coil from 1 Hz to 10 kHz with integration of 5 cycles per data point to improve noise rejection. The experimental stiffness of the cast rubber bearing is shown in Figure 5-10 . The stiffness at 1 Hz was 123 N/μm which compares quite favorably to the expected DC stiffness of 110 N/μm. Lower frequencies than 1 Hz were not measured as the slope of the stiffness is very flat and the resulting decrease in stiffness as the frequency approaches DC will be minimal.

The slope of the stiffness variation with frequency is approximately +1.1 decades per decade away from the break points and it is evident either a fractional order model or a series of poles and zeros are needed to accurately model the rubber behavior. The experimental stiffness data is approaching the displacement measuring capability of the system around 1 kHz which makes drawing many conclusions above this frequency difficult except in the case of the resonant stiffness zeros at 2.7 kHz. It is assumed the resonant zeros are a result of the 0.41 kg mass suspended on the rubber bearing. The mass suspension on a spring allows one to determine the effective stiffness, mass, or resonant frequency given the other two variables. Taking the mass and resonant frequency as known leads to a bearing effective stiffness of 125 N/μm at the resonance. The effective stiffness at resonance is consistent with the static rubber stiffness and not the bearing stiffness at resonance. Further study of this issue should be performed by obtaining using a high-bandwidth capable capacitance distance sensor (current probe BW = 5 kHz), retesting the current 1.8 mm cast bearing, as well as testing thicker cast bearings to see the effect on the resonant frequency. This further study of the compression fixture was not performed in this work due to limited time.

$$k_{eff} = 4m\left(f_n\pi\right)^2 \tag{5.1}$$

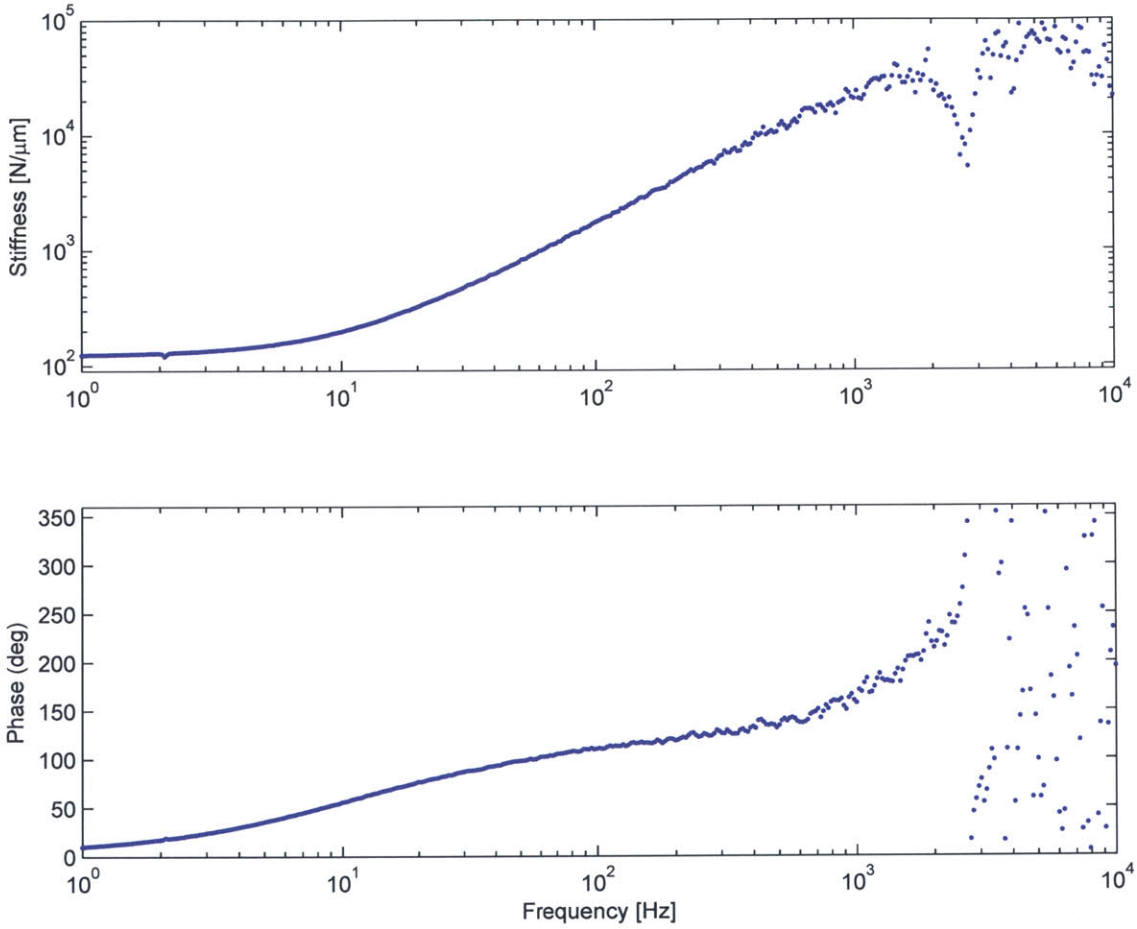

Figure 5-10: Experimental stiffness variation with frequency for the cast 1.8mm pad of 3110 RTV silicone rubber.

THIS PAGE INTENTIONALLY LEFT BLANK

Chapter 6

Nanopositioner Design

The conceptual development of the nanopositioner was performed while keeping in mind the intimate relation between the electromagnetics and the rubber bearings. This chapter describes each of the analysis activities and design processes utilized in developing the nanopositioner. Although some activities are described as if they are independent of other considerations, the tight packaging and nature of the nanopositioner tightly couples the mechanical and magnetic designs, requiring an iterative design process.

This chapter first describes the rubber bearing construction methods that were considered for use in the nanopositioner. Next, flux steering actuator configurations suitable for the nanopositioner were considered and the best actuator configuration selected for an in-depth analysis of the pertinent magnetic governing equations. The source and strength of the actuator nonlinearities are investigated and guidelines developed to limit nonlinearity due to geometry. A discussion of the rubber bearing design and the expected bearing performance in all 6 degrees of freedom follows to ensure the bearing system would be sufficient for precision applications. The nanopositioner design details are then reviewed including design trade-offs, modeling issues and other constraints. The chapter ends with a summary of alternative nanopositioner configurations that would utilize material from this thesis.

6.1 General Bearing Concepts

The initial step in preparing to design the nanopositioner was to consider the methods available for constructing the rubber bearing. The obvious methods are bonding of rubber pads and casting. An additional interesting idea was to stack standard and readily available o-rings one on top of another around a square or circular post. The question that needed to be answered was whether the stacked o-rings would provide sufficient constraint stiffness in the radial direction to be practical in a nanopositioner. The two cases of particular interest are the o-rings on a round post and the o-rings on a square post suspending a stage of the inverse post geometry.

Figure 6-1 shows two possible o-ring spacings for suspending a stage. Figure 6-1(a) shows an o-ring spacing scheme that will have a stiffness that approaches that of a solid sheet when the spacing is less than a o-ring thickness due to the constraint each bulging o-ring will place on the others. This interfering configuration will be referred to as having bulging interference. The two stiffness limits of the bulging interference configuration are the continuous sheet stiffness and the stiffness of n single o-rings with no bulging interference where n is the number of o-rings in the stack. When the o-rings are very tightly spaced the o-ring stack stiffness will approximate a continuous rubber sheet. Large spacing between the o-rings will eliminate the stiffening effect of the bulging interference and the stiffness will be that of n single o-rings. Literature is available that discusses the radial stiffness of a continuous rubber sheet in the gap although no such work is available for the non-interfering case [4]. Determination of the lower limit for stack radial stiffness is important in deciding whether an o-ring stack is feasible so a numerical approximation was developed and is described next.

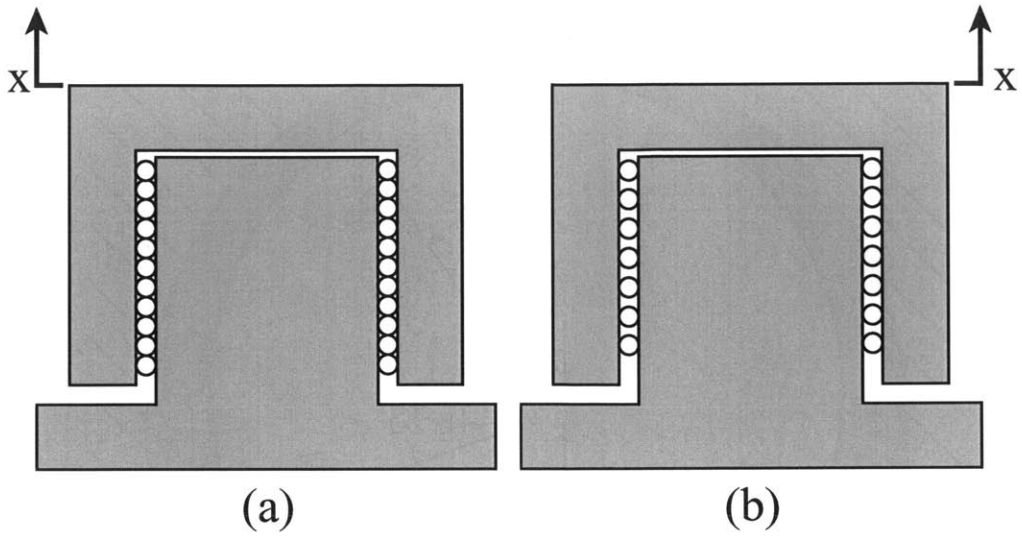

Figure 6-1: Cross-sectional view of a stage suspended on stacked o-rings with (a) and without (b) bulging interference.

6.1.1 O-ring Stiffness Analysis

The stiffness of solid rubber rollers was developed using the plane strain assumption and the inverse of the positioning stage problem shown in Figure 6-1. Rather a post was suspended in a bore with a disturbance force applied to the post as shown in Figure 6-2. The plain strain assumption for the round post means the azimuthal strain is small and can be neglected. This allows the radial stiffness of o-rings on a round post to be determined by discretizing the o-ring into sections of length $r\ d\theta$, summing the force across each section, and numerically differentiating with respect to the center-to-center displacement, x_p, of Figure 6-2. Note that the squeeze ratio (x_i/d) is a function of θ so each discretized segment of the o-ring has a different squeeze ratio and therefore contributes a different constraining force that is dependent on θ. The constraining force for each discretized section of the o-ring is derived from an incremental form of the force-displacement equation for solid rubber rollers (Equation 3.28). The geometrical assumptions are that the o-ring exactly fills the void between the post and the tube and is free to bulge laterally, as expected for solid rubber rollers in compression with no lateral constraints.

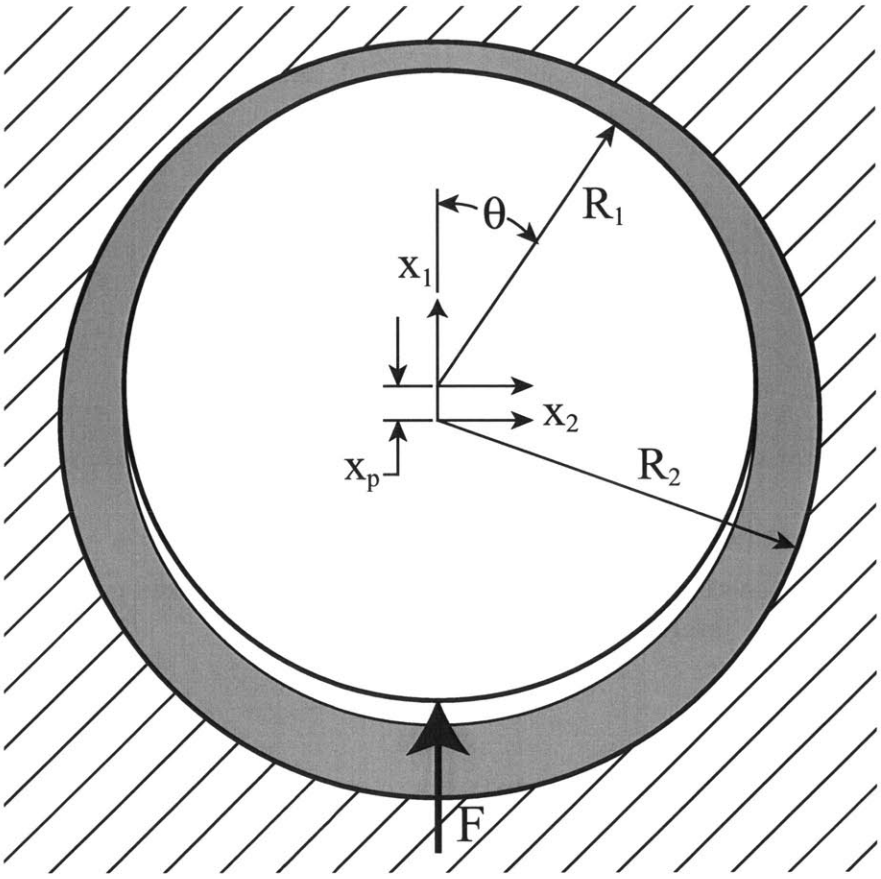

Figure 6-2: Diagram of single o-ring on a post inside a bore with a disturbance force applied to the post.

The steps in approximating the radial stiffness of a single o-ring on a post across a range of displacements is as follows:

- Define the range of center-to-center displacements, x_p.
- Discretize the o-ring into sections of length $r\ d\theta$.
- Calculate the squeeze ratio of each section x_i/d for each x_p.
- Evaluate the force per unit length required to reach the squeeze previously found using Equation 6.1 which is the incremental form of the force required to compress a solid rubber roller to a given squeeze ratio.

$$F_i = dE_o \left[1.25 \left(\frac{x_i}{d} \right)^{3/2} + 50 \left(\frac{x_i}{d} \right)^{6} \right] \tag{6.1}$$

- Sum the force around the o-ring to get the total force, F, necessary to displace the post in the bore by x_p.
- The stiffness is then determined by differentiating the total required force with respect to the displacement.

Figure 6-3 shows the necessary force to reach center-to-center displacements up to 0.5 mm for a 25 mm post and single 2 mm thick o-ring. Differentiation of the force with respect to the displacement leads to the stiffness plotted in Figure 6-4. A displacement of 0.4 mm corresponds to 20% squeeze and is the maximum recommended squeeze on standard o-rings for most applications. If the maximum squeeze recommendation is followed then the maximum radial stiffness of a single o-ring would be approximately 0.14 N/μm. The m-file and two functions used to perform this calculation are included in Appendix A.2.

The stiffness of a single o-ring with no bulge interference and 20% squeeze is much too low to be considered for use in the nanopositioner. The minimum constraint stiffness in precision machine tools is around 20 $N/\mu m$ and was taken as the target constraint stiffness for the positioners throughout this work [38]. Achieving the needed constraint stiffness would require 145-2 mm o-rings in a device less than 50mm long. Thus only configurations with bulging interference can be used to create a practical rubber bearing from a stack of o-rings. Effective design of such a bearing will require determination of the effect of bulging interference on the radial stiffness.

The lateral and tilting stiffness determinations for the square post without bulging interference are much easier to determine as they only require the use of use of Equation 3.28. The lateral stiffness is simply n times the stiffness of single rubber roller of length L, where L is the length of one side of the square post. Determination of the tilting stiffness simply requires including the varying displacement each o-ring will encounter and scaling each stiffness dependent on the distance between the o-ring and the axis of rotation of the stage.

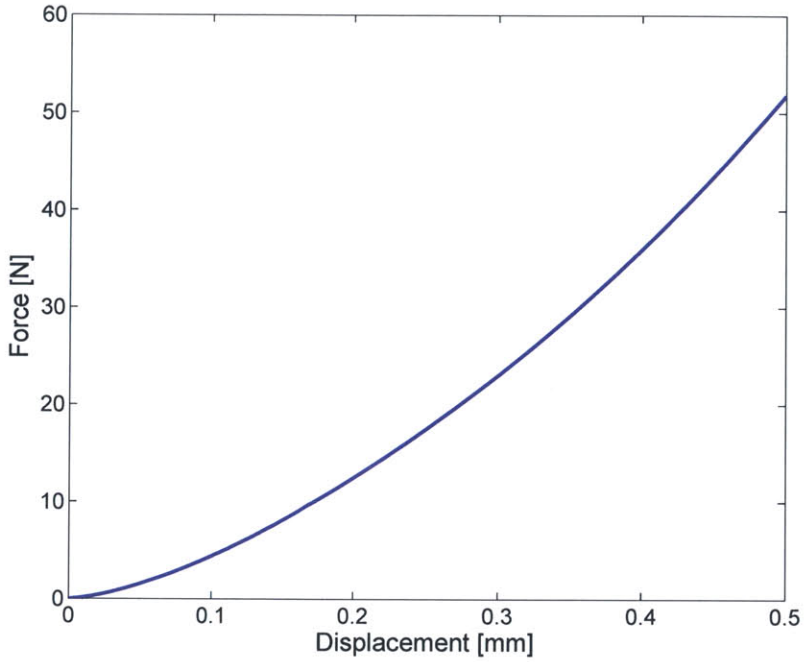

Figure 6-3: Required force to reach a specified center-to-center displacement of the circular post suspended on a single o-ring inside a bore.

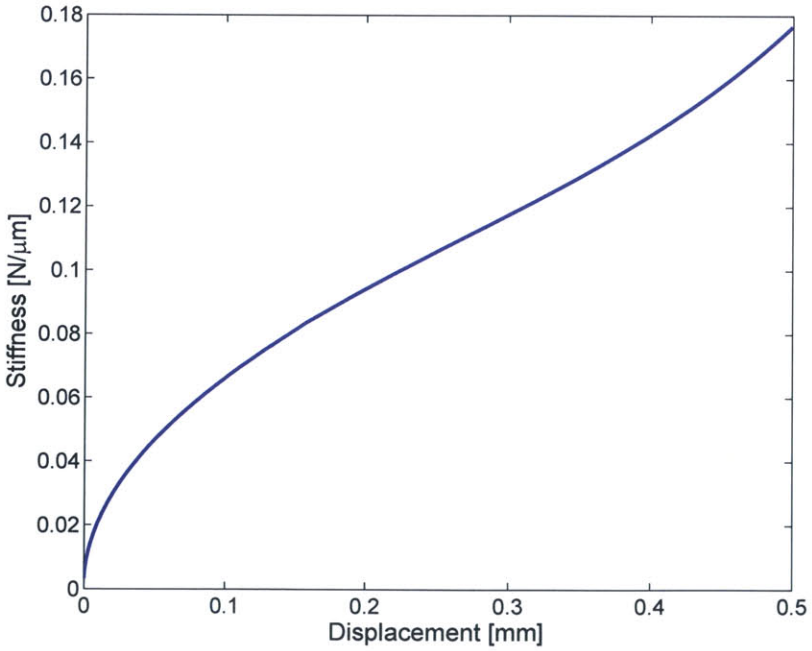

Figure 6-4: Radial stiffness of the circular post relative to the bore while suspended on a single o-ring.

6.2 Flux-steering Actuator Configurations

A key feature of the magnetic nanopositioner is the normal-stress, flux-steering, permanent magnet biased actuator that applies a force that is linear in coil current and stage displacement. The configuration characteristics of an electromagnetic actuator that make the force linear in current and displacement are an invariant bias flux, differential excitation, and natural subtraction. Normal stress actuators that have all three of these characteristics are referred to as hard linearized actuators [35]. Three hard-linearized magnetic configurations were evaluated for use in the nanopositioner.

6.2.1 Candidate Magnetic Configurations

The first configuration was proposed by Studer for use as a magnetic bearing and is shown in Figure 6-5. Studer's objective was to suspend a rotor radially by fixing the end caps of the figure to the rotor. The primary disadvantage of Studer's configuration for the nanopositioner was due to the practicality of integrating a rubber bearing and winding the coil around the poles.

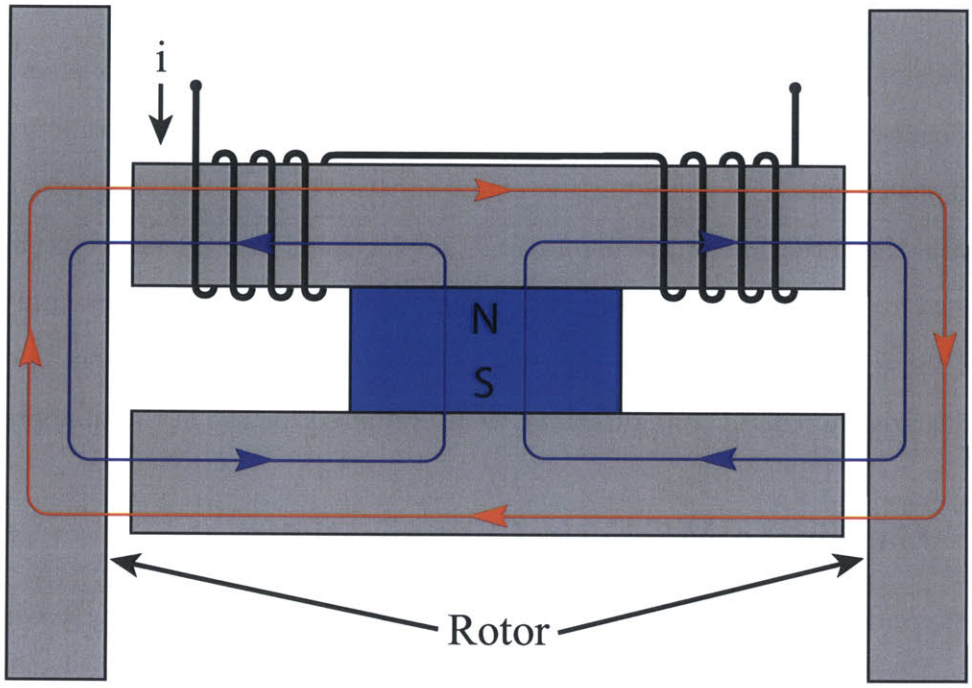

Figure 6-5: Hard-linearized magnetic configuration proposed by Studer [47].

The second configuration that was considered was used by Lu in his ultra-fast tool servo [35] and is shown in Figure 6-6. Lu's configuration was optimal for maximizing force on a small payload with the penalty of a relatively large package. Manufacturing and assembly of the overall package is more complex resulting in higher manufacturing costs than the other configurations.

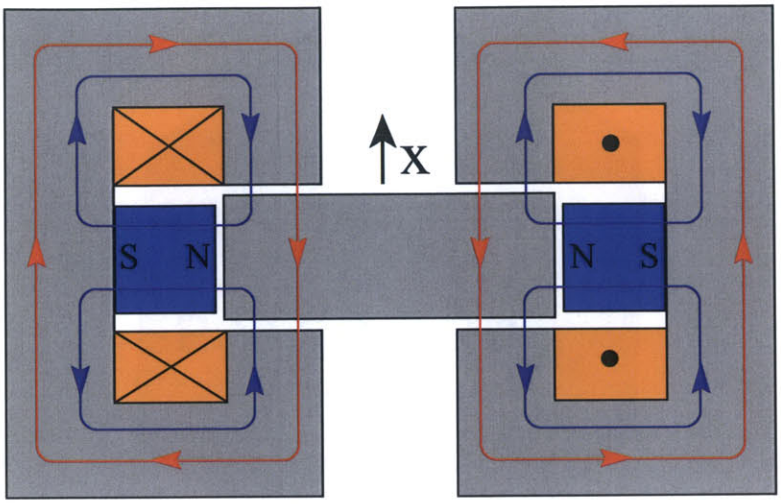

Figure 6-6: Lu's configuration that is optimal for applying large forces to a small payload.

The last configuration considered was suggested by Professor Trumper and was the configuration used in the nanopositioner. This configuration eliminates the rubber bearing and coil packaging complications of Studer's design by sweeping the cross-section of Figure 6-5 axisymmetrically. Reconfiguring the coils and merging the resulting center pole gives the geometry shown in Figure 6-7, where the end caps and coils have been removed to reveal the interior geometric detail of the poles. Figure 6-8 shows a cross-sectional view with the coil flux path in red and the permanent magnet flux paths in blue.

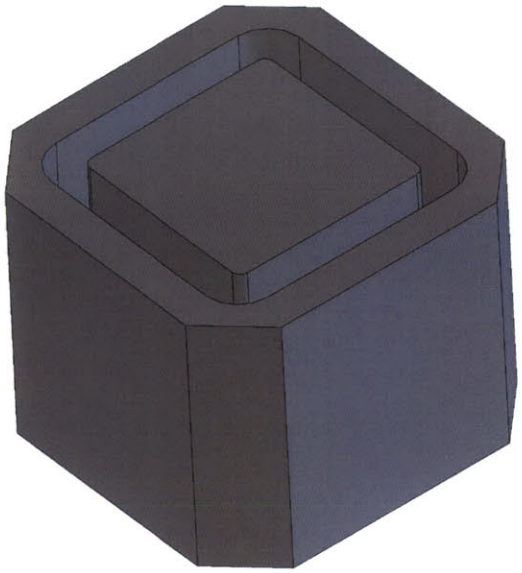

Figure 6-7: Isometric view of the nanopositioner magnetic configuration.

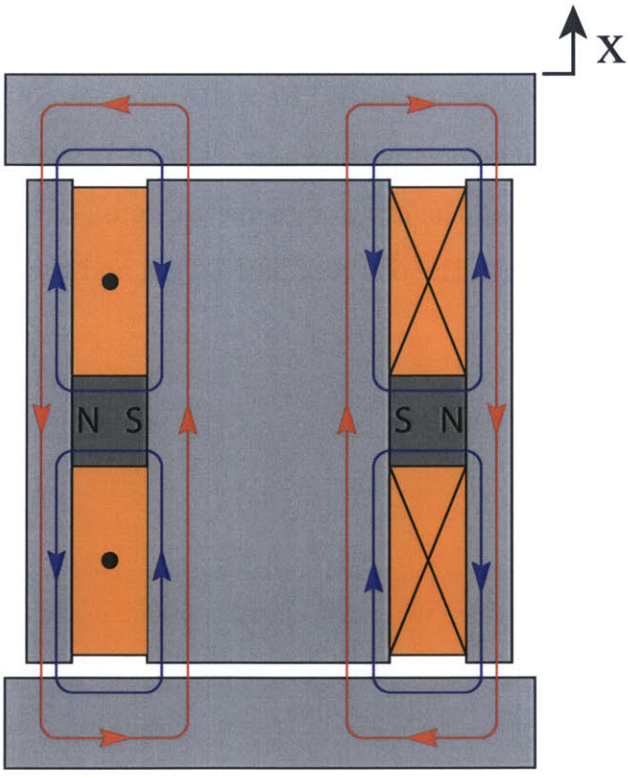

Figure 6-8: Diagram of the coil and magnetic flux paths in the nanopositioner.

6.3 Nanopositioner Magnetic Analysis

The force as a function of current and displacement for the nanopositioner was determined using a combination of the Maxwell equation approach and the reluctance method. The next section develops the equations describing the force with the following variable definitions:

- The permanent magnet length from the north to south pole is h_m and the total magnet area is A_m.
- A_p is the pole face area of the inner or outer pole while the total force producing area is $2A_p$.
- g_{nom} is the nominal length of the air gaps.
- The upper and lower air gap lengths are $g_{nom} + x$ and $g_{nom} - x$, respectively.
- The upper and lower coils each supply $Ni/2$ amp-turns in complementing directions around the core.
- The magnetic flux density at the permanent magnet face is B_m and is defined as:

$$B_m = \mu_o \left(H_m + M_o\right) \tag{6.2}$$

- The flux through the magnet, upper air gap, and lower air gap are given by Φ_{PM}, Φ_u, and Φ_l, respectively.

6.3.1 Maxwell Approach

Applying Ampere's Law around the contours, 1 through 3, of Figure 6-9 and Gauss's Law to surface 4 results in the following equations where the only simplifications are neglecting the leakage path and iron pole piece reluctances:

$$H_l = \frac{M_o A_m \, h_m \, \left(g_{nom} + x\right)}{2\left(h_m \, A_p \, g_{nom} + A_m \left({g_{nom}}^2 - x^2\right)\right)} + \frac{Ni}{4 g_{nom}} \tag{6.3}$$

$$H_u = \frac{M_o A_m \, h_m \, \left(g_{nom} - x\right)}{2\left(h_m \, A_p \, g_{nom} + A_m \left({g_{nom}}^2 - x^2\right)\right)} - \frac{Ni}{4 g_{nom}} \tag{6.4}$$

$$H_m = \frac{M_o \, A_m \, \left(x^2 - g_{nom}^2\right)}{h_m \, A_p \, g_{nom} + A_m \left({g_{nom}}^2 - x^2\right)} \tag{6.5}$$

Note the reverse magnetic field is completely independent of coil current and is always negative as the displacement will always be less than the nominal air gap.

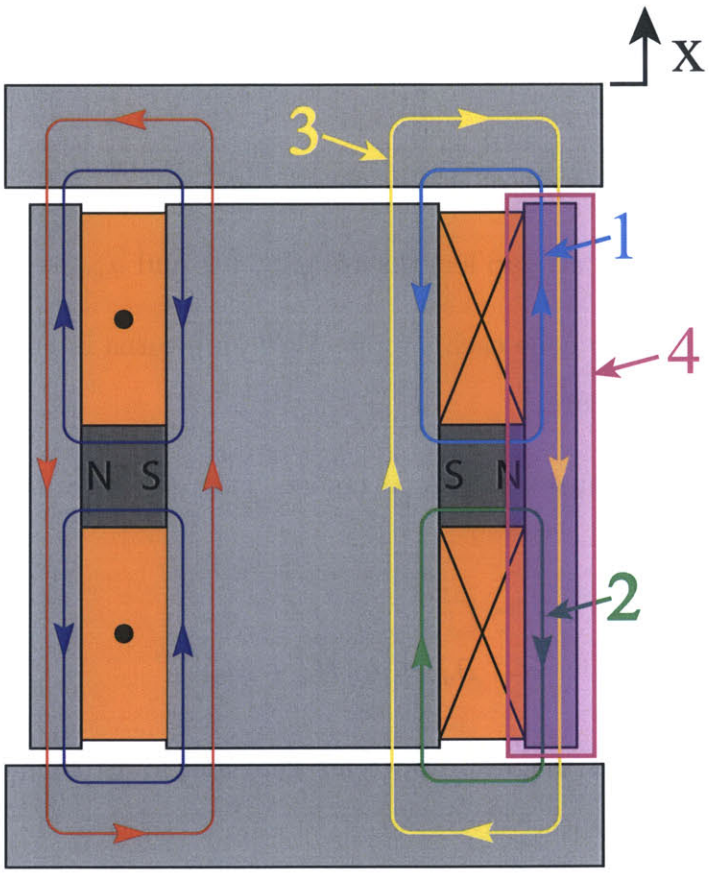

Figure 6-9: The contours and surface required for analyzing the nanopositioner configuration are displayed.

The total force on the stage is the difference between the attractive force on the upper end cap and the attractive force on the lower end cap. Equation 6.6 gives the total force on the stage as a function of current and position.

$$F_{stage} = \mu_o A_p \left(H_l^2 - H_u^2\right)$$

$$= \frac{\mu_o M_o A_m A_p h_m \left[2M_o A_m h_m g_{nom} x + NiA_p h_m g_{nom} + NiA_m \left(g_{nom}^2 - x^2\right)\right]}{2\left[A_p h_m g_{nom} + A_m \left(g_{nom}^2 - x^2\right)\right]^2} \quad (6.6)$$

Figure 6-10 plots magnetic force, Equation 6.6, for the nanopositioner as a function of displacement for three current levels. Magnetic saturation of the poles is taken into account in Figure 6-10 and is responsible for the break from the linear region for the ± 1 A and ± 2 A curves. Note that this is only magnetic force and does not take account of the rubber spring that is used in the nanopositioner. Modeling of the nanopositioner force with the rubber bearings is performed in Section 6.4.4 .

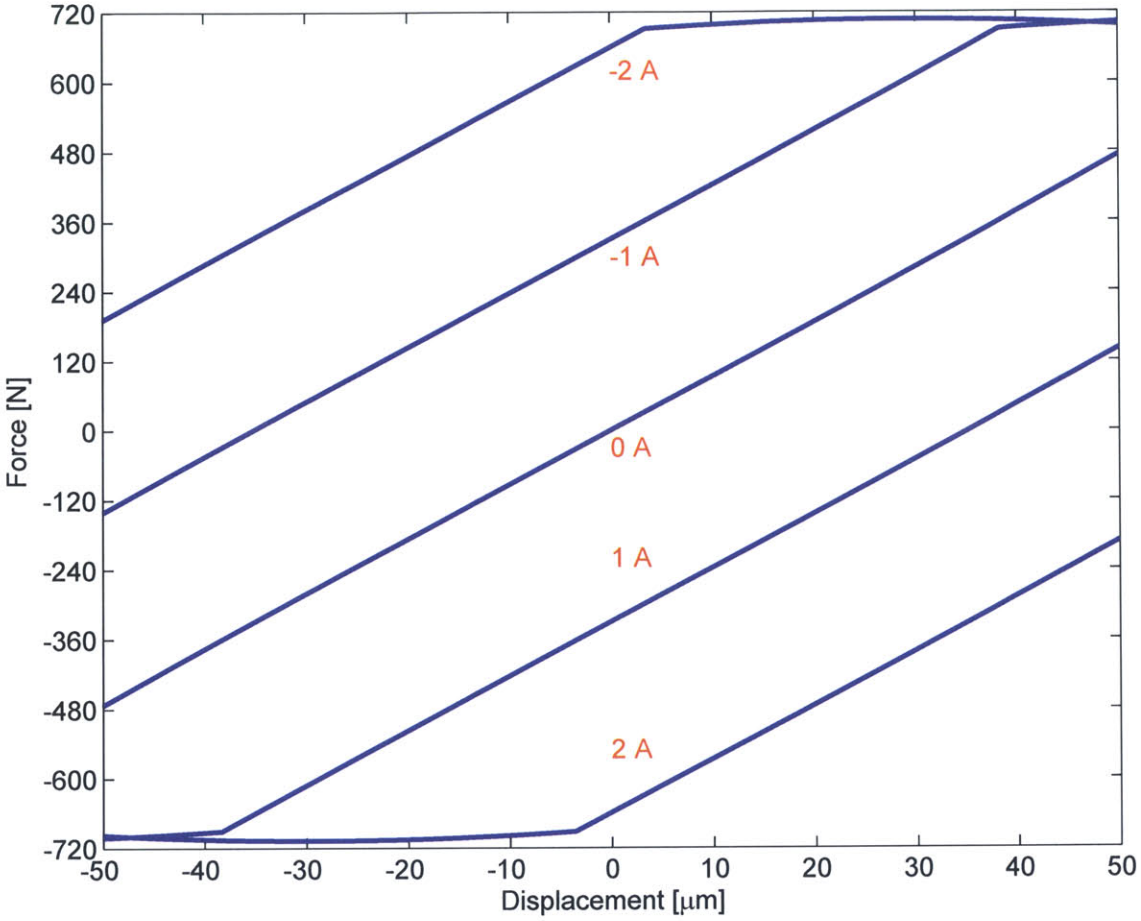

Figure 6-10: Magnetic force versus displacement parametric on current for the designed nanopositioner.

The linearized in displacement force relation is shown in Equation 6.7. The coefficient of x is the magnetic stiffness as it relates the force to stage displacement, just as the stiffness, k, does in Hooke's Law, $F = kx$. The magnetic stiffness, k_{mag}, is defined in Equation 6.8.

$$F_{lin,x} = \frac{\mu_o M_o^2 A_m^2 A_p h_m^2 g_{nom}}{\left(A_p h_m g_{nom} + A_m g_{nom}^2\right)^2} \text{ x} \tag{6.7}$$

$$k_{mag} = \frac{\mu_o M_o^2 A_m^2 A_p h_m^2 g_{nom}}{\left(A_p h_m g_{nom} + A_m g_{nom}^2\right)^2} \tag{6.8}$$

The magnetic configuration and the chosen positive x-direction leads to a positive magnetic force on the stage which is consistent with the negative magnetic stiffness. A quick thought experiment is now presented to clarify the effect of the negative stiffness in for this actuator configuration.

When the stage is in exactly the zero or null position, the fluxes in the upper and lower gaps will be exactly equal and the net force on the stage would be zero. If the stage is displaced δ in the positive x direction from null, the upper air gap length will increase and lower air gap length will decrease. More of the permanent magnet bias flux will now pass through the lower air gap, increasing the magnetic flux density and causing a positive net force on the stage. So the negative magnetic stiffness behavior is evident and the sign associated with Equationeq:magstiff is correct; a positive disturbance force leads to magnetic force that causes further divergence.

The error resulting from the linearization in displacement of the force relation varies with the ratio of magnet length to nominal air gap length and also with the ratio of magnet area to pole face area. The shape of the error curves are shown in Figure 6-11 and the RMS error resulting from variations in these two ratios are tabulated in Table 6.1. Variations in magnet length to nominal air gap length were all calculated using $A_m/A_p = 1.283$ and all variations in magnet area to pole face area were calculated with $h_m/g_{nom} = 40$, which were both the final values used in the nanopositioner.

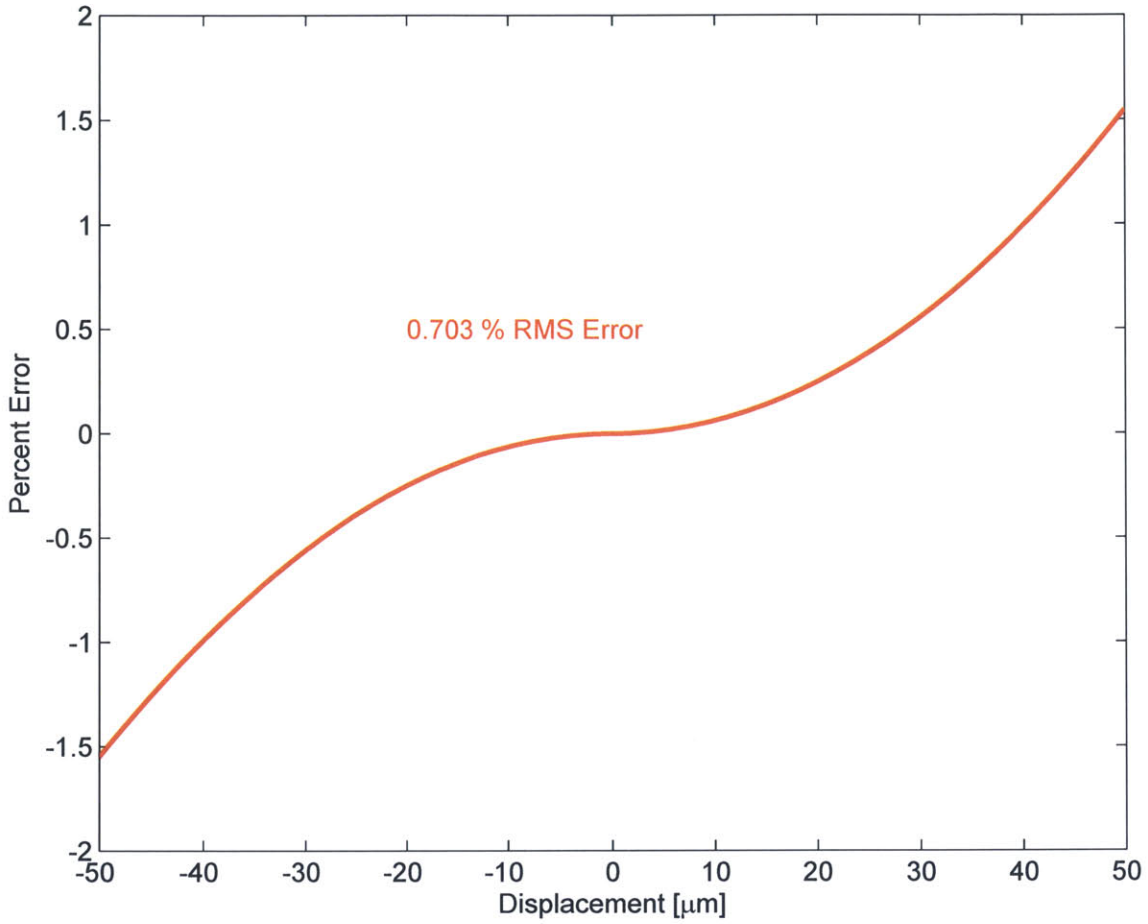

Figure 6-11: Error between the linear approximation and the full nonlinear force versus displacement relationship throughout the nanopositioners operating range for zero coil current.

Table 6.1: RMS error between the linearized and full nonlinear force versus displacement relation for varying magnet length to air gap length ratios and varying magnet area to pole face area ratios.

$\frac{h_m}{g_{nom}}$	% RMS Error		$\frac{A_m}{A_p}$	% RMS Error
1	12.1		0.2	0.113
1.1	11.6		0.5	0.28
5	4.55		0.8	0.444
10	2.55		1	0.552
20	1.36		1.1	0.606
40	**0.703**		**1.283**	**0.703**
80	0.358		1.4	0.765
100	0.278		1.485	0.808

The nonlinearities summarized in Table 6.1 can be visualized by breaking the numerator of Equation 6.6 into three separate terms. Figure 6-12 through Figure 6-14 show the contribution of each term of the separated magnetic force equation to the total force for three different current levels. The first term appears linear in displacement, while the second and third term are parabolic with the minimum or maximum at zero displacement. These two parabolic terms always have opposite concavity which results in reduced total nonlinearity when summed. Note that the nonlinearity of the total force is invisible even at the low currents of ± 0.5 A and is more of a mathematical exercise for the nanopositioner geometry chosen.

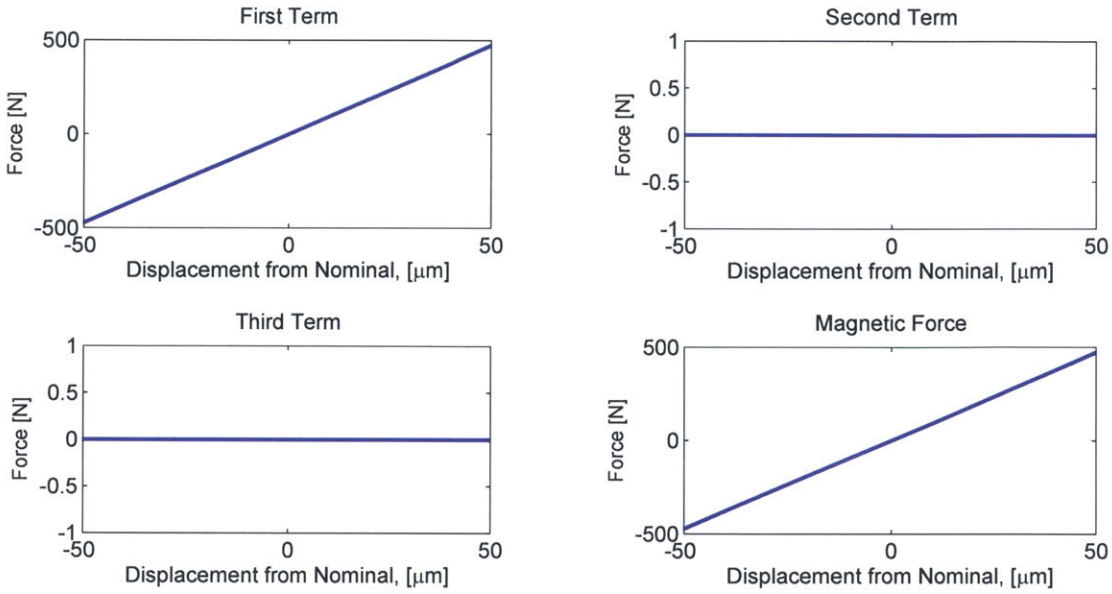

Figure 6-12: Contributions of each term of force as function of displacement for zero current (Equation 6.6).

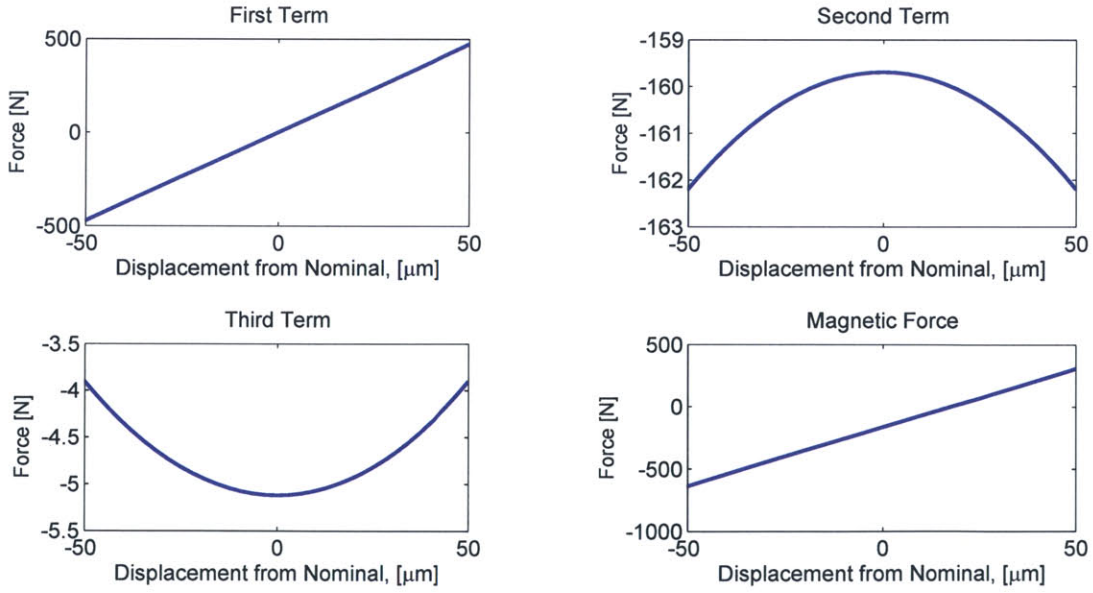

Figure 6-13: Contributions of each term of force as function of displacement for +0.5 A coil current (Equation 6.6).

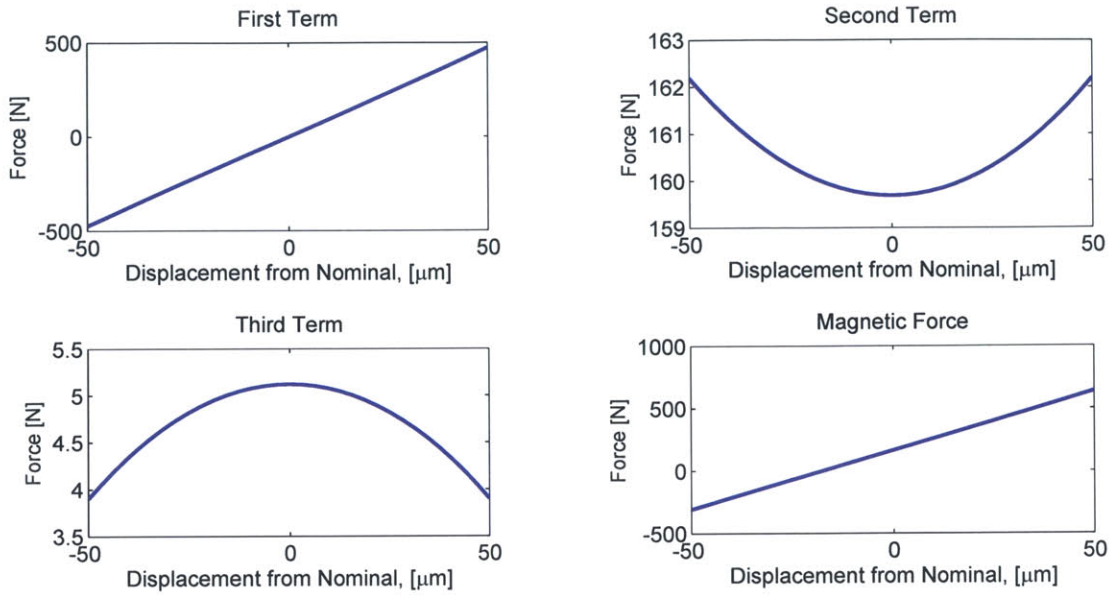

Figure 6-14: Contributions of each term of force as function of displacement for -0.5 A coil current (Equation 6.6).

The force nonlinearity due to actuator geometry has now been discussed to emphasize that some geometric configurations will drastically reduce force linearity and may require increased system controller complexity. The specific geometry chosen for the nanopositioner keeps the geometric nonlinearity to an acceptable level and enables the use of linear control techniques (see Chapter 7 for more on control.).

The nonlinearities of more importance for the chosen nanopositioner geometry are shown in Figure 6-15. The events pointed out in that figure are a result of material saturation and the fact the permanent magnet bias flux is greater than one half of the pole saturation flux. Another way of explaining the situation is that the current which magnetically saturates the upper/lower gap is not the precise current at which the lower/upper bias flux is exactly canceled by the coil flux.

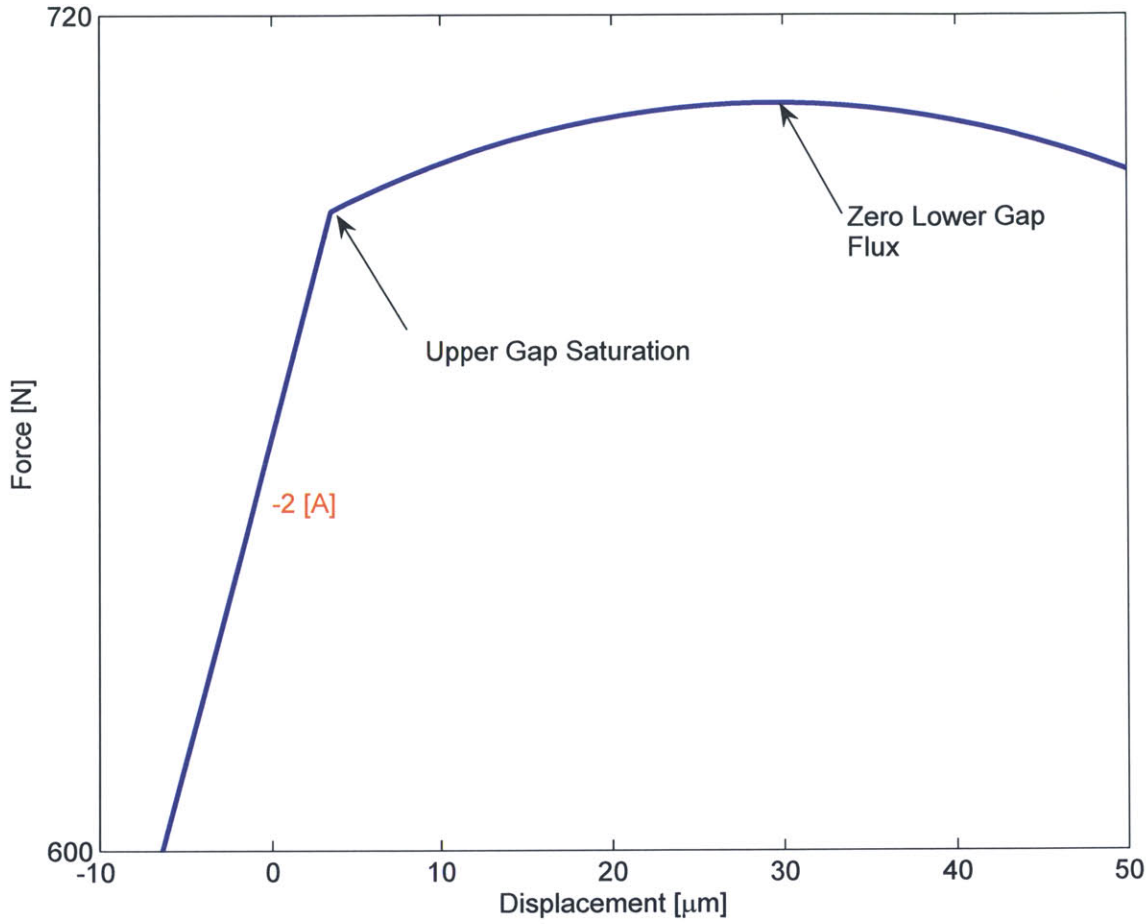

Figure 6-15: Zoomed view of Figure 6-10 that emphasizes the result of material saturation and force reversal.

Collocation of the saturation and gap flux extinguishment in current would mean the actuator was linear from exactly the minimum force to the maximum force. However, making this happen requires very precise knowledge and control of the following parameters:

- Magnet geometry including squareness.
- Permanent magnet magnetization density and flux.
- Pole piece geometry.

- Coil and magnet leakage pathes.
- Pole piece magnet permeability and saturation.

Precise control of all of these parameters is very difficult, if not impossible, so the question becomes: "Which side of pole saturation should the flux in the gap be driven to zero on?" Lu recommends an over-biased design to increase the gain from current to force, resulting in an more energy efficient design [35]. The ratio of biasing flux to coil flux was set to 1.3 to increase the current to force gain in exchange for a small decrease in maximum force that can be obtained linearly with current.

The variation of magnetic force with current is shown in Figure 6-16 for three positions. Magnetic saturation is again accounted for and with the assumed coil direction shown in Figure 6-9 a positive current leads to a positive net force on the stage.

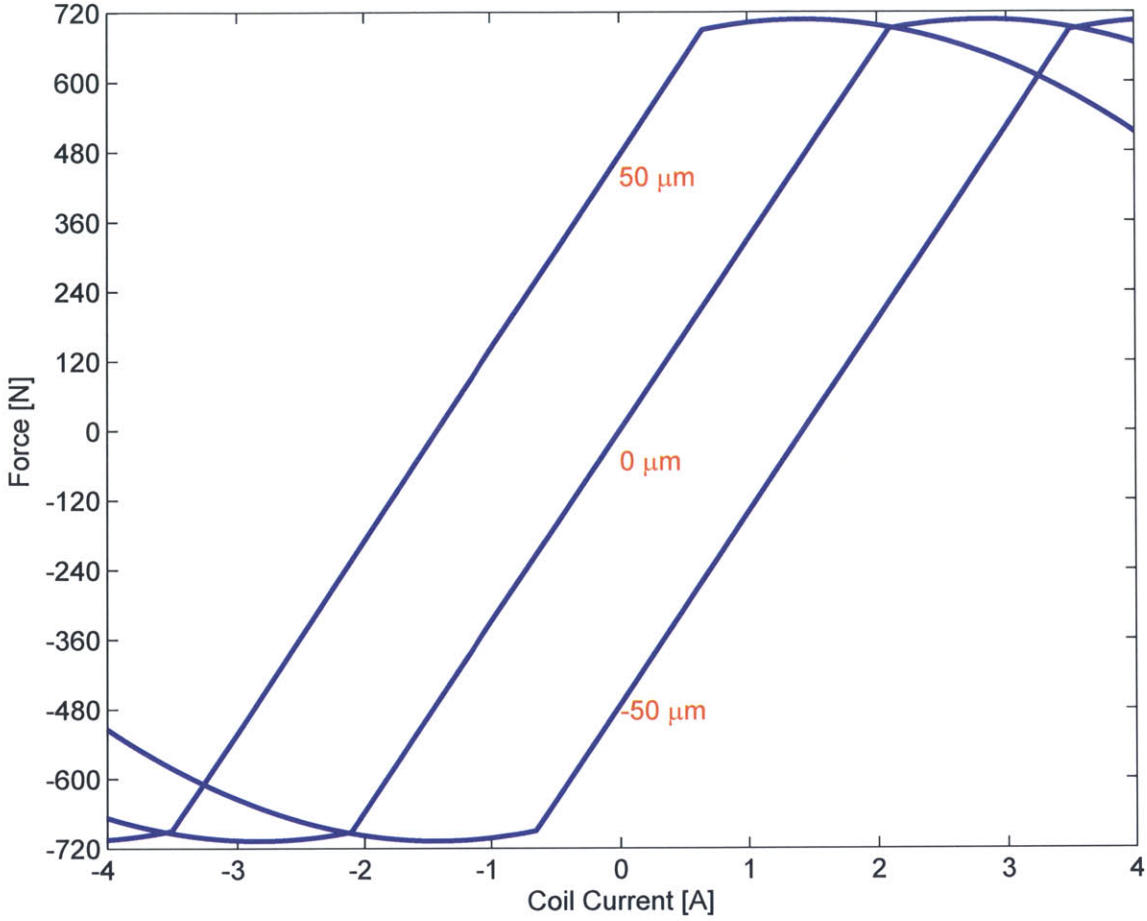

Figure 6-16: Magnetic force versus coil current parametric on displacement for the designed nanopositioner.

Figure 6-16 shows the force is linear in current, when a pole is not saturated, and Equation 6.9 is the linearization of the force relation for current. Conventional motor specifications include a proportionality constant that allows one to find the output force or torque directly if the coil current is known (i.e. $T = k_\tau i$). This proportionality constant for the nanopositioner is the force constant and is defined in Equation 6.10.

$$F_{lin,i} = \frac{\mu_o M_o A_m A_p h_m N}{2\left(A_p h_m g_{nom} + A_m g_{nom}^2\right)} \text{ i} \tag{6.9}$$

$$k_f = \frac{\mu_o M_o A_m A_p h_m N}{2\left(A_p h_m g_{nom} + A_m g_{nom}^2\right)} \tag{6.10}$$

The flux through the upper gap due to the permanent magnet was determined during the Maxwell equation analysis as

$$\Phi_{PM,upper} = \frac{\mu_o M_o A_m A_p h_m \left(g_{nom} - x\right)}{2\left(A_p h_m g_{nom} + A_m \left(g_{nom}^2 - x^2\right)\right)} \tag{6.11}$$

The flux through the lower gap due to the permanent magnet was determined as

$$\Phi_{PM,lower} = \frac{\mu_o M_o A_m A_p h_m \left(g_{nom} + x\right)}{2\left(A_p h_m g_{nom} + A_m \left(g_{nom}^2 - x^2\right)\right)} \tag{6.12}$$

And the flux through the upper and lower gaps due to the coil the same and given as

$$\Phi_{coil} = \frac{\mu_o N A_p i}{4 g_{nom}} \tag{6.13}$$

The flux linkage, λ, is found by considering the direction and magnitude of each of the fluxes that pass through the coils. The flux due to the coil is linked by the coil N times, while the flux in the upper gap due to the permanent magnet is linked by the upper coil only and is in the opposite direction of the coil flux. The lower gap flux from the permanent magnet is linked only by the lower coil and is in the same direction as the coil flux. The resulting flux linkage is given in Equation 6.14.

$$\begin{aligned}
\lambda &= \frac{\mu_o N^2 A_p i}{4 g_{nom}} - \frac{\mu_o M_o A_m A_p h_m \left(g_{nom} - x\right) N}{4\left(A_p h_m g_{nom} + A_m \left(g_{nom}^2 - x^2\right)\right)} + \frac{\mu_o M_o A_m A_p h_m \left(g_{nom} + x\right) N}{4\left(A_p h_m g_{nom} + A_m \left(g_{nom}^2 - x^2\right)\right)} \\
&= \frac{\mu_o N^2 A_p i}{4 g_{nom}} + \frac{\mu_o M_o A_m A_p h_m N x}{2\left(A_p h_m g_{nom} + A_m \left(g_{nom}^2 - x^2\right)\right)}
\end{aligned} \tag{6.14}$$

The form of Equation 6.14 is convenient for determining the inductance and speed voltage as the first term is independent of position so it does not affect the speed voltage and the second term independent of current so it does not affect the coil

inductance. The inductance and speed voltage are calculated in Section 6.3.3

6.3.2 Reluctance Approach

The nanopositioner was also analyzed using the reluctance approach for comparison with the Maxwell method equations. The reluctance model for the nanopositioner is shown in Figure 6-17. The pole reluctance and leakage flux are neglected and the permanent magnet is viewed as an MMF source. Three equations are found using the Kirchoff's current law at node A for flux and Kirchoff's voltage law around loops 1 and 2 for MMF resulting in the following three equations:

$$\Phi_{PM} = \Phi_u + \Phi_l \tag{6.15}$$

$$\mathcal{F}_{mag} - 2R_u\Phi_u - \frac{Ni}{2} - R_m\Phi_m = 0 \tag{6.16}$$

$$\mathcal{F}_{mag} - 2R_u\Phi_u + \frac{Ni}{2} - R_m\Phi_m = 0 \tag{6.17}$$

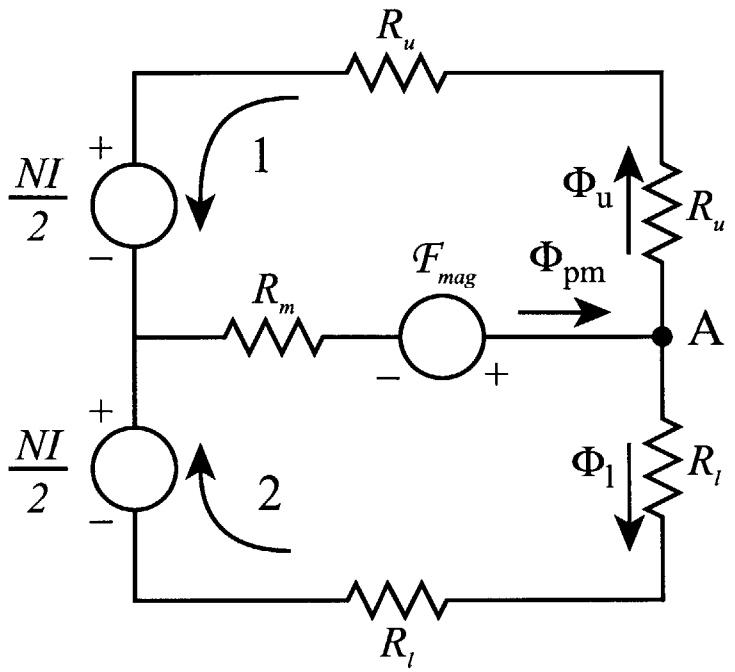

Figure 6-17: Reluctance model of the flux-steering actuator employed in the nanopositioner.

The three equations are solved to determine the fluxes through each path and are given in Equations 6.18-6.20.

$$\Phi_{PM} = \frac{2\mathcal{F}_{mag}\left(R_u + R_l\right) + Ni\left(R_u - R_l\right)}{2\left(R_m R_l + R_u R_m + 2R_u R_l\right)} \tag{6.18}$$

$$\Phi_u = \frac{2\mathcal{F}_{mag} R_l - Ni\left(R_m + R_l\right)}{2\left(R_m R_l + R_u R_m + 2R_u R_l\right)} \tag{6.19}$$

$$\Phi_l = \frac{2\mathcal{F}_{mag} R_l + Ni\left(R_m + R_u\right)}{2\left(R_m R_l + R_u R_m + 2R_u R_l\right)} \tag{6.20}$$

The total force on the stage is now found using Maxwell's stress tensor (Equation 6.21) in a magnetic flux form and the flux through the upper and lower gaps allow quick determination of the flux linkage (Equation 6.22). The upper gap flux is only linked by the upper coil and the lower gap flux is only linked by the lower coil. The

force on the stage given in Equation 6.21 is numerically equivalent to Equation 6.6 and is easily calculated once the geometry and other parameters of the magnetic circuit have been determined.

$$F_{stage} = \frac{\Phi_l^2 - \Phi_u^2}{\mu_o A_p} \tag{6.21}$$

$$\lambda = \frac{N\left(2NiR_m + NiR_u + NiR_l + 2\mathcal{F}_{mag}\left(R_u - R_l\right)\right)}{4\left(R_m R_l + R_m R_u + 2R_u R_l\right)} \tag{6.22}$$

6.3.3 Inductance and Speed Voltage

Thus far only the DC operation of the actuator has been considered. Determination of the force as a function of current and displacement was performed by assuming the coil would provide some number of amp-turns. Operation at frequencies above DC require a time varying voltage to be applied to the coils. The coil voltage is determined by taking the time derivative of the flux linkage (Equation 6.14 or 6.22) as shown in Equation 6.23 where the last term of the RHS is added to account for the ohmic coil resistance.

$$v = \frac{d\lambda}{dt} = \frac{d\lambda}{di}\frac{di}{dt} + \frac{d\lambda}{dx}\frac{dx}{dt} + iR \tag{6.23}$$

The assumption that is now commonly made is that the flux linkage is a linear function of current, which allows the definition of the coil inductance, L, as shown in Equation 6.24. Also shown in Equation 6.24 is the coil inductance expression for the nanopositioner magnetic configuration. Note that the inductance is independent of current and displacement, although the inductive voltage, $L\frac{di}{dt}$, is not independent of current. The inductance quantifies the magnetic flux produced in the circuit for a given electric current and the inductive voltage quantifies the resistance the coil has to changing the flux in the magnetic circuit.

$$\frac{d\lambda}{di} = L = \frac{\mu_o N^2 A_p}{4g_{nom}} \tag{6.24}$$

The $\frac{d\lambda}{dx}$ term of Equation 6.23 is referred to as the speed voltage coefficient as it is the scaling factor that determines the voltage required due to mechanical motion, $\frac{dx}{dt}$. The speed voltage coefficient is given in Equation 6.25 for the nanopositioner configuration. Note the speed voltage is independent of current and dependent on position.

$$\frac{d\lambda}{dx} = \frac{\mu_o N M_o A_p A_m^2 h_m x^2}{\left(A_p h_m g_{nom} + A_m \left(g_{nom}^2 - x^2\right)\right)^2} + \frac{\mu_o N A_p A_m M_o h_m}{2\left(A_p h_m g_{nom} + A_m \left(g_{nom}^2 - x^2\right)\right)} \tag{6.25}$$

Figure 6-18 shows the variation of the inductance and speed voltage coefficient versus the number of coil turns for the nanopositioner. The two red lines for the speed voltage coefficient are the envelope in which the speed voltage coefficient actually falls. The envelope is shown to quantify the effect of variations in displacement will have on the speed voltage within the motion range of the nanopositioner.

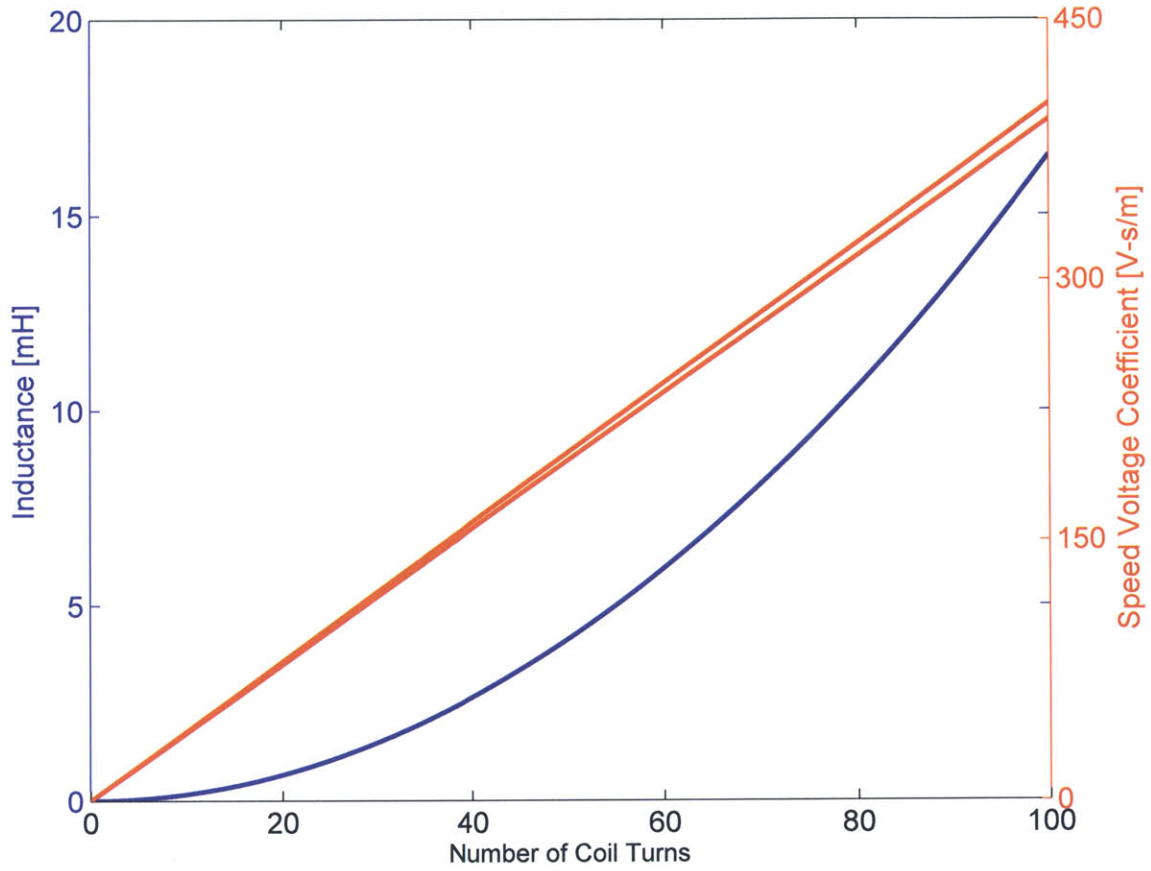

Figure 6-18: Variation of inductance and speed voltage coefficient with the number of turns.

The relations between voltage requirements, current limits, and number of coil turns have been determined and the decisions of amplifier selection and number of turns in the coil can now occur in parallel.

Several amplifiers were available and a very simplified equation was used to compare the expected nanopositioner with each of the amplifiers relative to one another. The voltage and current limits of the amplifier, along with a maximum amplitude of 25 μm, were substituted into Equation 6.23 with the assumption the maximum force and velocity were exactly in phase. The number of turns in the coil for each different amplifier configuration was found by dividing the total number of desired amp-turns by the maximum current available from the amplifier. Evaluation of Equations 6.24

and 6.25 using the Kepco BOP 50-4M specifications of ±4 A and voltage rails of ±50V led to values of 11.7 mH and 330 V s/m for an 84 turn coil, respectively.

6.4 Nanopositioner Design Details

Design details are presented for the rubber bearings, magnetics, mechanical design, and modeling. These design details include numerical values for the parameters that have been assumed constant in the previous analyzes.

6.4.1 Rubber Bearings

A factor of prime importance in selecting an actuator configuration was ensuring the rubber bearings could be easily integrated into a compact package while constraining five degrees of freedom. Figure 6-19 shows the actuator body and the placement of the rubber bearings relative to the actuator body. The actuator body is fixed to mechanical ground in the nanopositioner, but for understanding the bearing constraints, consider the outside surfaces of the bearings as being connected to ground so the actuator body would now be the moving component.

The unconstrained DOF for a general rubber pad are those motions parallel to the plane of the bearing (refer to Section 3.4). The unconstrained motions of a system with multiple rubber bearings is the common shear direction of all bearings. The common shear direction of all bearings of Figure 6-19 is x-translation and it is the DOF controlled using the magnetic actuator.

The constrained motions of the bearing pair 1-3 are θ_x, θ_z, and y-translation with reference to the coordinate system of Figure 6-19. The constrained motions of the bearing pair 2-4 are θ_x, θ_y, and z-translation. Leaving the only compliant axis as x-translation.

The total stage stiffness was determined by computing the compression, shear, torsion, and tilting stiffness of a single rubber pad and summing the stiffness contribution of the four pads of Figure 6-19 to the overall stage stiffness. Each of the rubber pads is a 25 mm square sheet of 50 Shore A Durometer neoprene with a thickness of

0.8 mm. The stiffness of Pad 1 in for all six DOF of Figure 6-19 are tabulated in Table 6.2, along with a description of the type of loading. The total stage stiffness for all six DOF is given in Table 6.3.

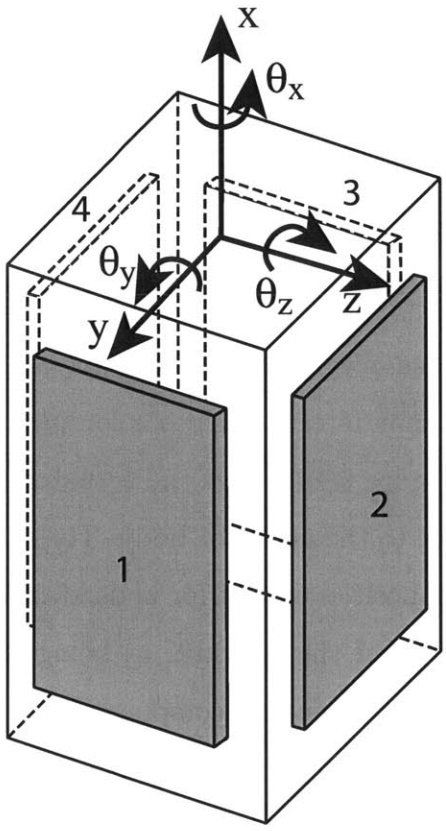

Figure 6-19: Displays the 6 DOF nanopositioner actuator and the locations of the four rubber bearings.

Table 6.2: Expected DC stiffness for rubber pad 1 shown in Figure 6-19 with the reference to the directions of Figure 6-19.

x-direction (shear)	2.4 N/μm	θ_x **(tilting)**	18640 N m/rad
y-direction (compression)	330 N/μm	θ_y **(torsion)**	260 N m/rad
z-direction (shear)	2.4 N/μm	θ_z **(tilting)**	18640 N m/rad

Table 6.3: Expected DC stiffness for each nanopositioner DOF shown in Figure 6-19.

x-direction	9.7 N/μm	θ_x	74570 N m/rad
y-direction	664 N/μm	θ_y	37805 N m/rad
z-direction	664 N/μm	θ_z	37805 N m/rad

The compression of bearings 1 and 3 provide the constraint in the y-direction, while the compression of bearings 2 and 4 provide the constraint in the y-direction. The tilting stiffness of bearings 1 and 3 provide constraint against θ_z rotation and the tilting of bearings 2 and 4 provide constraint against θ_y rotation. The tilting stiffness of all four bearings prevent θ_x rotation, leaving the only compliant motion as translation in x.

Two important assumptions in the computation of the total stage stiffness are that the rubber pad is under a uniform load and the adhesion of the pad to the supports is complete. A nonuniform loading of the will result in a reduction in bearing area actually supporting the load and the bearing stiffness will be several reduced. The stiffness reduction would be most severe due to the reduced shape factor and Section 3.2 showed the stiffness varies with the shape factor squared whereas the relation with bearing cross-sectional area is linear. Incomplete adhesion will result in a similar reduction in stiffness.

The preventative measures taken to ensure the load across the bearings were uniform and adhesion were complete include grinding of the magnetic actuator faces, hand lapping the struts, dabbing of the adhesive across the faces, and matching the four rubber pads based on uniformity and matching thicknesses.

All faces of the magnetic actuator were ground, while the struts had to be hand lapped as they where quite thin and nonmagnetic so the magnetic chuck on grinder was not useful. Adhesive was then applied by dabbing a paper towel across the adhesive until it was uniform applied, after which it was placed adhesive side down on a strut and a 5 N weight was placed on the top surface. The dabbing technique allowed visual confirmation a minimum amount of adhesive was used to eliminate the

possibility of the excess leaking out and bridging the gap between the supports.

The rubber layer was placed on the strut in a motion similar to reverse of peeling tape off a surface. One edge of the rubber pad made contact and the line of contact moved from one end of the rubber pad to the other. With the thin adhesive layer and reverse peeling technique was expected to eliminate air entrapment in the bond line to maximize the stiffness of the bond. Unfortunately this technique could not be used when applying the bearing to the other surface.

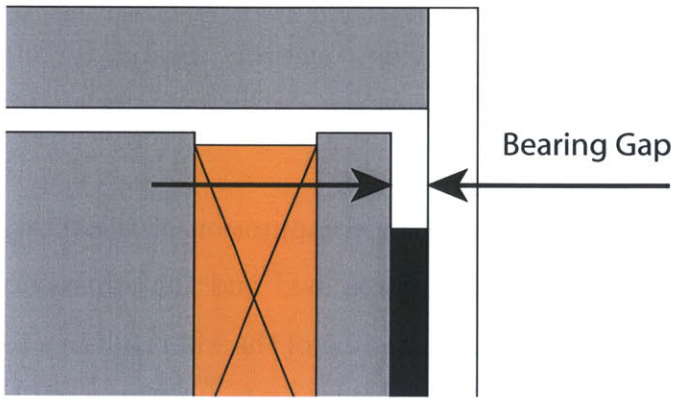

Figure 6-20: The bearing gap is defined by the actuator body width and endcap width that set up a distance constraint the bearing must meet.

Figure 6-20 demonstrates one further complication to ensuring the bearings are loaded properly. The complication is that the bearing preload is set by a distance constraint rather than a force constraint that is more deterministic. The manufacturing of the end caps, actuator body, and struts become even more critical as the rubber pads are very stiff in compression so missing any single dimension could result in losing contact between the rubber and the supports.

The rubber bearing design also provides an opportunity to greatly enhance nanopositioner power requirements at DC operation if the DC bearing stiffness is matched to the actuator negative stiffness. Matching the DC bearing stiffness to the actuator negative stiffness results in a system that has a zero current requirement at steady-state for any given position, which would be extremely beneficial for low frequency operation. The determining factor to how beneficial is dependent upon the operation

frequency and the rubber relaxation. One possible disadvantage of trying it match the negative and DC stiffness is that if the DC stiffness is underestimated the positioner may become open-loop unstable and will snap one of the magnetic gaps shut when the controller is turned off.

A result of matching the magnetic stiffness with the spring stiffness is also documented by Studer in a patent for a Spring Neutralized Magnetic Vibration Isolator [48]. This device was designed to achieve a near zero natural frequency through matching the negative magnetic stiffness with the axial stiffness of a spring. The resulting system would reject nearly all vibrational energy the low natural frequency with -2 decades/decade slope. A comparison of the expected open-loop plant model with and without stiffness matching is presented in Section 6.4.4.

6.4.2 Magnetic Design

The magnetic design started with a force target of 660 N from the actuator configuration suggested by Professor Trumper and analyzed throughout Section 6.3. The force and material specification allows calculation of the minimum pole area using the magnetic saturation magnetization of the Sandvik 1802 stainless steel and Maxwell's stress tensor. The length of the inner square pole was then calculated as one-half the total pole area.

Knowing the pole area allows the permanent magnet to then be sized based on the discussion in Section 6.3.1 on over-biasing. The coil window area is determined by observing a current density limit of $J = 5 \text{ x } 10^6$ A/m^2 in the copper that is determined by thermal considerations and the total necessary amp-turns to saturate the actuator pole faces. The outer pole octagonal shape was determined by the coil size, inner pole dimension, and the need to provide the connection to mechanical ground whereas the dimensions were determined by matching the inner pole area with the outer pole area.

The last dimension based on magnetic considerations was the end cap thickness. The minimum thickness is determined by ensuring magnetic saturation would not choke off flux through the circuit. Maximum flux through a single end cap occurs when the pole faces on that end cap are saturated. It was assumed the maximum

flux density in the end would occur just as flux started leaving the end cap into the inner pole face. This results in a surface of area $4Lt_e$ that should be at magnetic saturation when the maximum flux is in the circuit where L is the length of the inner pole. Setting this area equal to the area of the inner or outer pole, which should also be at saturation for maximum flux, results in Equation 6.26.

$$t_e = \frac{A_p}{4L} \tag{6.26}$$

Substitution of the coil current as $i = Ni/N$ and the definition for coil resistance from the geometry of the wire leads to the RHS of Equation 6.27 where L_{ave} is the average length of each coil turn, A_{wire} is the cross-sectional area of a single wire, and ρ_{cu} is copper resistivity.

$$P_{heat} = i^2 R_{coil} = \frac{(Ni)^2}{N^2} \frac{N L_{ave} \rho_{cu}}{A_{wire}} \tag{6.27}$$

The cross-sectional wire area can be eliminated with the substitution $A_{wire} = PF\ A_{window}/N$ where PF is the wire packing factor. Substitution of the average coil length for the nanopositioner geometry leads to Equation 6.28, where every term has previously been determined so the heat dissipation depends on force capacity (read amp-turns).

$$P_{heat} = \frac{(Ni)^2 \rho_{cu} \left(4L_2 + 2\pi h_m/\sqrt{2}\right)}{PF\ h_m^2 R_{window}} \tag{6.28}$$

Table 6.4 lists many important magnetic circuit parameters of the nanopositioner that was built and tested in this work. A few notes on values in Table 6.4 are presented here:

- The permanent magnet area given is the combined area of the four magnets used in construction.
- The number of coil turns was increased from 80 to 84 to accommodate coil construction.

- The packing factor is the actual attained packing factor and does not take account of the space left for the coil in the mechanical package.

Table 6.4: Nanopositioner magnetic circuit parameters.

Nominal Air Gap, g_{nom}	100 μm
Pole Face Area, $2A_p$	1052 mm^2
End Cap Thickness, t_e	5.75 mm
PM Area, A_m	168.8 mm^2
PM Magnetization Density, M_o	9.42 x 10^6 A/m
PM Length, h_m	4.0 mm
Total Coil Turns, N	84
Actual Packing Factor, PF	0.81
Current Density, J	3.5 x 10^6 A/m^2
Heat Dissipation @ 4 A, P_{heat}	1.89 W
Motor Constant, K_m	497 N/$\sqrt{\text{W}}$
Force Constant, K_f	330 N/A
Magnetic Stiffness, K_{mag}	9.32 x 10^6 N/m

6.4.3 Mechanical Design

Only one structural vibration mode was considered during the development of the nanopositioner as all other components had low length to thickness ratios that tend to push structural vibrations to frequencies far above the 5 kHz limit of this work. The one mode will be directly excited by the magnetic actuator will be the rigid body motion of each end cap supported by the spring formed by the four struts clamped to the rubber pads. The mass of each end cap and associated machine screws is 72 g.

The effective spring length of the struts was already set by the magnetics design at 37.7 mm and the material was already determined to be 304 stainless steel with a modulus of elasticity around 200 GPa. The 304 stainless steel was chosen as it is nonmagnetic and also to minimize galvanic corrosion with the Sandvik 1802. The width of each strut, w, was determined by the size of the rubber pads in 6.4.1 to be 25.4 mm wide so the last variable that needed to be defined is the strut thickness,

t. Substituting the axial stiffness of the struts into the standard equation for natural frequency and solving for strut thickness results in Equation 6.29

$$t = (\pi f)^2 \frac{mL}{wE} \tag{6.29}$$

Substitution of known values in Equation 6.29 and a minimum desired resonant frequency of 10 kHz gives a minimum thickness of 0.52 mm, which is would be too thin to give an acceptable preload to the rubber bearings. The preload complication and availability led to the strut thickness being upgraded to 3.05 mm. This strut thickness moves the structural vibration frequency in question to 25 kHz and provides a strut aspect ratio high enough the flexible membrane modes would not be an issue.

Table 6.5: Nanopositioner magnetic circuit parameters.

Length (controlled direction)	42 mm
Max. Cross-section Width	48 mm
Footprint	1200 mm^2
Stage Mass	257 g

6.4.4 Modeling Nanopositioner

The actuator characteristics and bearing geometry have been developed in-depth enough a qualitatively useful model of the nanopositioner can now be presented. Two important aspects that are missing from making this model quantitatively useful is an accurate model for the rubbers dynamic properties and the hysteresis loop for the Sandvik 1802. However, these limitations can be quickly overcome in future projects and the full nanopositioner model presented here will be of greater utility.

The high degree of linearity demonstrated for the current actuator geometry in Section 6.3.1 allows the motor force constant and linearized magnetic stiffness, Equations 6.9 and 6.7, in deriving a linear transfer function model from input current to stage position, $X(s)/I(s)$, with little loss of accuracy for small signals. The accuracy for large signals is significantly degrade due to the nonlinear material hysteresis that

is apparent for large signals and is demonstrated in Section 7.2.2.

A schematic realization of the nanopositioner is shown in Figure 6-21 with the corresponding model shown in Figure 6-22. The mass, m, of the model represents all moving parts of the nanopositioner that includes both end caps and the four struts that are suspended around the actuator body on the black rubber bearing. The actuator force is shown in the model as F and is independent of position as the linearized magnetic stiffness element is modeled as a negative mechanical spring in parallel with the rubber bearing DC stiffness..

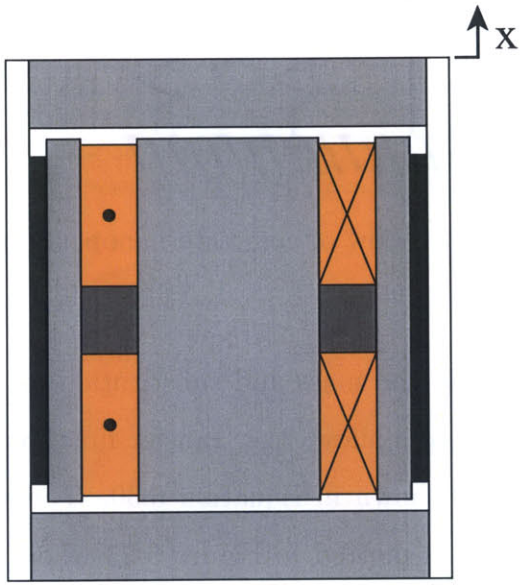

Figure 6-21: Integration of the rubber bearings with the electromagnetics of the nanopositioner.

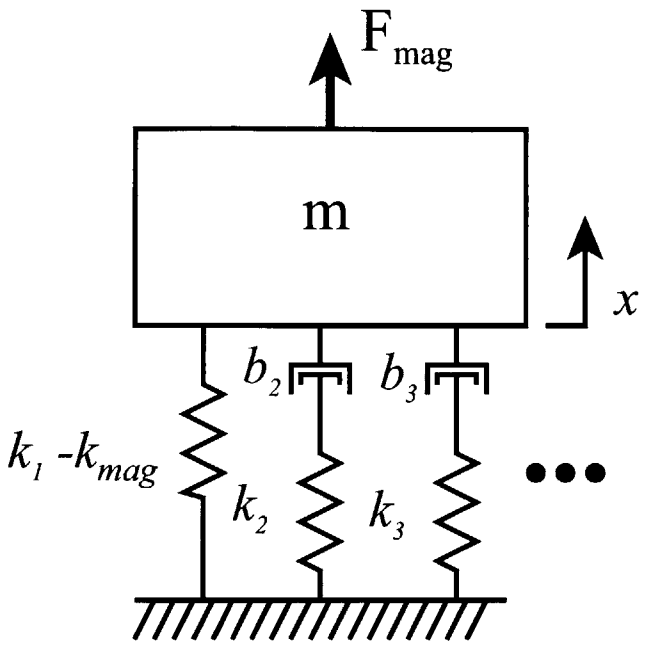

Figure 6-22: View of complete nanopositioner.

Summation of all forces on the mass and substitution of $F_{mag} = k_f i$ while considering two spring/damper pairs allows the transfer function from current to stage position to be derived and is shown in Equation 6.30. The expected open-loop response of the nanopositioner is plotted in Figure 6-23 where *a priori* knowledge of the open-loop response of the constructed nanopositioner was used to find reasonable values for k_1, k_2, k_3, b_2, and b_3.

$$\frac{X(s)}{I(s)} = \frac{k_f(b_2 s + k_2)(b_3 s + k_3)}{mb_2b_3s^4 + m(b_2k_3 + b_3k_2)s^3 + (b_2b_3(k_1 - k_{mag} + k_2 + k_3) + mk_2k_3)s^2 + (b_3(k_1k_2 + k_2k_3) + b_2(k_1k_3 + k_2k_3) - k_{mag}(b_2k_3 + b_3k_2))s + k_2k_3(k_1 - k_{mag})} \quad (6.30)$$

Figure 6-24 demonstrates the expected open-loop frequency response when the negative spring stiffness is matched to the DC stiffness of the rubber bearings.

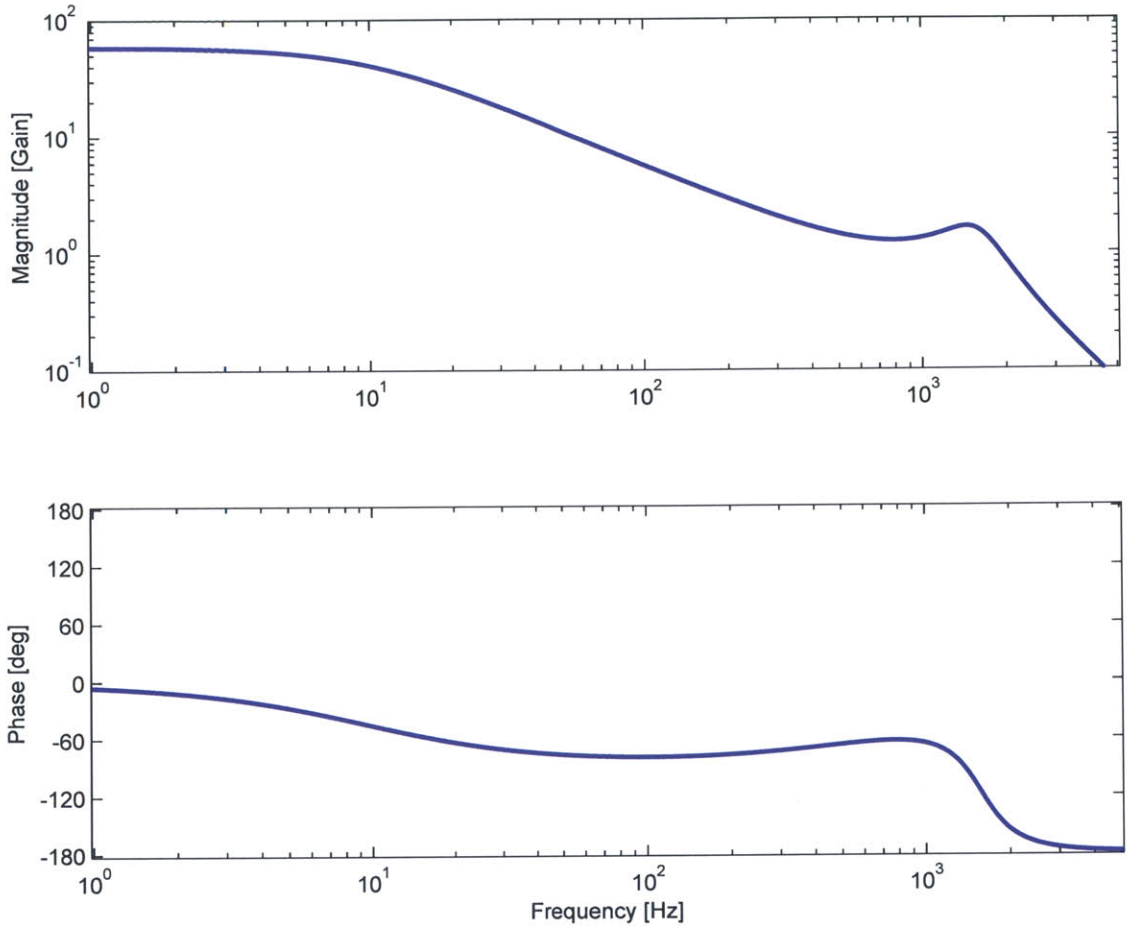

Figure 6-23: Expected nanopositioner frequency response where stage position is measured in μm and current in amps.

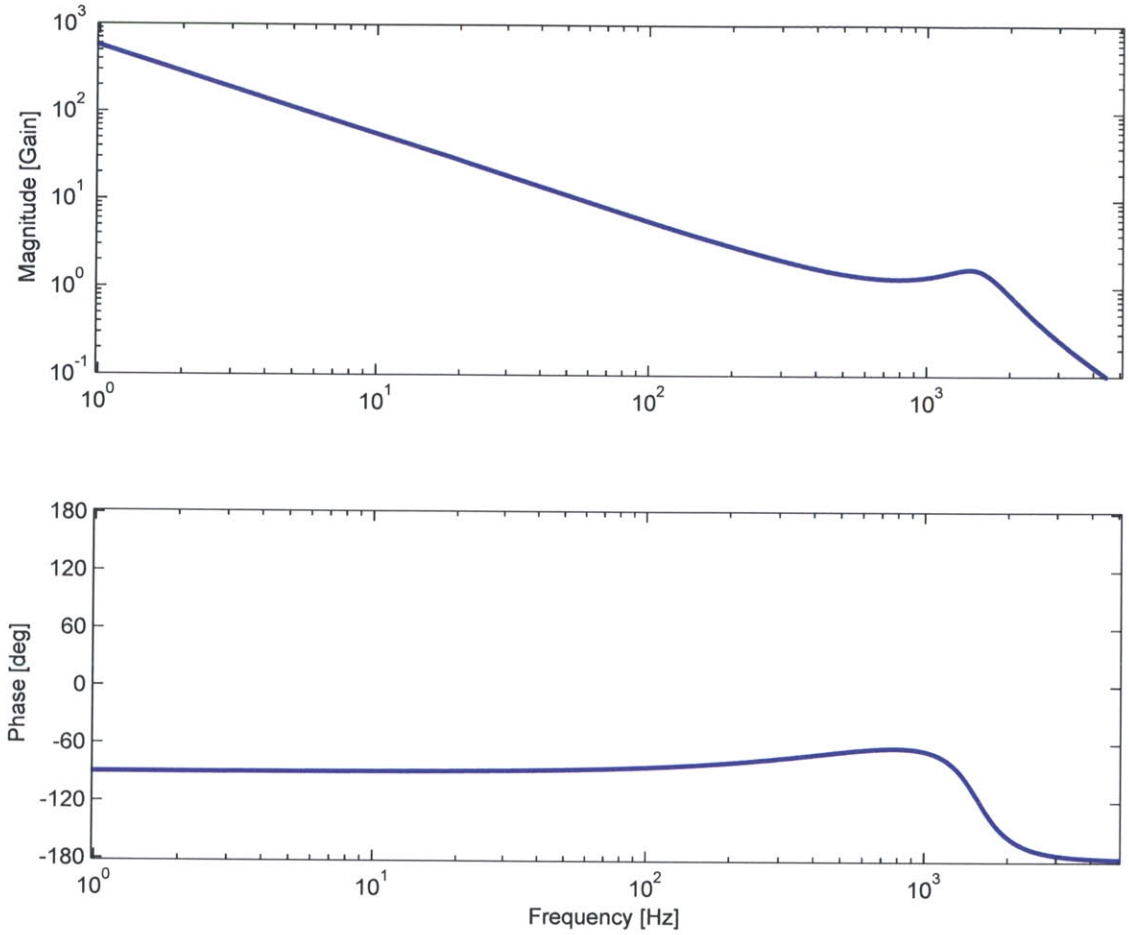

Figure 6-24: Expected response of a nanopositioner with the DC rubber stiffness matched to the negative spring stiffness.

6.5 General Nanopositioner Concepts

This section reviews concepts and ideas that could be incorporated into the class of nanopositioner developed in this thesis. Included here are integrated sensing concepts, alternative guidance systems, and higher DOF positioning systems.

A concept for integrating a capacitance distance sensor is shown in Figure 6-25. This particular capacitance distance sensor would have a very large sensing area and the nanopositioner could be plug and play with very little setup as all components would be internal.

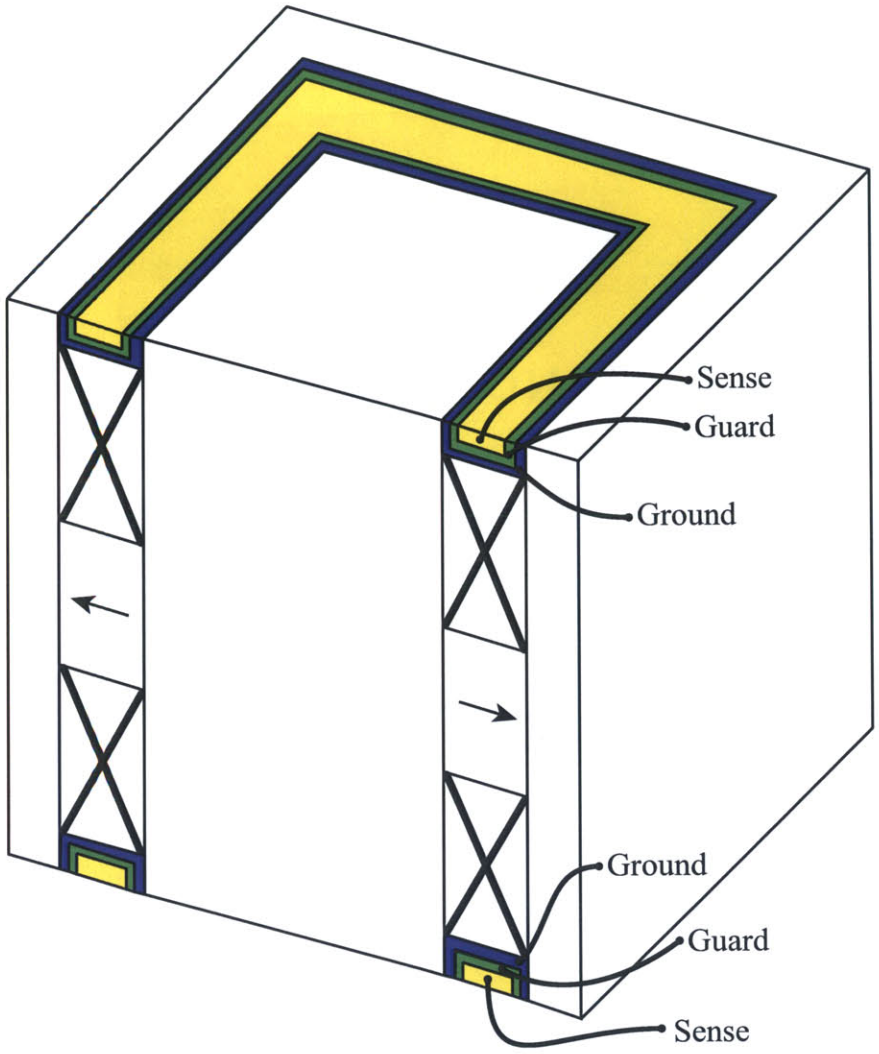

Figure 6-25: Nanopositioner with integral capacitance sensing.

Metal flexures are the traditional method for eliminating the stiction, friction, and vibration caused by conventional sliding or rolling contact bearings. Although the benefits of replacing metal flexures with rubber bearings is one of the core ideas of this work, rubber bearings are not well suited to all situations. Several situations where metal flexures are better suited as a positioning system include elevated or ultra-low temperatures and rubber unfriendly environments (e.g. ozone, high oxygen environments, and strong oxidizers). Figure 6-26 shows how metal flexures could be used as the guidance system for the current nanopositioner with very little modification.

Figure 6-27 demonstrates how metal flexures guide motion.

Figure 6-26: Nanopositioner concept employing metal flexures in place of the rubber bearing.

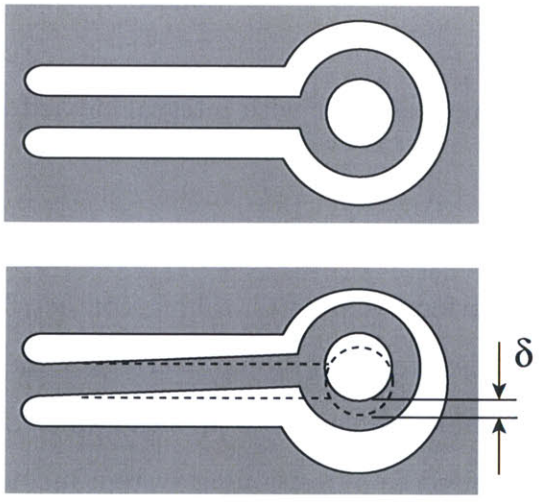

Figure 6-27: Metal flexures with a deflection of δ.

Another sensor concept that could be employed on the nanopositioner is glass scales encoders. Two glass scales could be integrated into the current prototype on opposite sides to measure the position differential from one side of the positioner to the other, in addition to the current capacitance distance sensor. Such a configuration could be used to evaluate the stage stiffness and detect parasitic motions.

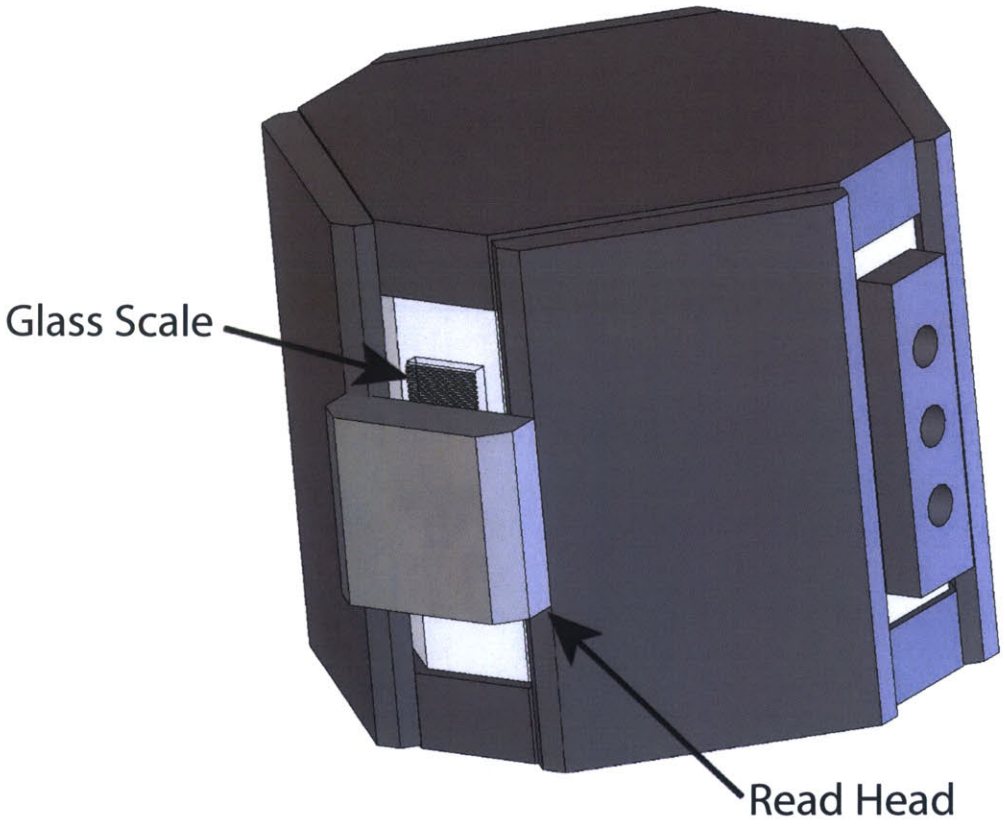

Figure 6-28: Nanopositioner with glass scale for measuring displacement.

Figure 6-29 presents a two DOF magnetic nanopositioner with the stage suspended on a rubber sheet. Figure 6-29 presents the x-plane cross-section of the nanopositioner, although the y-plane cross-section is identical. Actuator nonlinearities would be higher as the force would be dependent on both the x and y stage positions. A second drawback is the torsional stage stiffness would be close to the translational stiffness meaning torsion is unconstrained. Figure 6-30 increases the translational to torsional stiffness ratio by introducing a void near the center of the stage. The

advantage of this configuration is that the torsional stiffness can now be designed independent of translational stiffness.

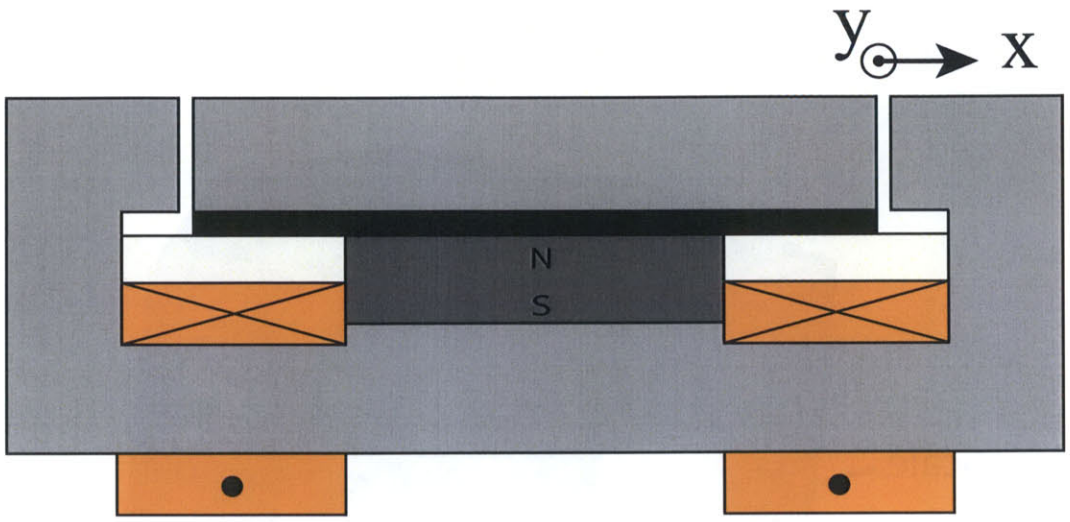

Figure 6-29: Cross-sectional view of a 2-axis nanopositioner configuration.

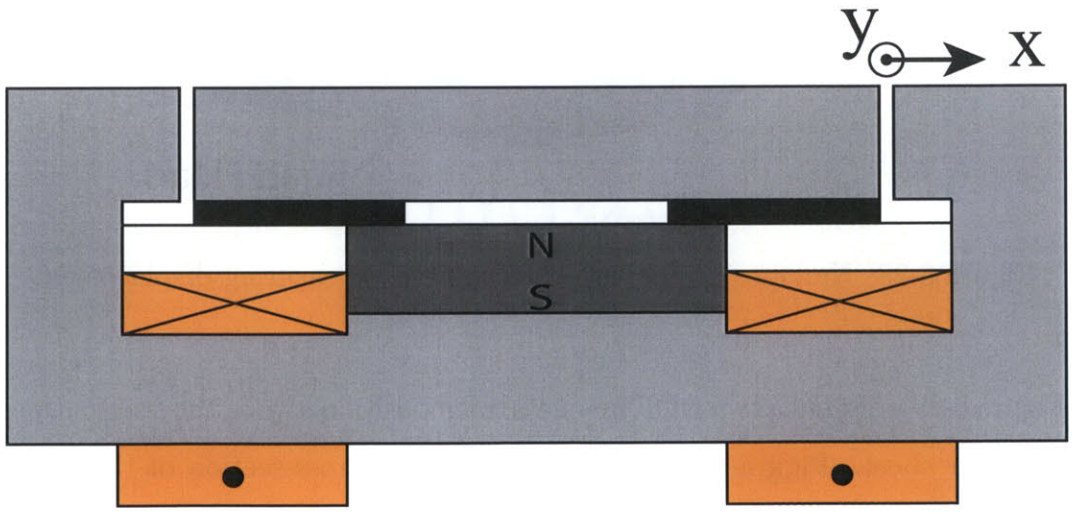

Figure 6-30: XY stage with higher torsional to lateral stiffness ratio.

An ideal configuration for active vibration cancellation is shown in Figure 6-31. The configuration is torsionally compliant and the bearing is composed of a stack of o-

rings. The configuration would however require the development of design guidelines for determining the stiffness of the o-ring stack with bulging interference (as discussed in Section 6.1.1).

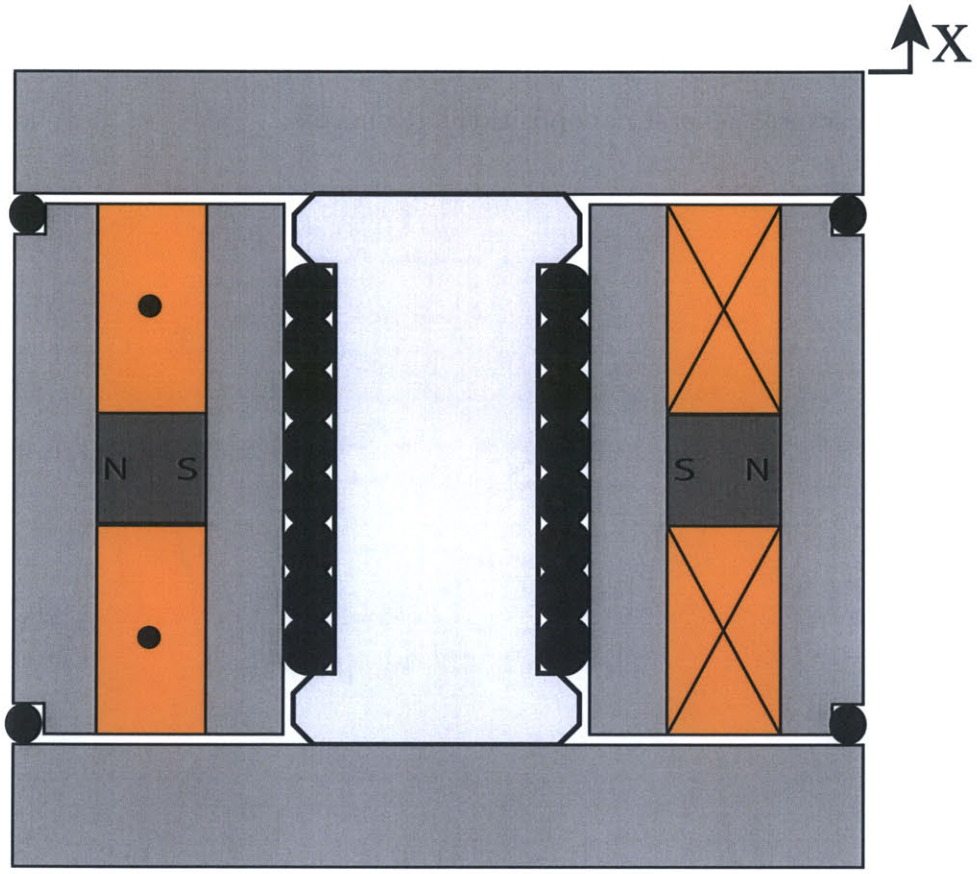

Figure 6-31: Cylindrical nanopositioner configuration for applications not requiring rotational stiffness.

6.6 Summary

An initial bearing concept that utilized a stack of o-ring was analyzed to determine if the concept could be employed in nanopositioning applications. The result of the analysis is that only o-ring stacks with bulging interference can provide suitable stiffness for nanopositioning applications. Several hard-linearized, normal-stress actuator configurations were presented and were followed by a detailed magnetic analysis of

the selected actuator configuration. The primary results of the magnetic analysis are the magnetic force as a function of current and displacement, as well as the equations for speed voltage and actuator inductance.

Nanopositioner design details were presented including bearing details and the theoretical positioner stiffness in all six DOF, positioner magnetic circuit parameters, nanopositioner package size, and nanopositioner modeling details. The chapter concluded with several general nanopositioning concepts.

Chapter 7

Nanopositioner Setup and Control

This chapter presents the hardware necessary for running the nanopositioner and the final system performance. Other issues addressed include complications encountered in using laser interferometer position feedback, the addition of a capacitance distance sensor for position feedback, and the controller design that gave the final system bandwidth of 580 Hz and a maximum static force of 460 N.

7.1 System Physical Layout

The equipment initially available for testing the nanopositioner was a Kepco BOP 50-4M linear current amplifier, Tektronik AM502 Differential Amplifier, an experimental air-cooled laser interferometry source, a Zygo ZMI 4004 measurement board, a dSPACE DS1103 PPC Controller running at 40 kHz, and a custom interface for accessing 40-bit position data, 32-bit velocity data, and 32-bit time data for use in control by DS1103 board.

The laser source and necessary optics had been previously used for measuring horizontal displacements so the nanopositioner was positioned horizontally and an interferometry mirror was epoxied to one face of the stage as shown in Figure 7-1. The laser source and optics were previously positioned such that the laser was 120 mm above the table while the center point of the mirror was 45 mm above the table. The arrangement shown in Figure 7-2 was devised to raise the nanopositioner

to the proper level. A close inspection of Figure 7-1 reveals the two locations where the laser reflects off the mirror.

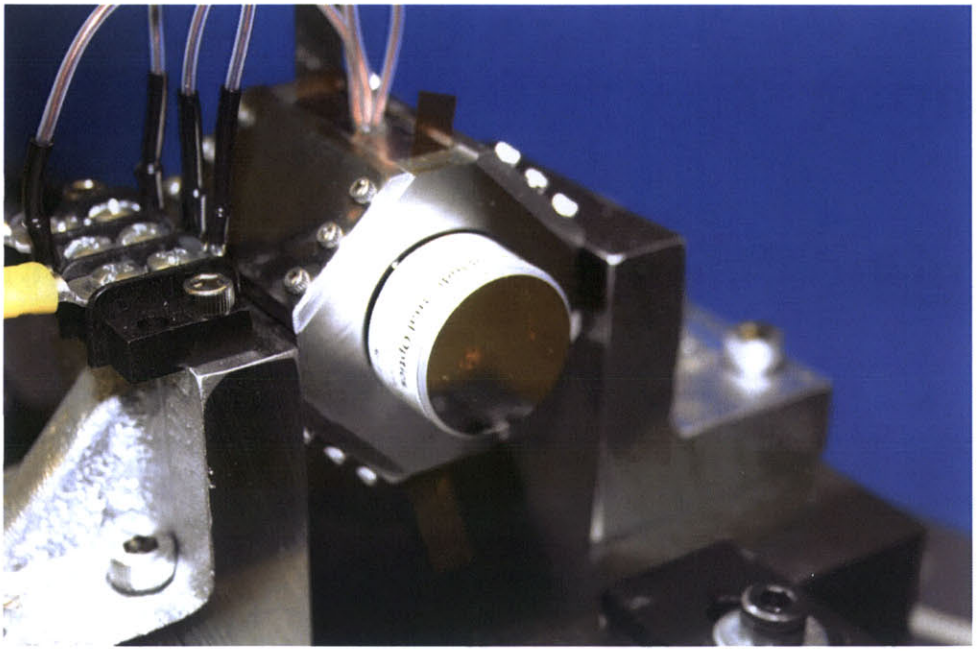

Figure 7-1: Photo of the interferometry mirror attached to the positioner with the gap shims still in place.

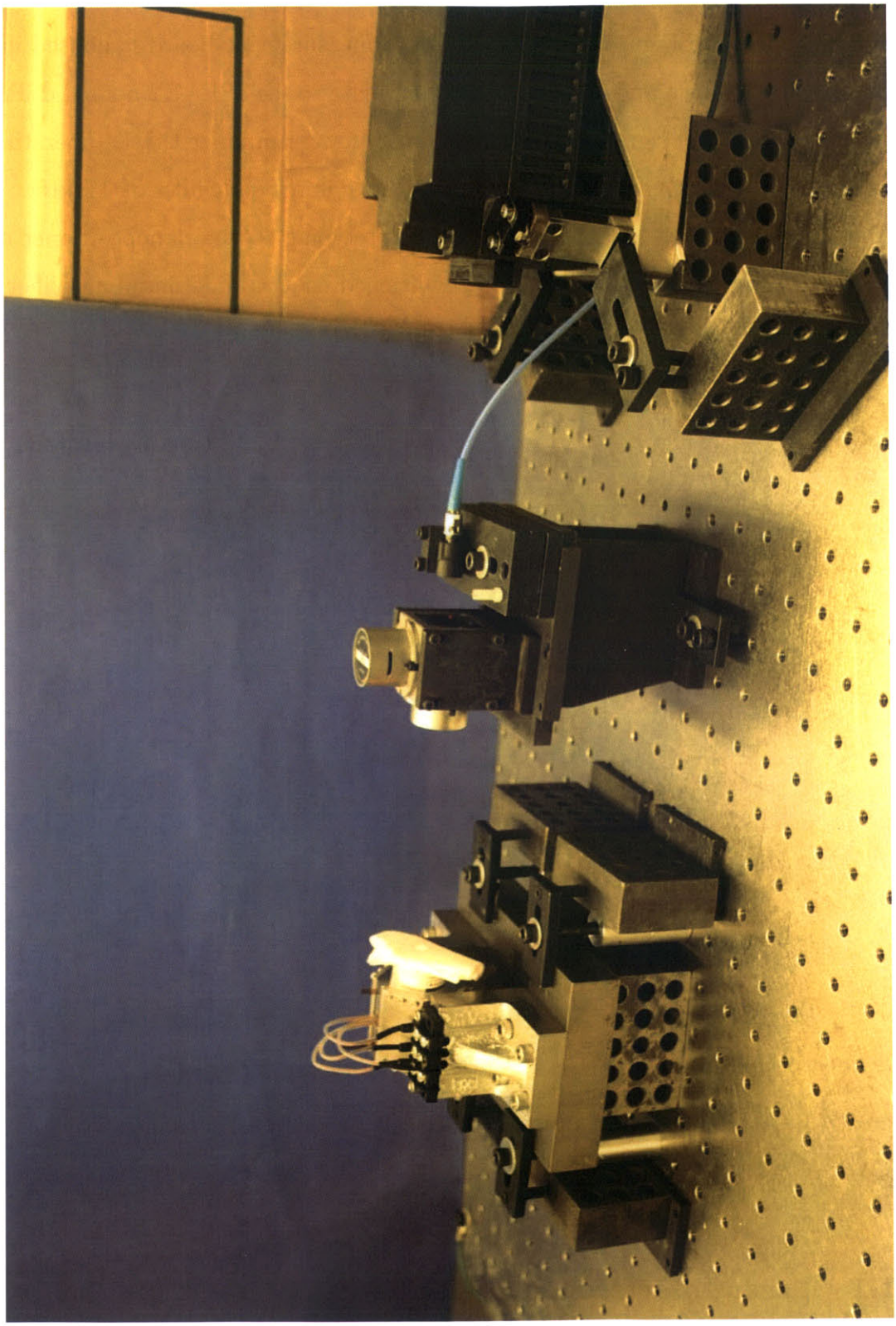

Figure 7-2: Nanopositioner, laser interferometry source and optics arrangement on the optical table.

The components needed to run the nanopositioner that are not on the laser table are shown in Figure Figure 7-3. A single Zygo measurement board is housed in the computer tower shown and passes displacement data to the dSPACE board. dSPACE computes the control signal and sends it to the power amplifier that is operating in current mode with a gain of 0.4 A/V to a maximum bandwidth of 11 kHz. The current passes through a resistor of 0.1 Ω before going to the nanopositioner coils. The voltage drop across the resistor is conditioned using a differential amplifier and is passed to dSPACE through one of the 16-bit A/D channels.

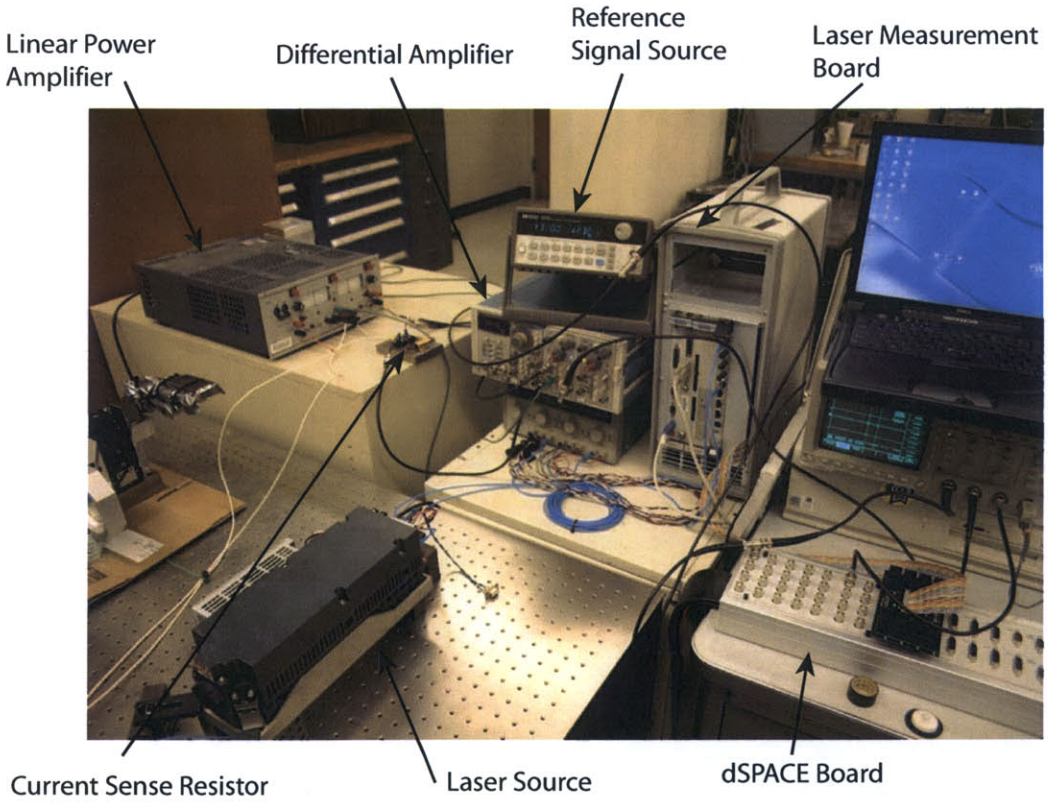

Figure 7-3: Arrangement of equipment needed to operate the nanopositioner with laser feedback.

7.1.1 Laser Interferometry Feedback

The laser source, optics, and measurement board constitute a Displacement Measuring Interferometer (DMI) used to acquire high resolution real-time position, velocity,

and time. The resolution capability of the two pass configuration of this system is 0.15 nm and the bandwidth is limited to a minimum of 15 kHz by settings on the measurement board[1] [11].

The laser interferometer based data is available through a S-function in Simulink and can be accessed by controls running on the dSPACE hardware. The interface consists of several printed circuit boards and drivers developed by David Otten in the Precision Motion Control Laboratory at MIT.

The displacement data passed to dSPACE through the interface has the units of nanometers already associated with it so the block diagram of the system varies slightly from the usual form as shown in Figure 7-4. The error that drives the system is not found by comparing a reference voltage to a electrical representation of the current position. Instead the reference voltage is converted to a desired position from which the current position is subtracted before being converted back into a voltage for use by the compensator. The block diagram could be simplified to eliminate the displacement subtraction however Figure 7-4 shows how the control was performed in Simulink.

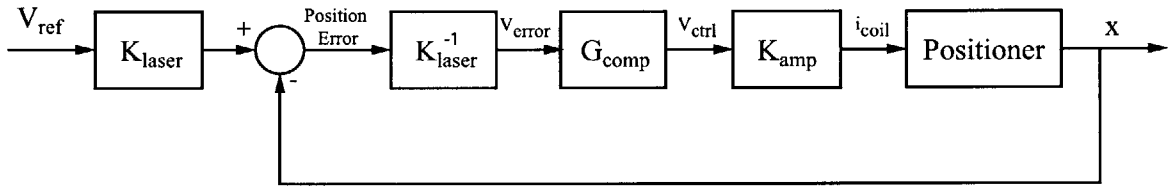

Figure 7-4: Block diagram of compensated nanopositioner system with laser position feedback.

The open-loop system frequency response had to be obtained using the HP 35665A DSA before G_{comp} of Figure 7-4 could be computed. The DSA requires two voltage signals so the Zygo board displacement was multiplied by a gain $K_{out} = 0.7$ V/μm and output to the DSA through a D/A channel as shown in Figure 7-5.

[1]The measurement board bandwidth setting was not checked due to time constraints and the fact the minimum bandwidth was sufficient for the nanopositioner

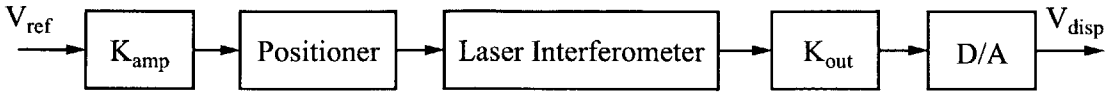

Figure 7-5: Open-loop configuration required to obtain a voltage representation of displacement for use with the DSA.

A major problem was soon discovered during a high resolution frequency sweep and can be seen Figure 7-6 between 500 and 600 Hz. The laser source has dynamics of its own at these frequencies and goes unstable preventing the completion of the sweep. The sweep in Figure 7-6 was obtained using a low source amplitude and took several attempts to complete successfully. Luckily an alternative sensor was available in the form of a capacitance position sensor and was easily integrated into the test configuration.

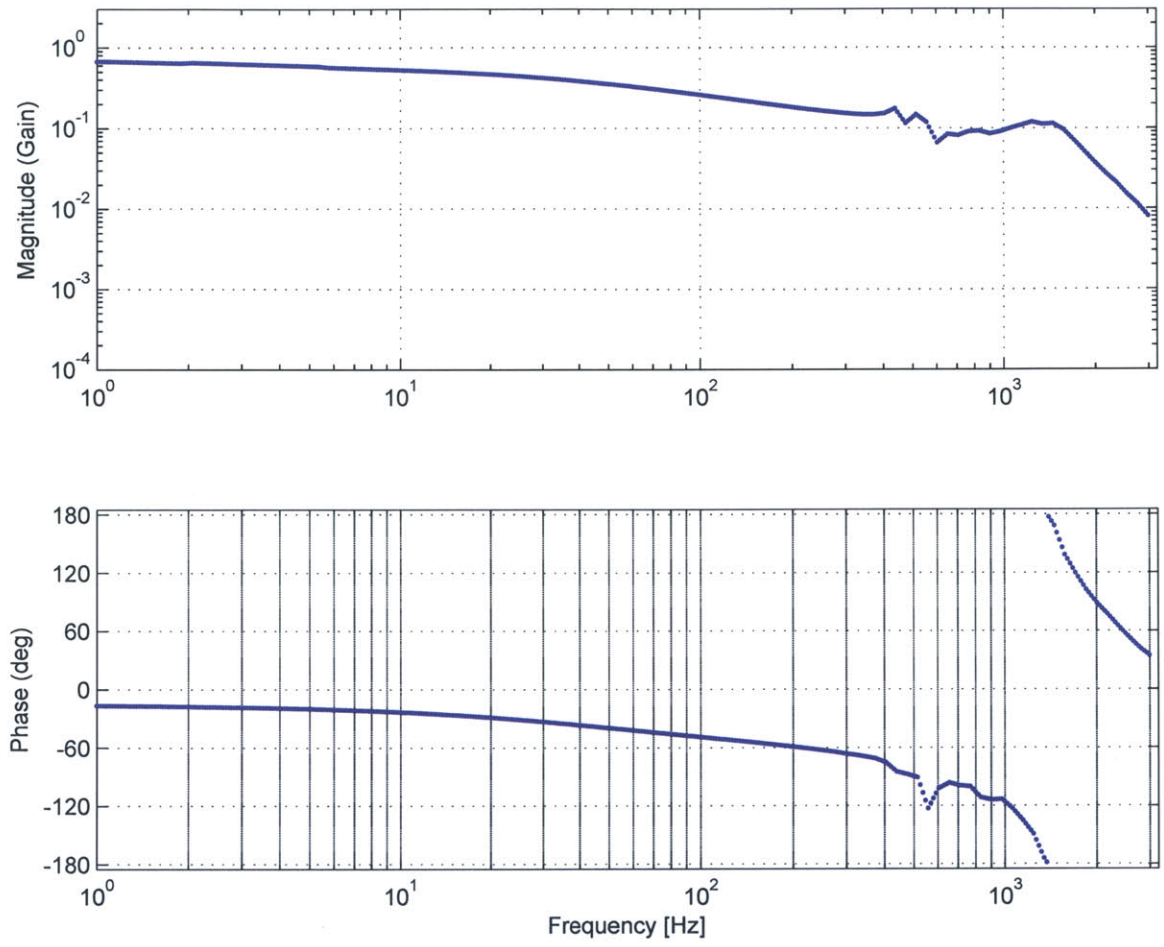

Figure 7-6: The open-loop magnitude and phase of the nanopositioner with laser interferometer feedback are plotted.

7.1.2 Capacitance Position Sensor Feedback

The replacement of the laser interferometer with capacitance distance sensor feedback was unfortunate as the bandwidth and resolution were reduced from more than 15 kHz and 0.15 nm to 5 kHz and 1.5 nm, respectively. However the new capacitance distance sensor performance did not degrade the results in this work as the sensor bandwidth was more than five times the system bandwidth and the system noise floor was not

investigated.

Mounting the capacitance gage to the nanopositioner required grounding the positioning stage that was serving as the capacitance target and adding a plate parallel to the stage ends to hold the capacitance distance sensor normal to the stage ends. The plate, capacitance probe, and one crimp-on connection for the grounding wire are shown in Figure 7-7. The two brass-tipped set screws are visible in the top face of the plate. The set screws were gently tightened as distortion of the capacitance sensor housing can affect the linearity and scaling factor [50].

The capacitance distance sensor had an electronics module that required jumper setting changes for the capacitance sensor to operate over the entire 100 μm of travel. The electronics module required the use of a differential amplifier before the position data could be passed to dSPACE through a 16-bit A/D.

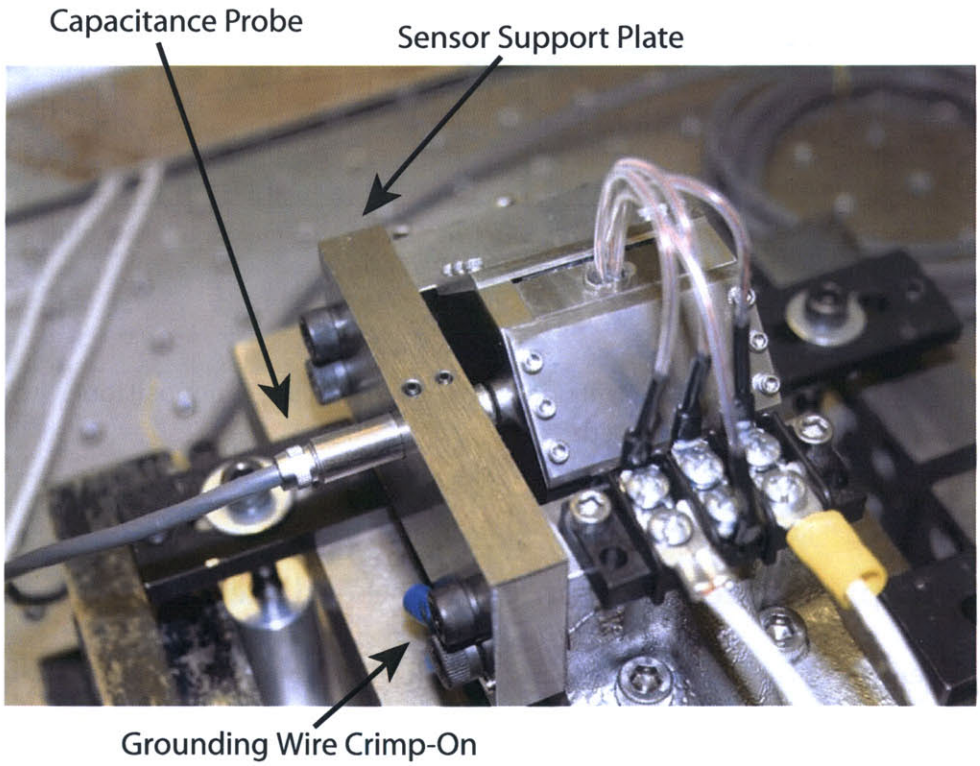

Figure 7-7: View of capacitance position sensor after installation on the nanopositioner.

Use of the capacitance distance sensor changed the closed loop system block diagram from that shown in Figure 7-4 to the more traditional block diagram of Figure 7-8. The dotted box in Figure 7-8 represents the elements that were implemented in the digital controller.

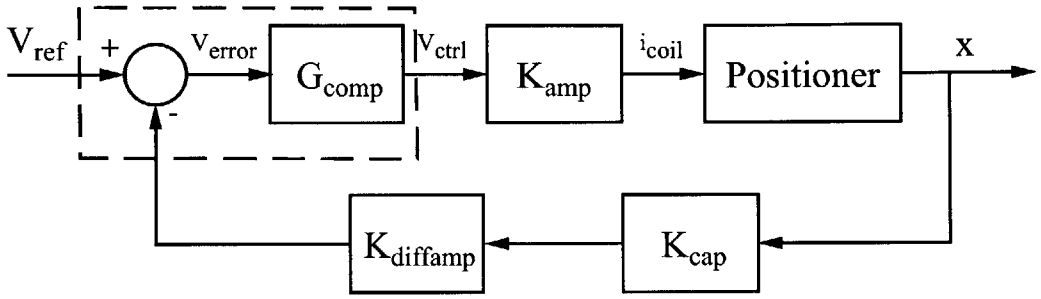

Figure 7-8: Block diagram of compensated nanopositioner system with capacitance sensor position feedback.

The input-output response of the nanopositioner itself is demonstrated in the open-loop step response of Figure 7-9. The step in coil current provides a constant force to the stage and the resulting position response can be predicted by the Multiple Standard Element viscoelastic model presented in 3.6. The quick initial response is due to each of the spring elements extending and supporting some fraction of the force applied by the actuator. The stage velocity decreases as the stage approaches the steady-state position found by the parallel combination of all the springs. The decreased velocity reduces the force each series combination of springs and dampers can support, resulting in an increased load and extension of the first spring, K_1.

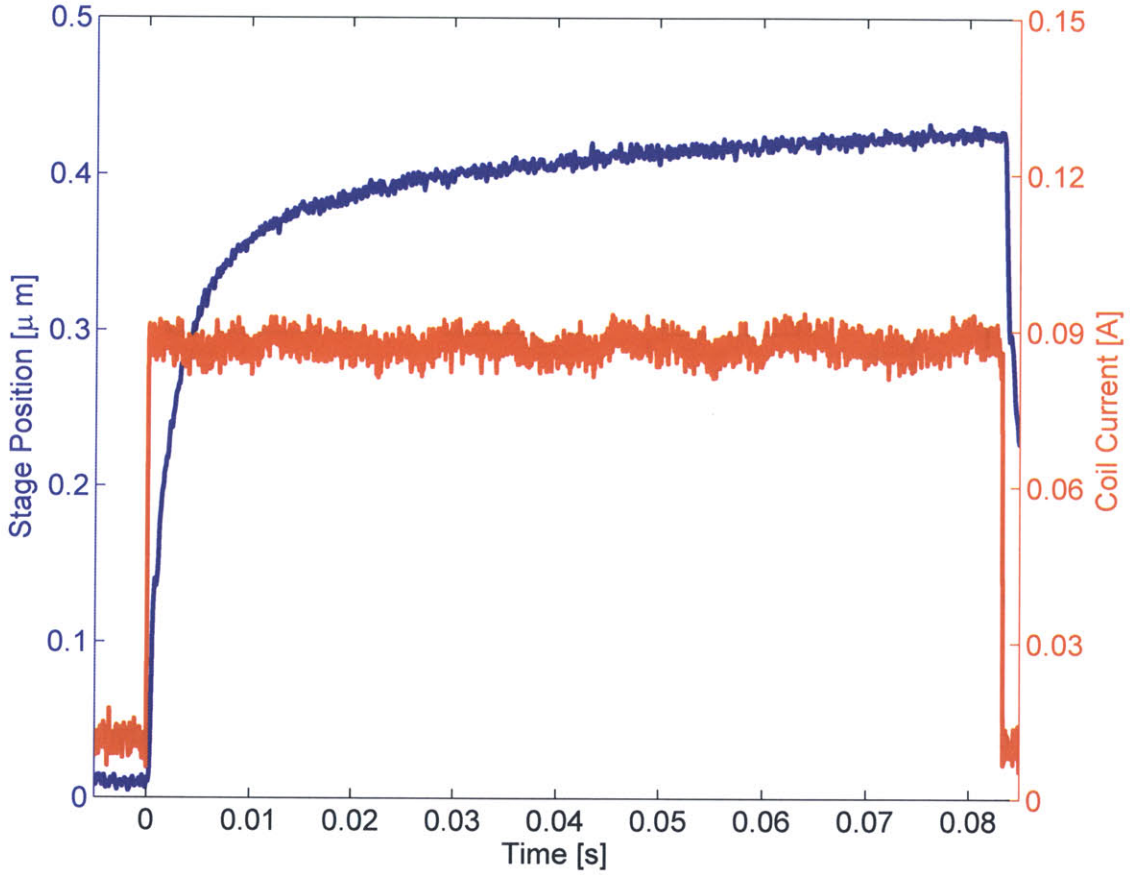

Figure 7-9: The coil current and stage position are shown for a open-loop coil current step of 70 mA.

Figure 7-10 compares the open-loop frequency response of the nanopositioner when capacitance sensor and laser interferometer feedback are used. Several extra system modes can be identified around 500 Hz when laser interferometer feedback is used. This evidence suggests a mechanical resonance of the laser cavity that would change the laser beam frequency slightly and this change would register with the interferometer measurement board as motion. The only significant deviation of the capacitance sensor open-loop response from the expected open-loop response is the resonance around 3 kHz although it is far enough away from probable crossover points it irrelevant. The lowest expected structural vibration mode was at 25 kHz as discussed in Section 6.4.3, although the contact stiffness between the end caps and struts were

neglected.

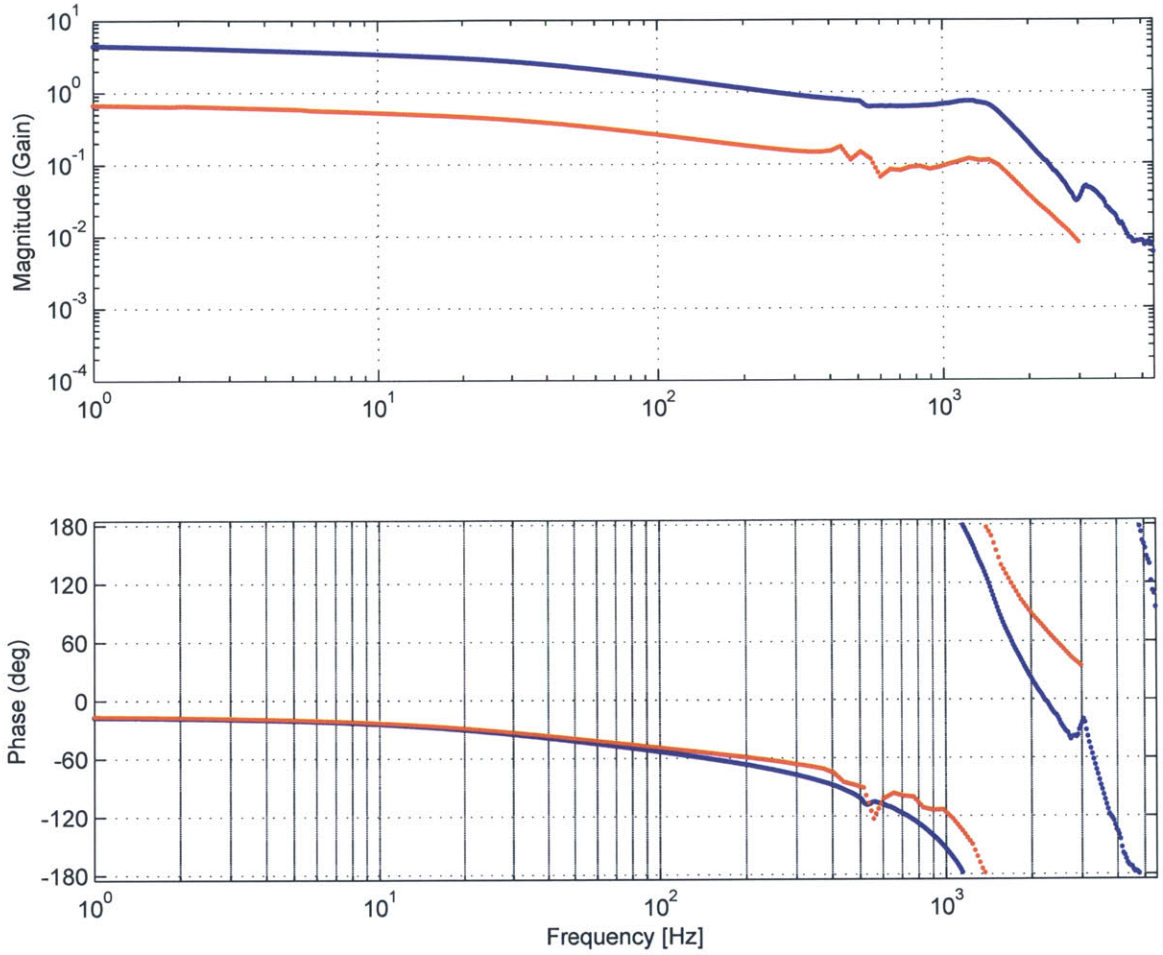

Figure 7-10: Comparison of the open-loop plant responses for capacitance sensor (blue) and laser interferometer (red) feedback.

7.2 Closed-loop Control

The purpose of this work is to establish the electromagnetically actuated nanopositioner as low-cost alternative to piezoelectric devices, and as such, a relatively simple compensator was utilized. The goal was to push the positioner to moderate bandwidth while maintaining zero steady-state error. The simplest control structure that

could be used to reach this goal is a lag-lead compensator. However, a slight resonance in the nanopositioner at 1.2 kHz made an integral compensator in place of the lag more desirable as discussed later in this section.

The standard form for implementing an integral-lead controller is shown in Equation 7.1. It is the form obtained by cascading an integral compensator with a lead compensator.

$$G_c(s) = \frac{K \ (\tau s + 1)}{T_i s \ (\alpha \tau s + 1)} \tag{7.1}$$

The cascaded form is convenient for quick implementation, but has the disadvantage that adding anti-windup limits adversely affect the lead compensator as well as limiting the integrator windup. Equation 7.1 can be factored into a parallel form where the integrator anti-windup limits can be effectively implemented without affecting the lead compensation. The parallel form is shown in Equation 7.2 where the first term is the integrator.

$$G_c(s) = \frac{K}{T_i s} + \frac{K\tau\,(1-\alpha)}{T_i\,(\alpha\tau s + 1)} \tag{7.2}$$

A block diagram of how each of these forms is implemented in Simulink is shown in Figure 7-11 where the integrator control effort is explicitly available for saturation limits to be implemented. Limiting the effect of the saturation limits is important to preserve the full dynamic performance independent of DC loads such as the weight of an object when the nanopositioner is positioned vertically.

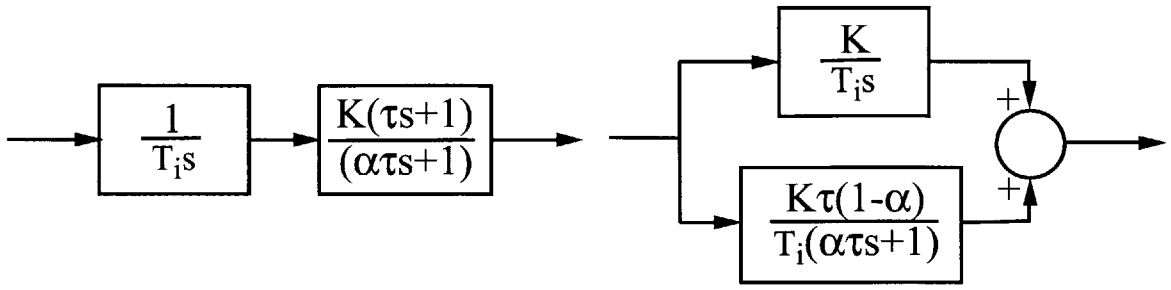

Figure 7-11: Block diagram of the series and parallel forms of integral-lead compensator for control of the nanopositioner.

7.2.1 Aggressive Control

The goal of the first controller designed was to determine a probable upper limit on bandwidth with little regard to the desirability of the step response. The integral time was arbitrarily set to 1 millisecond. Placing the lead compensator was difficult as it was desirable to attenuate the plant resonance near 1200 Hz while maximizing the phase margin. The lead compensator that was found to provide an acceptable compromise between resonance attenuation and phase addition is shown in Equation 7.3 in both the continuous time and discrete time equivalent found using Tustin's method. The effect of the digital control running at 40 kHz is a decrease in phase of less than 1° at 200 Hz and 4.5° at 1 kHz, which justifies designing in the continuous domain. The parameters that describe this controller in terms of the variables defined in Equation 7.1 are $\tau = 1.7857$ x 10^{-3}, $\alpha = 0.08$, $T_i = 0.001$, and $K = 0.8074$.

$$G_c(s) = \frac{10092.5(s+560)}{s(s+7000)} = \frac{0.0921(z-0.9861)(z+1)}{(z-1)(z-0.8391)} \tag{7.3}$$

The open-loop plant with the aggressive compensation of Equation 7.3 is shown in Figure 7-12 with the closed loop response shown in Figure 7-13. The compensation pushes the crossover frequency to 500 Hz resulting in a closed loop bandwidth of 1.2 kHz. Note the gain margin is extremely low at only 1.25 and the phase margin is 44° resulting in a very oscillatory step response .

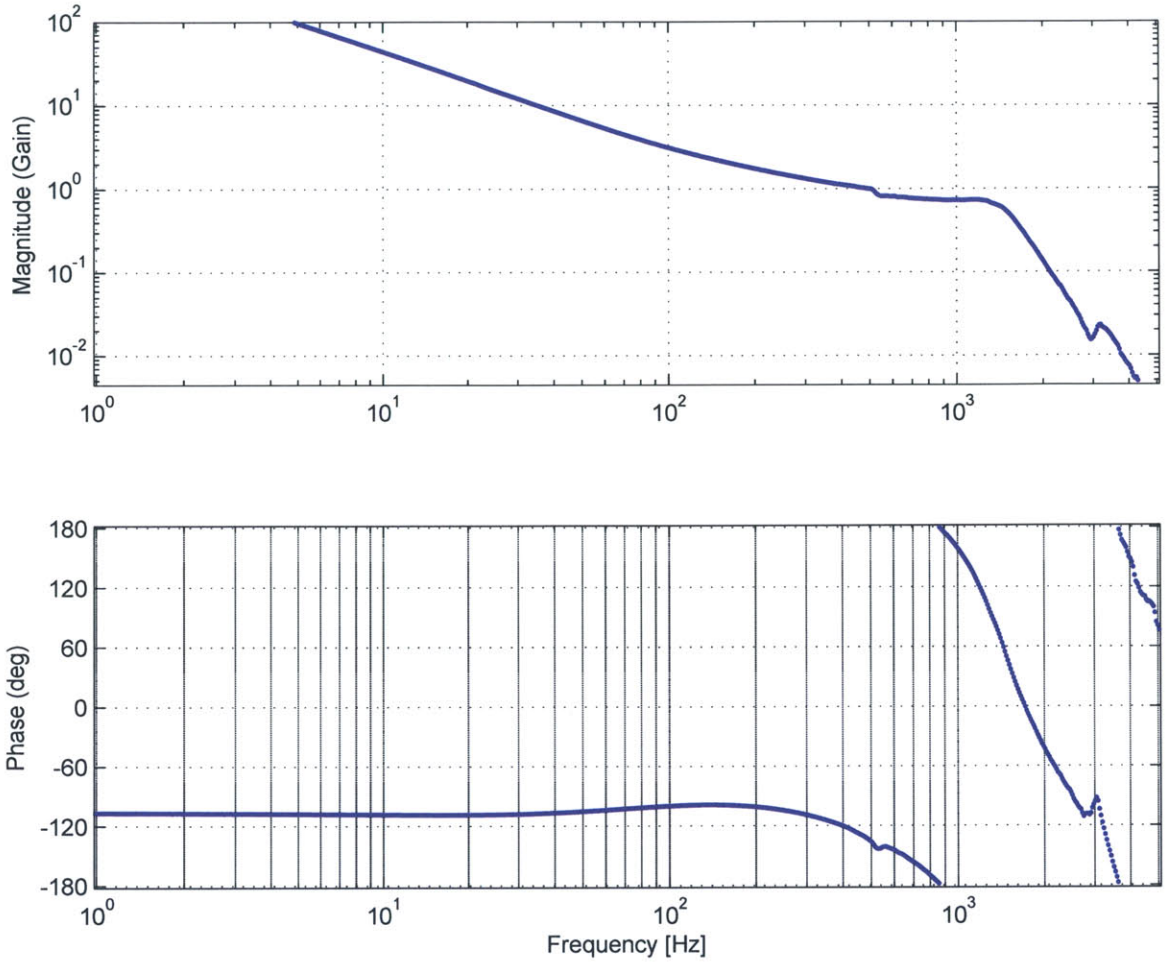

Figure 7-12: Expected nanopositioner loop transmission with the aggressive compensation of Equation 7.3.

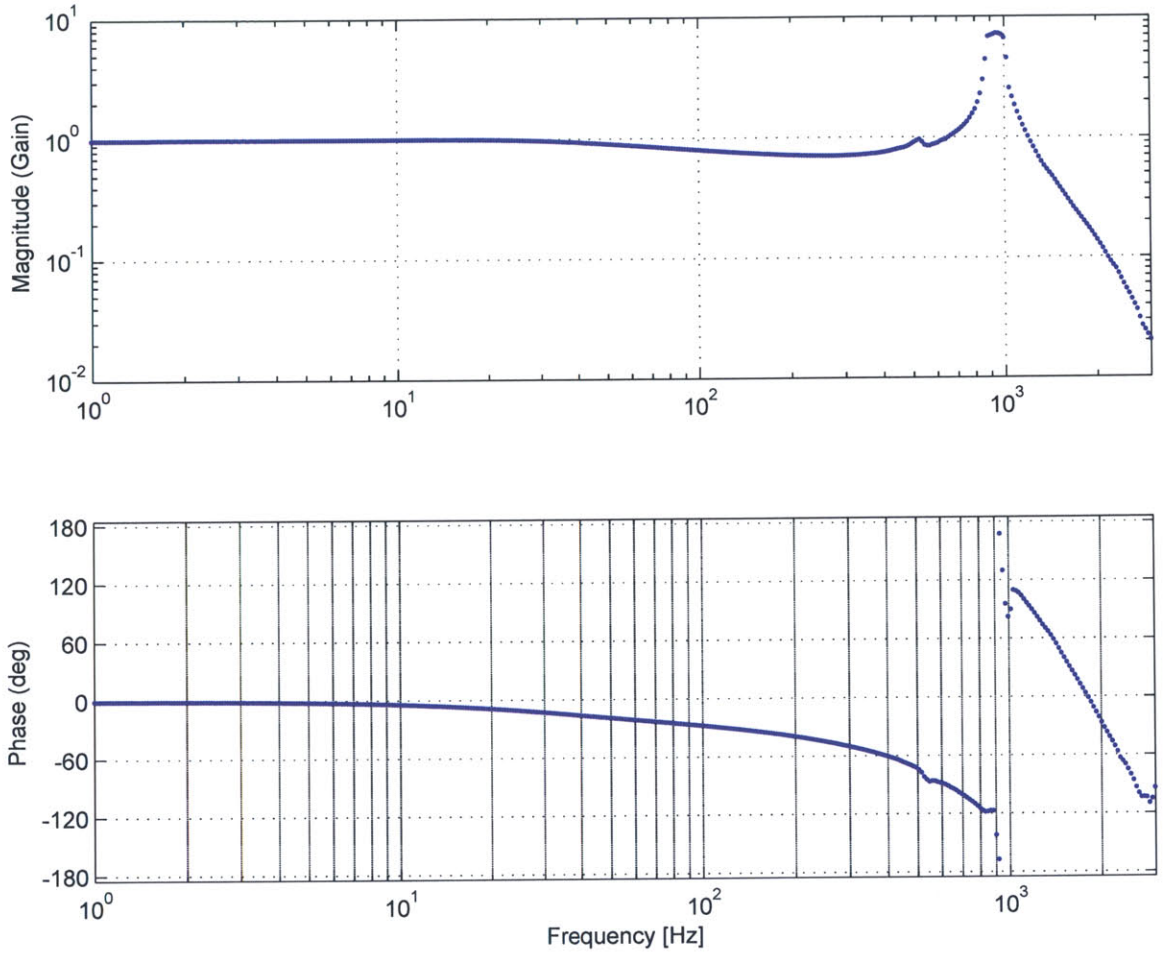

Figure 7-13: Closed-loop frequency response of the nanopositioner with the aggressive compensation of Equation 7.3.

The step response performance of the aggressively compensated nanopositioner is shown in Figure 7-14. The $10-90\%$ rise time is 325 μs giving a bandwidth estimate of 1.077 kHz from the $2.2/t_r$, which agrees with the closed loop frequency plot very well. The oscillation in the step response has a frequency of 1.08 kHz and a 2% settling time of 4.9 ms. A second step response is shown in Figure 7-15. The coil current is shown as well as the displacement during the 5 μm step response. The overshoot is somewhat ill-defined in this system due to the relatively long tail to the

final value and does not give a useful metric for measuring the system performance. The step response of this system disqualifies this controller from being considered for positioning applications that cannot tolerate large overshoots.

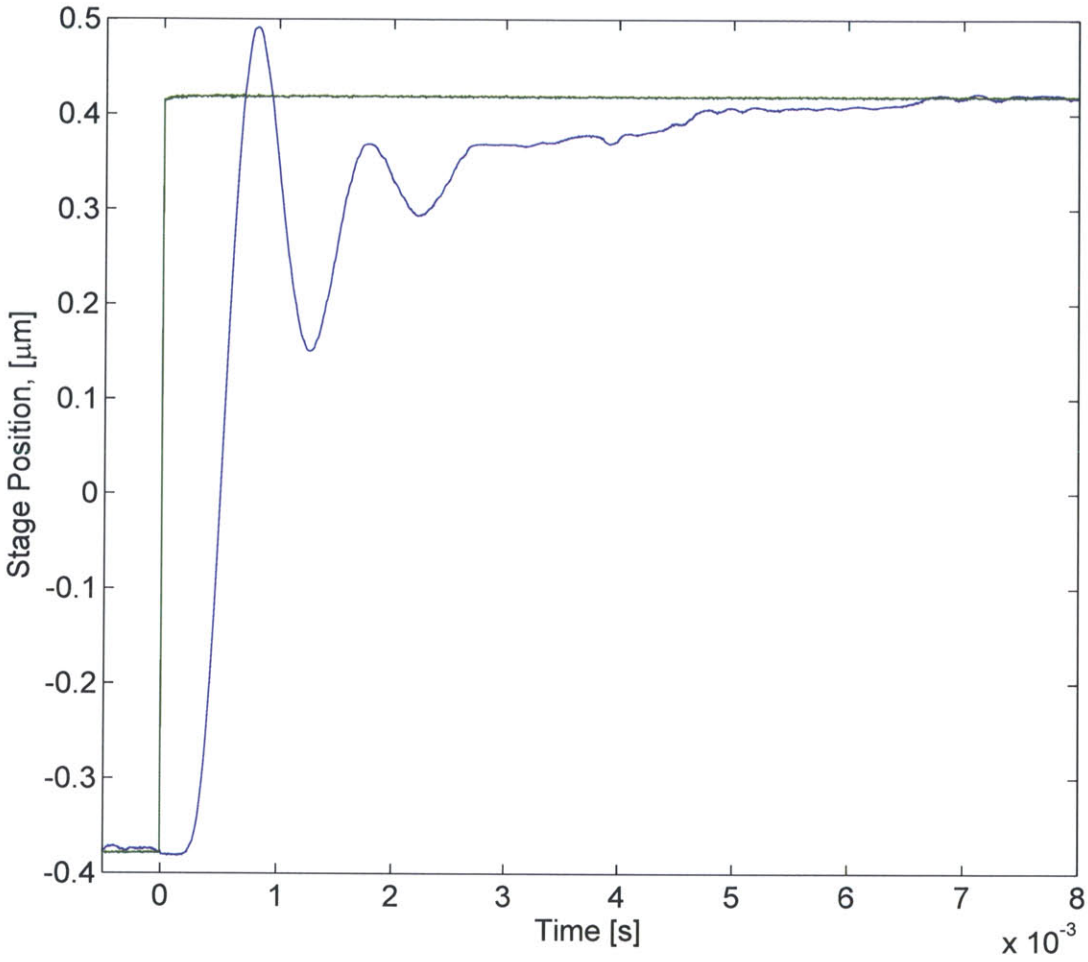

Figure 7-14: Nanopositioner step response for a 800 nm change in desired position when compensated with Equation 7.3.

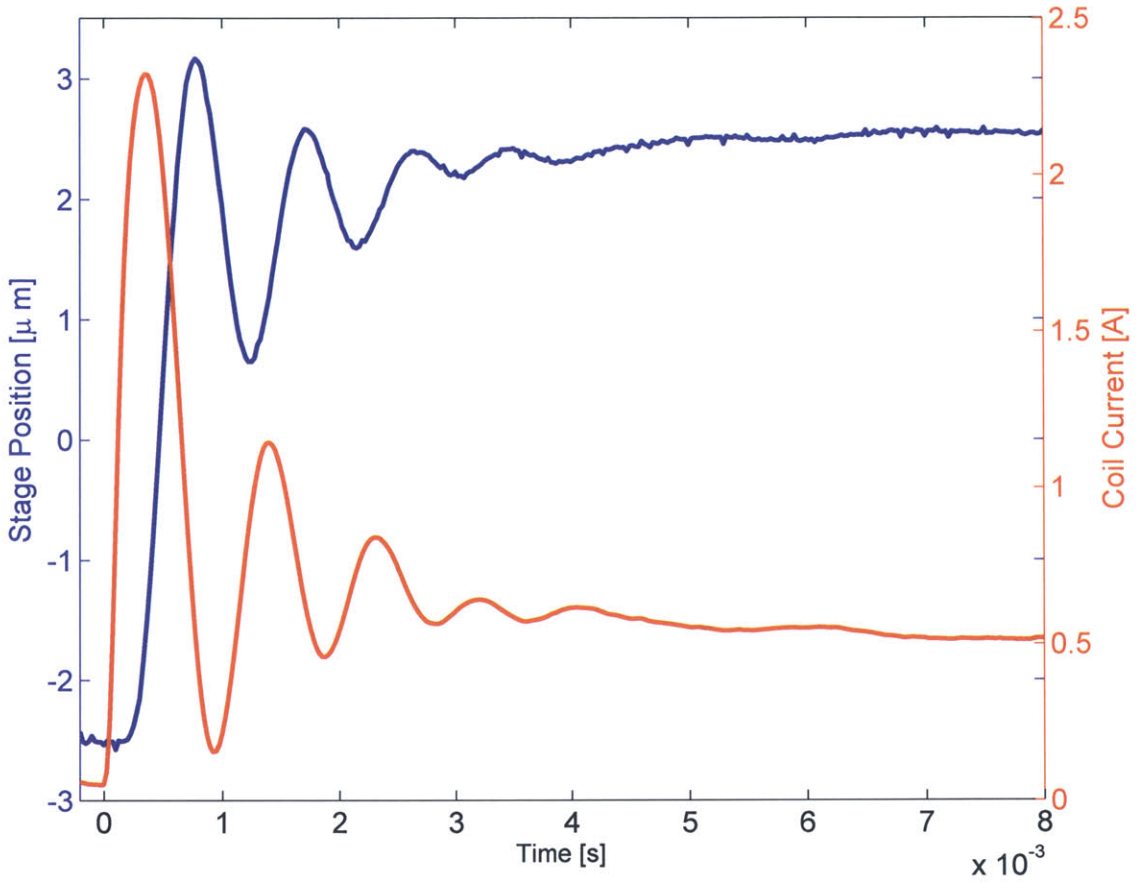

Figure 7-15: Nanopositioner stage position and coil current during a 5 μm step with the compensation of Equation 7.3.

7.2.2 Final Control

The performance goal of the final controller was to develop a compensator that would provide a nearly overdamped step response while maximizing the positioner bandwidth. These goals would be reached using the integral-lead control of Equation 7.1. Figure 7-10 displays the open-loop nanopositioner frequency response with capacitance sensor feedback that will be used to design the final controller.

The first issue to be covered is the decision to use a pure integrator in place of a more traditional lag compensator with the lag zero well below crossover. Figure 7-16 demonstrates the benefit of employing integral compensation in place of a lag compen-

sator. The integral compensation beneficially reduces the slope by -1 decade/decade and decreases the phase by 90° for all frequencies. The threat of the resonance at 1.2 kHz pushing above unity gain once the lead compensation is added has been greatly reduced. The worst case with the integral control is having the lead compensator placed such that the resonance point regains the original slope should the lead zero be located at a higher frequency than the resonance. The alternative situation with the lag compensator, rather than the integrator, is a resonance with an increased slope of $+1$ decade/decade over the open-loop resonance, which is a much larger threat of reducing the gain margin.

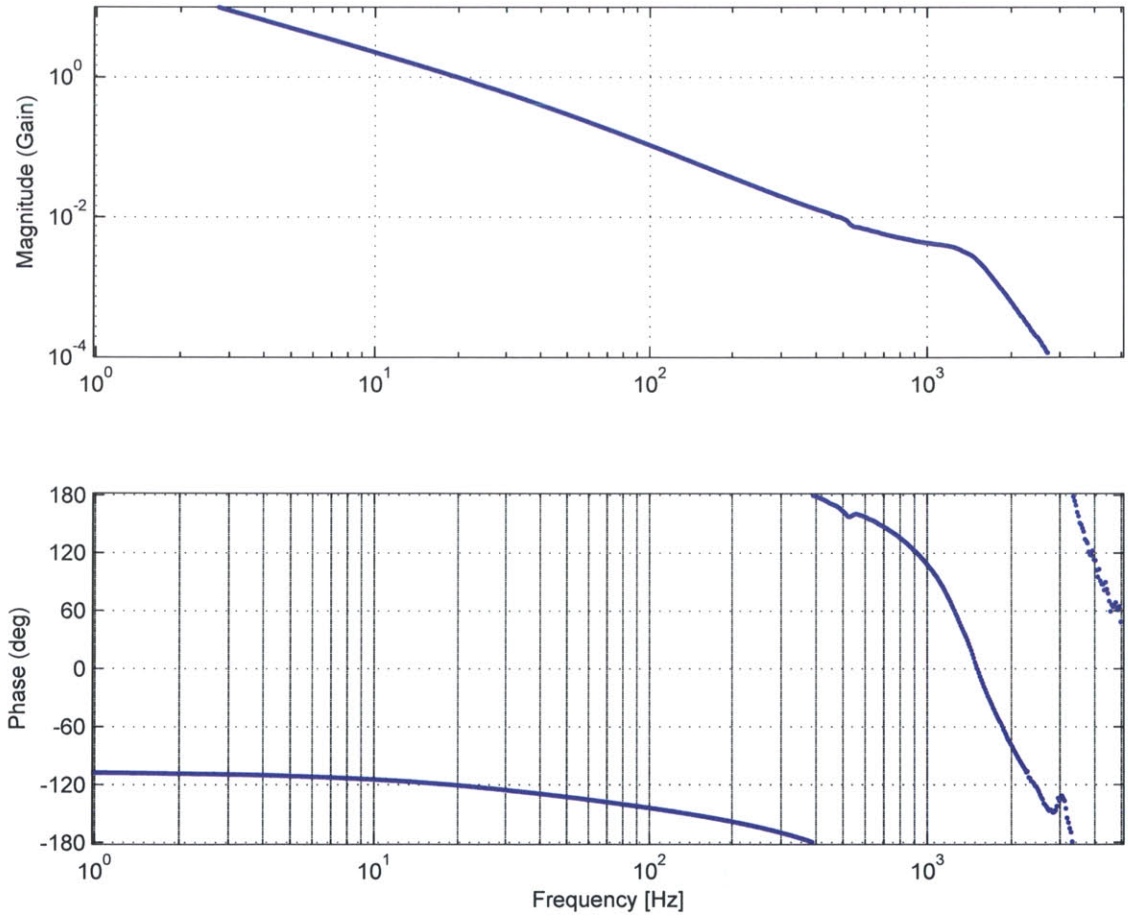

Figure 7-16: Integral compensated nanopositioner set to crossover at 20 Hz with 60° of phase margin.

The control design challenge is now to increase the phase to an acceptable level through a lead compensator while minimizing the magnitude of the resonance to keep the gain margin high enough the stability is good and the step response is acceptable. The following design was used as a starting point, while the final controller will be determined by tuning a gain, K, that is in series with the compensator to minimize the rise time while maintaining minimal overshoot.

Attenuation of the resonance and very high damping were desirable for the nanopositioner so the lead pole would be placed below the resonance and the α of the lead compensator was set to 0.1. The lead pole was initially place at 600 Hz, 1/2 the resonance frequency, and a gain adjustment to make the crossover point coincide with the maximum phase addition resulted in 78° of phase margin and a gain margin of 3 with crossover at 186 Hz. The continuous and discrete compensator transfer functions are shown in Equation 7.4. The loop transmission and the compensator used to reach that loop transmission on the nanopositioner are plotted in Figure 7-17.

$$G_c(s) = \frac{2960(s+377)}{s(s+3770)} = \frac{0.03551(z-0.9906)(z+1)}{(z-1)(z-0.91)} \tag{7.4}$$

An extra gain block was originally included in series with the compensation block to allow for tuning of the step response. After implementing Equation 7.4 through Simulink, the extra gain was adjusted while viewing the system response to a 1 μm reference change on an oscilloscope. The desired step response was overdamped with a minimal rise time. Setting this gain to 1.135 was experimentally found to give the desired step response. The resulting digital control law is given in Equation 7.5 after being rearranged to the parallel compensator form that allows the anti-windup limits on the integrator. The final control implementation is shown in Figure 7-18. The addition of the gain changed the crossover point to 200 Hz with 75° of phase margin and a gain margin of 2.6.

$$G_c(z) = \frac{0.0052494\,(z+1)}{(z-1)} + \frac{0.045118\,(z+1)}{(z-0.990619)}; \tag{7.5}$$

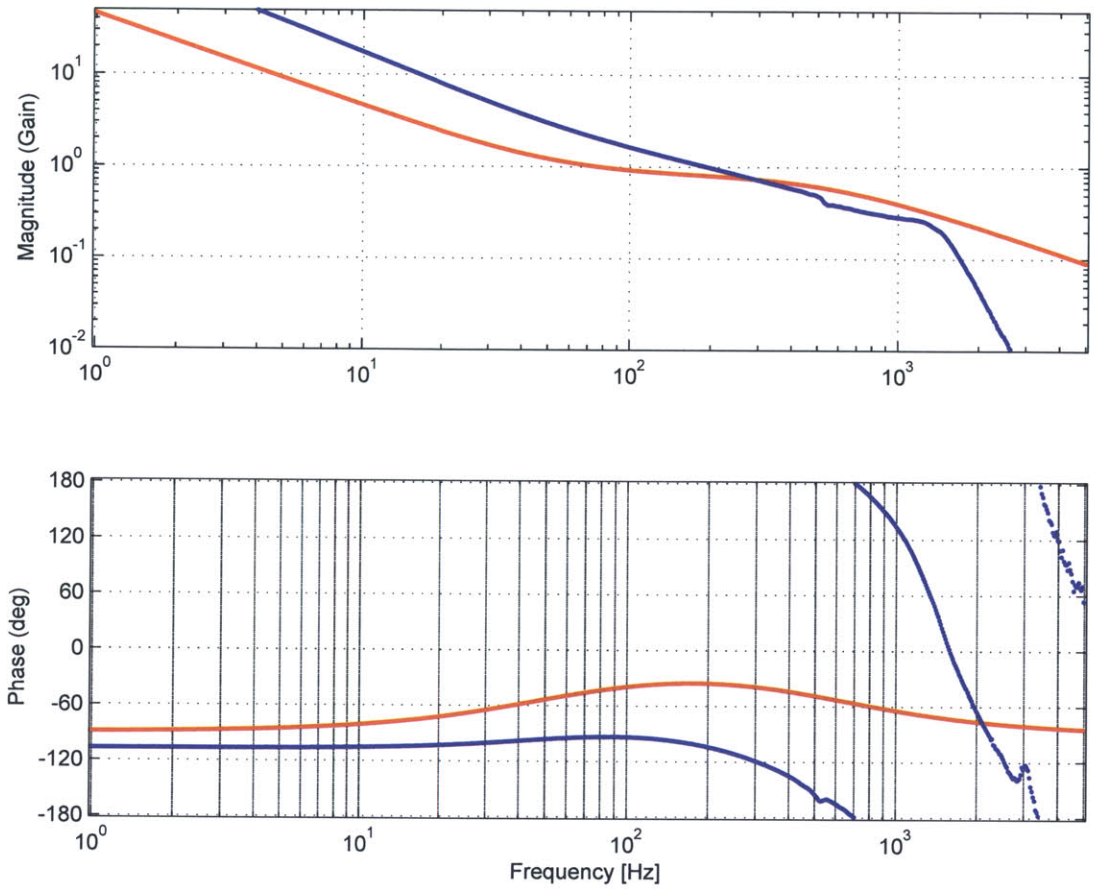

Figure 7-17: The expected loop transmission (red) and compensator frequency responses are compared.

The step response used to tune the final compensator is shown in Figure 7-19. It appears the gain could have been increased further when viewing Figure 7-19, however the positioner would quickly start to overshoot around 4.5 ms and the overshoot would grow and shift to the left. It is quite evident the step response is quite different than a second order system, which becomes even more apparent when looking at the 4 μm step response shown in Figure 7-20. The peak overshoot in the 4 μm step response actually occurs during the drift period around 7 ms rather than at the initial rise. This result may come from the interaction of integrator wind-up and the rubber dynamics. The final nanopositioner closed-loop frequency response is presented in Figure 7-21 and shows the -3 dB system bandwidth is 580 Hz.

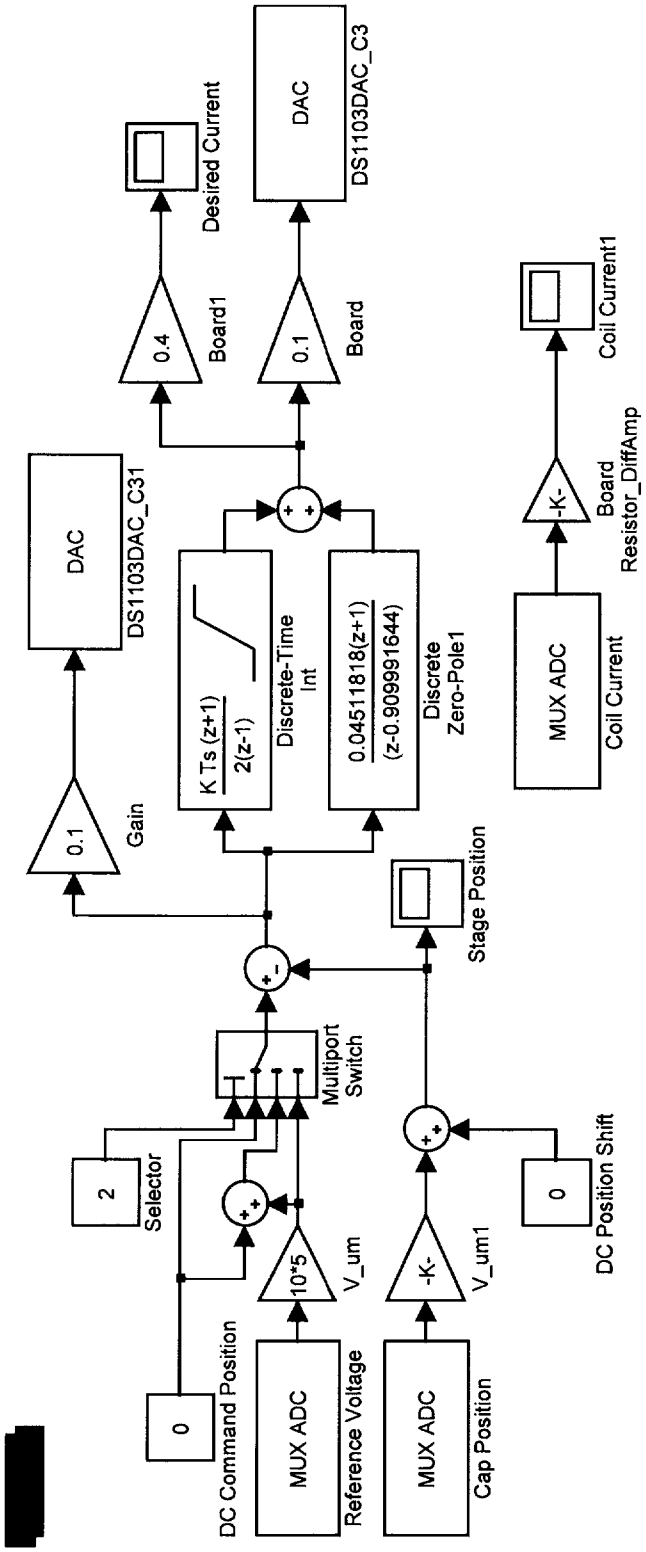

Figure 7-18: Simulink diagram implemented through dSPACE employing the digital equivalent of Equation 7.5 after adjusting the gain for a good step response.

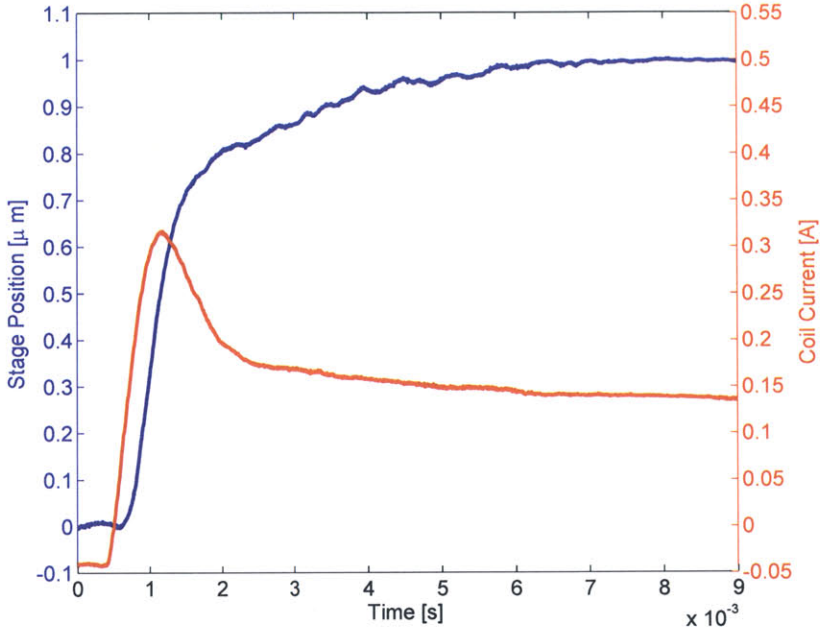

Figure 7-19: Response of the nanopositioner with the final compensation to a 1 μm reference step change.

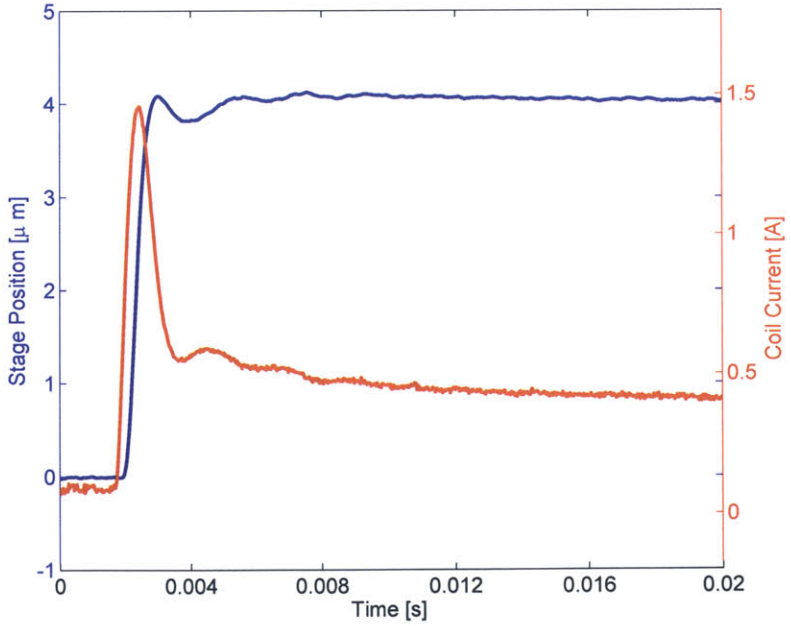

Figure 7-20: Response of the nanopositioner with the final compensation to a 4 μm reference step change.

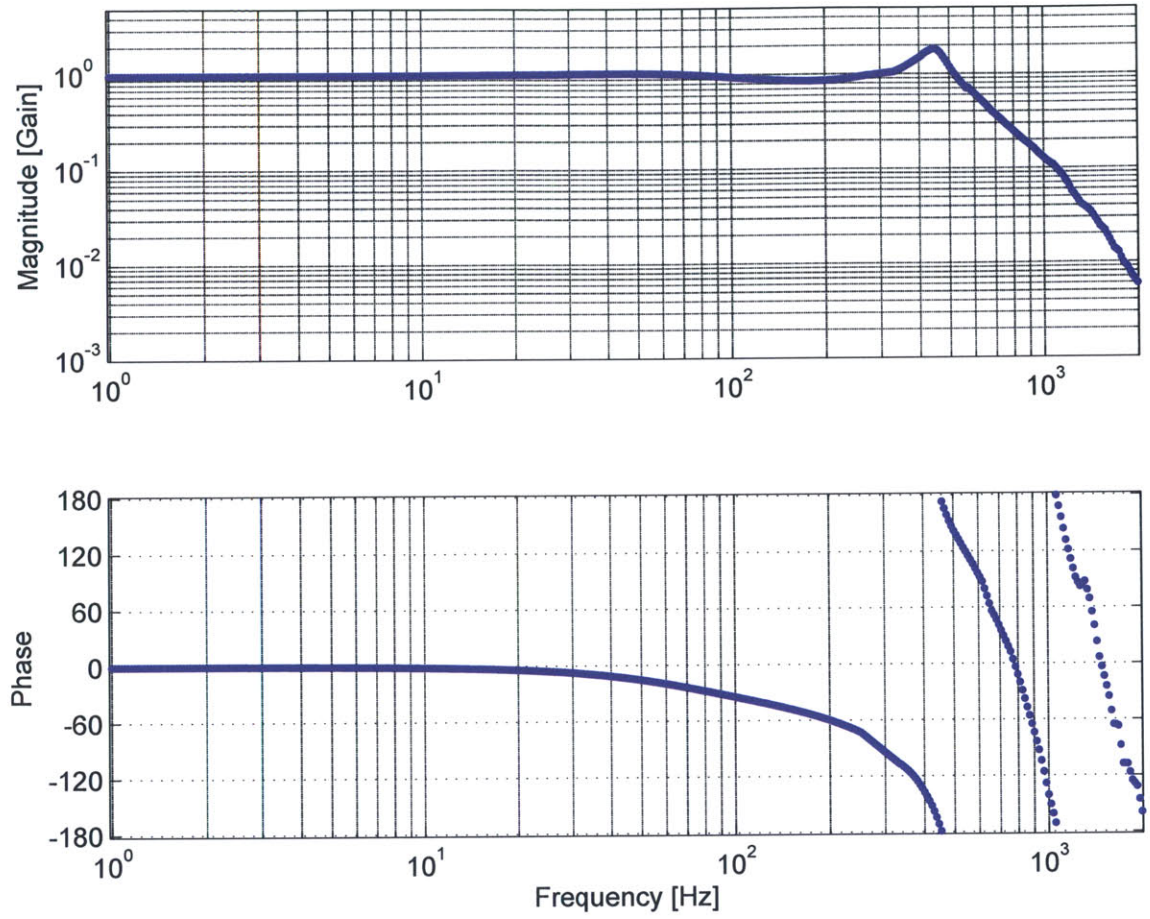

Figure 7-21: Closed loop frequency response with the final control implemented and obtained a closed loop bandwidth of 580 Hz.

Two examples of trajectory following of the nanopositioner are presented in Figure Figure 7-22 and Figure 7-23. Both examples demonstrate the hysteretic nature of the actuator and the rubber in that the coil current must lead the stage position in time.

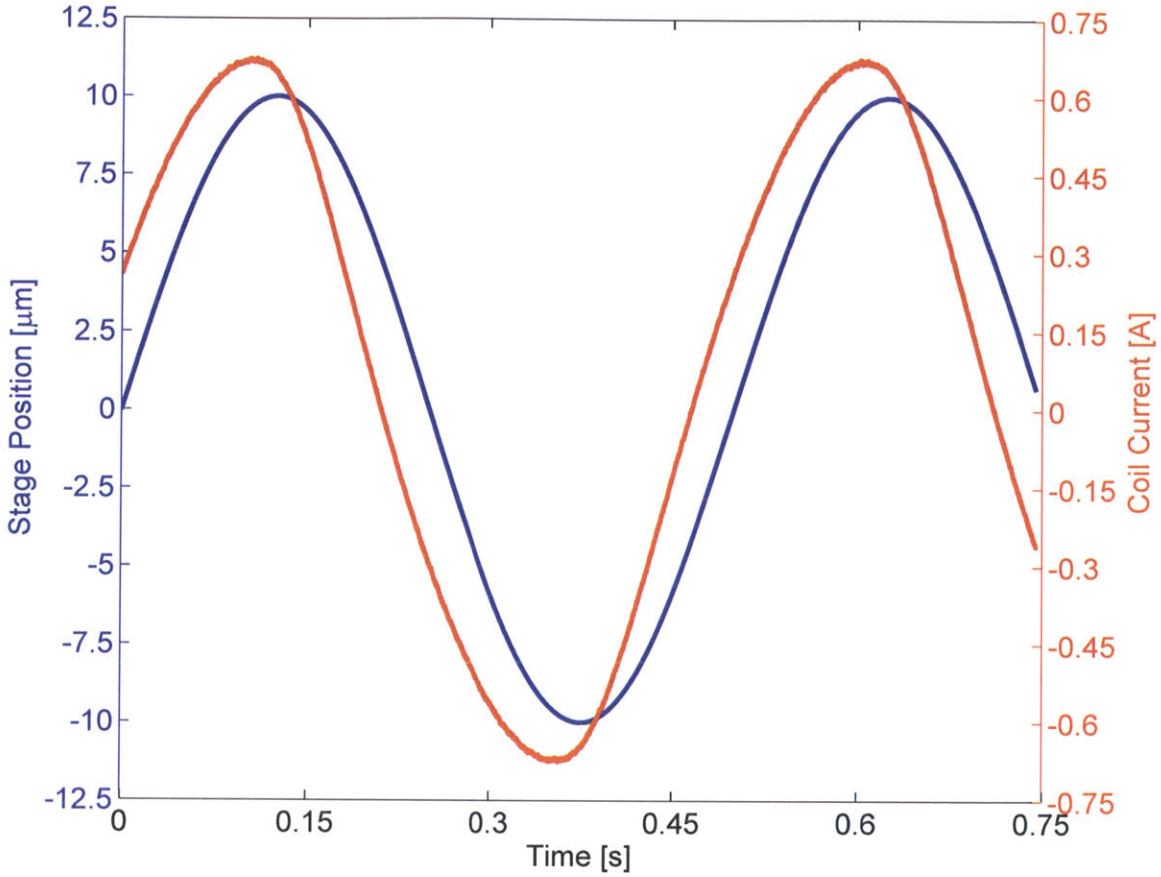

Figure 7-22: Coil current and stage position when the nanopositioner is following a 2 Hz, 20 μm peak-to-peak sinusoidal trajectory.

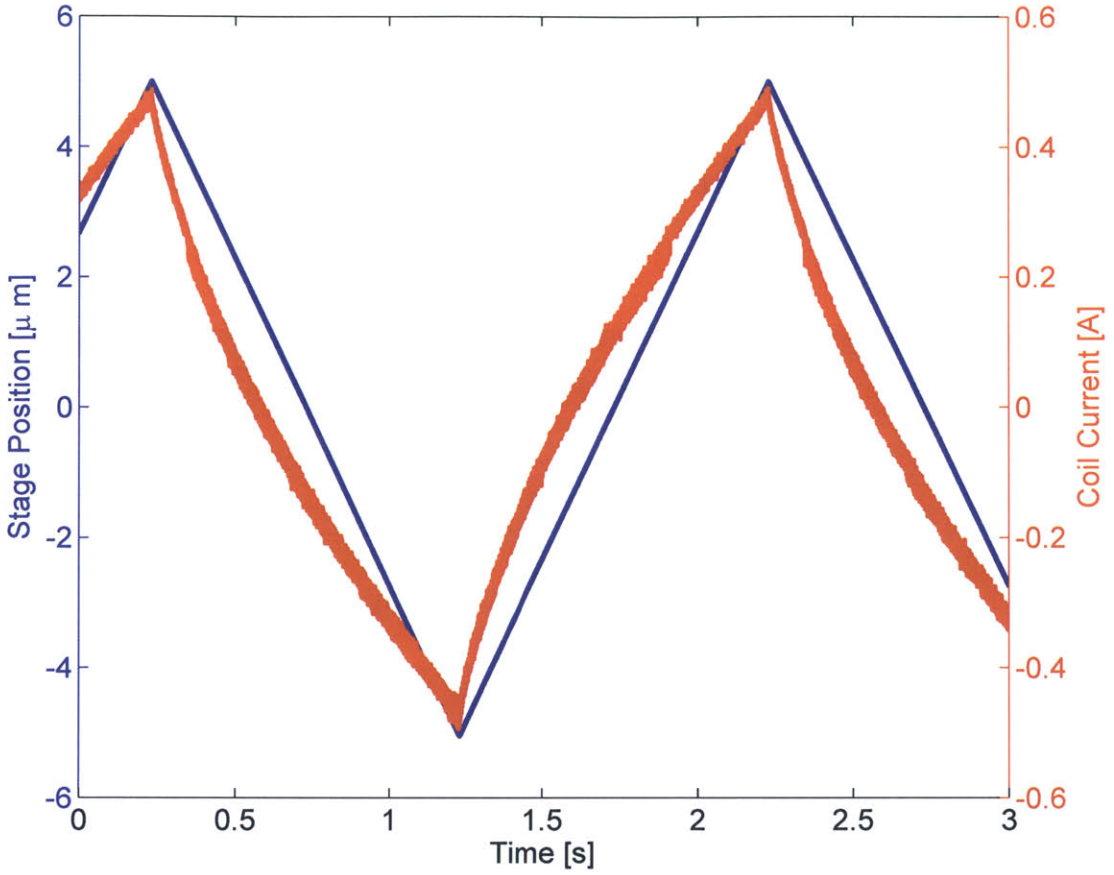

Figure 7-23: Response of the nanopositioner to a ± 3 μm triangle wave reference signal.

7.3 Actuator Force Capability

The actuator maximum force capability of 460 N was measured using an AC-coupled load cell mounted on a micrometer base. The AC coupling presented a slight challenge as only the dynamic force would effectively be measured although the actuator DC force capability was desired.

The fixturing of the load cell relative to the nanopositioner is shown in Figure 7-24. The stiffness of the load cell support post was quite low and deflected away from the nanopositioner as the a micrometer base was used to move the load cell against the nanopositioner face. The peak DC force was measured by pushing the load cell

against the nanopositioner until the coil current went to 4 A and the AC coupling of the load cell caused it to measured zero force. The load cell was then quickly removed from the nanopositioner and the maximum force would register with the load cell. The resulting force versus time plot looked like a tensile force impulse to the maximum force with an exponential decay that depended on the time constant setting of the electronics.

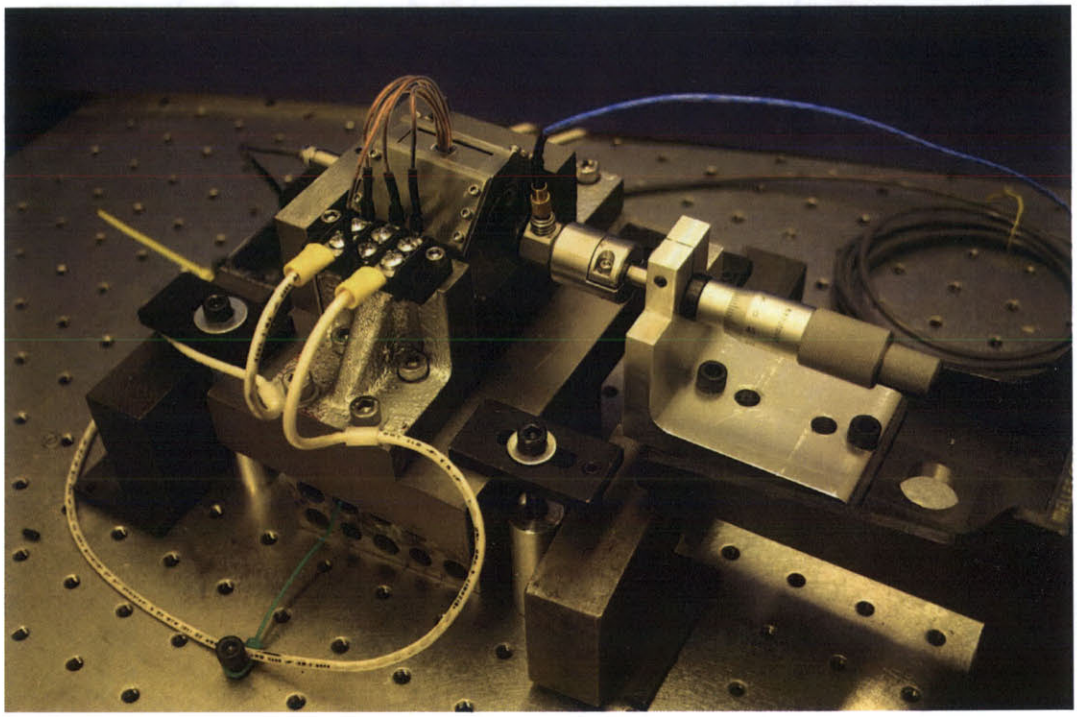

Figure 7-24: Configuration of the force cell relative to the nanopositioner.

7.4 Summary

The experimental setup used in running the nanopositioner and difficulties encountered using the laser interferometer sensing were outlined. Comparisons between the open-loop frequency responses for laser interferometer and capacitance distance sensing were presented to emphasize the negative effect of using the laser interferometer sensing. An aggressive control was developed that pushed the closed-loop bandwidth over 1 kHz with a step performance that was unacceptable. The final control that

had an acceptable step response gave a -3 dB closed-loop bandwidth of 580 Hz. The effect of magnetic hysteresis was shown for a sine wave with an amplitude that was 20% of total stage travel and a triangle wave trajectory that was 10% of total stage travel. Lastly, the maximum force capability of 460 N and the setup used to measure the force capability were presented.

THIS PAGE INTENTIONALLY LEFT BLANK

Chapter 8

Conclusions and Future Work

This thesis has demonstrated a new class of low cost nanopositioner based on a hard-linearized magnetic actuator with rubber bearings supporting the stage in all six DOF. This chapter will summarize the contributions of the thesis to the science involved in developing these nanopositioners. Suggestions for improving the nanopositioner design and future work are also presented.

8.1 Summary of Contributions

Contributions to the design of nanopositioners starts in Chapter 5 with the development of a casting process for producing rubber bearings from liquid rubbers. The liquid rubber materials identified as best for positioner applications are polyurethanes and silicone rubbers. Experimental results show that the analysis methods developed in Chapter 3 are still applicable to cast bearings.

The o-ring stacking concept was analyzed and it was determined such a bearing construction method could produce a suitable bearing system for precision machine applications when bulging interference is present. The amount of bulging interference is yet to be determined. The best hard-linearized magnetic actuator configuration was selected based on very compact packaging of all needed components. The selected configuration was analyzed in-depth to determine the force relations, nonlinearities, and voltage requirements. Design considerations were presented, followed by the

development of a nanopositioner model that combines the magnetic and mechanical domains. Several additional nanopositioner configurations are also presented in Section 6.5 that would employ the concepts covered in this thesis.

Controls issues and compensator development were discussed throughout Chapter 7. Chapter 7 concluded with experimental results and showed the constructed nanopositioner force capability of 460 N did not meet the maximum desired force of 680 N. The final system bandwidth was found to be 580 Hz when a moderate integral-lead compensator was employed.

8.2 Suggestions and Future Work

Many lessons were learned throughout the design, construction, and testing of the nanopositioner and this section will share these hard-earned design insights and possible research directions that should be pursued to further the state of the art in the design of nanopositioners in this new class.

8.2.1 Casting

The casting process developed in this thesis worked well in the laboratory environment and is scalable to nearly any level desired. However, some significant changes would be required when these bearings are cast as part of a commercial product.

A production level process would begin with a batch of mixed liquid rubber being de-aired in a vacuum chamber. Once de-airing is complete, the batch would be removed from the vacuum chamber and a positive pressure system would be used to fill the mold from the bottom up. The fill port would then be capped and the filled mold would be allowed to cure.

The primary variation from the process presented in this thesis is the positive pressure system. The speed at which the rubber fills the mold in a vacuum driven system is limited by the rubber viscosity as the maximum pressure differential available is one atmosphere. A positive pressure system would allow much faster filling of the mold as the pressure differential can be driven much higher. The positive pres-

sure system minimizes the effect the uncured viscosity has on the material selection process to add another design DOF.

One issue that was not directly addressed in this thesis was the issue of preload on the rubber bearing. Bearing preload does not play as large a role in cast bearings as it does in adhesively bonded rubber sheets as perfect conformance between the bearing shape and the support are guaranteed. However, an interesting idea for varying preload on the cast rubber bearings is to vary the curing environment temperature from the bearings in-service temperature. The coefficients of thermal expansion for steel and silicone rubber are drastically different at 13 m/m K x 10^{-6} and $30 - 300$ m/m K x 10^{-6}, respectively, which could provide an extra degree of design freedom. However, lowering the temperature may result in a significant increase in cure time.

The adhesion strength of the cast bearing with the support can also be increased by passivation of the support before bonding. Passivation changes the chemical composition and reactivity at the surface of a material. Passivation also has positive implications in regard to corrosion resistance of the support structure, as well as bond strength. Guides for passivation of stainless steel are provided in ASTM A967 [39].

A suggestion for furthering the understanding of cast rubber bearings with regard to the current testing fixture (See Section 5.4) would be to machine the pocket of the aluminum mold ring slightly deeper to produce thicker bearings. The mold design was intentionally setup to allow many rubber bearings of increasing thickness to be produced without requiring new hardware.

8.2.2 Electromagnetics

The actual force capability fell 32% short of the desired force capability. Part of the force deficiency was caused by not annealing the stainless steel magnetic parts after machining, but before assembly. The machining process leaves residual stresses in the material that lower the magnetic permeability and saturation flux, while increasing the coercive force. Although the actual state of the stainless steel used in the positioner was unknown, a proper anneal would have increased the force capability and

decreased the magnetic hysteresis. Increased force capability and decreased hysteresis are both desirable so a proper anneal should be required in upcoming nanopositioners.

Another factor that likely decreased the actuator force capability is magnetic saturation near the permanent magnets in the inner and outer pole pieces. There are non-aligned flux contributions from both the magnets and the coils in this area making it a likely choke point for all magnetic flux in the circuit. This choke point could be prevented by increasing the magnetic material in these regions. Equivalent flux density in the gap could be achieved by tapering or otherwise decreasing the pole area near the air gap where saturation is less likely.

8.2.3 Rubber Bearings

Although a casting technique was developed in this thesis, the bearing system employed in the nanopositioner was created using adhesively bonded sheets. Two suggestions for those that may repeat this technique in the future are to use a two-part silicone adhesive rather than the single-part adhesive that has trouble curing in thick sections and apply a thin layer of adhesive to the rubber sheet before applying the rubber sheet to the support. A technique that was found to work well was to dab adhesive on the rubber using a paper towel and visually ensure complete coverage before rolling the sheet down on the support to prevent air from becoming trapped.

The single-part silicone adhesives cure with exposure to moisture which can be convenient, although thick bond lines may never cure. The cure mechanism for common single component RTV silicone rubber is also a reaction with moisture. Sections of these single component curing materials may never cure as cured silicone adhesive, silicone rubber sheeting, and most support materials are impervious to water. Therefore, silicone adhesive near the middle of the pad is protected from moisture as once the edges cure, the moisture is locked out. A two-part silicone adhesive is better suited for adhering silicone rubber pads to the support as all components needed to cure are available after mixing is complete.

The o-ring investigation of Chapter 6 shows the o-ring stacking concept could be used as a bearing system in a precision machine if bulging interference is incorporated

in the design. More work is needed to experimentally verify the methods developed in this thesis are accurate and then to determine the level of bulging interference required to reach the 20 N/μm stiffness required in precision machines.

Rubber bearing design can also benefit from the work done in the tire industry and helicopter rotor hubs. Rubber structures in the tire industry are composite structures that incorporate steel, nylon, and other materials to create anisotropic stiffness in the structure.

An alternative to macroscopic composite structures, as seen in the tire industry, is microscopic composite structures. These microscopic composites could employ conductive or magnetic particles suspended in the liquid rubber which could be aligned prior to curing by an electric or magnetic field to give anisotropic stiffness.

Rotary rubber bearing systems will be a useful addition to this class of nanopositioner and can benefit from study of the helicopter rotor hubs that can accommodate rotary motion while supporting substantial loads. One important lesson will be aligning the centers of pressure from multiple laminate stacks to enable long and trouble free operation [43].

8.2.4 Nanopositioner

Suggestions for use of and improvements to the nanopositioner developed in this work will now be presented. The first improvement that could be incorporated into the nanopositioner is laser welding of the end caps to the struts. Laser welding would eliminate 24 bolts from the moving mass and also allow the end caps to be have chamfers around one end of the outside. The chamfers would eliminate mass that is not structural and does not carry flux.

The concept of Figure 6-28 could be employed with matching glass scales on opposite sides to of the current nanopositioner to verify the six DOF stage stiffness and measure any parasitic motion.

The final suggestion of this thesis is to incorporate cast rubber bearings into the current nanopositioner design. The struts that are currently employed are thicker than necessary due availability and the desire for a very robust stage. A rectangular

o-ring groove could be machined into the strut surface currently in contact with the rubber bearing. The o-ring would then be captured between the strut and the actuator outer pole. Two molding ports would then need to be drilled through the strut to allow casting of the rubber bearing. The o-ring that defines the mold cavity would become an integral piece of the bearing after casting.

Two issues in need of investigation to allow this system to be robustly designed are how well does the cast bearing adhere to the o-ring and what is the stiffness of this hybrid o-ring/cast bearing in compression and shear.

8.3 Conclusion

This thesis has demonstrated a new class of low cost nanopositioner based on a hard-linearized magnetic actuator with rubber bearings supporting the stage in all six DOF. Contributions to the state of the art in nanopositioning include a robust, compact, and low cost bearing system, a hard-linearized electromagnetic actuator, and a casting technique that allows uniform and robust rubber bearings to be constructed in precision machines.

Appendix A

MATLAB Scripts

A.1 Compression Modulus Plot

```
% Variation of compression modulus with shape factor


% David Cuff

% 11-11-2005


clear;clc;


% Column 1 is Shore A Hardness, Column 2 is correction factor k, Column 3

% is Young's Modulus, Column 4 is Bulk Modulus,

%%Compiled from Lindley 1978

hard=[35:10:75]';k=[0.89 0.8 0.64 0.54 0.52]';E=[168 256 460 830 1340]';

E_inf = [142000 142000 154000 171000 189000]';

E=E*6894.7; E_inf = E_inf*6894.7;% Convert from psi to Pa

prop=[hard k E E_inf]

ll=0.1;lu=50;    % Limits of shape factor axis

S=1:1000;S=S*(lu-ll)/1000;

for i=1:5

    for j=1:1000

        E_c(j,i)=(1/(prop(i,3)*(1+2*prop(i,2)*S(j)^2))+1/(prop(i,4)))^(-1);
```

```
    end
end

loglog(S,E_c/1e6,'b','LineWidth',2);grid on;
xlabel('Shape Factor','FontSize',18),ylabel('Compression Modulus [MPa]','FontSize',18)
%title('Compression Modulus with Shape Factor','FontSize',20)
set(gca,'FontSize',18,'fontname','arial');
set(gca,'XTick',[0.1 0.5 1 5 10 50])
set(gca,'YTick',[1 5 10 50 100 500 1000])
axis([ll lu 0.9 max(max(E_c))/1e6])
str1(1)={' Shore A'};
str1(2)={'Hardness'};
str2=num2str([hard(5),hard(4),hard(3),hard(2),hard(1)]');
text(0.25,22,str1,'FontSize',20,'color','r')
text(0.4,4,str2,'FontSize',20,'color','r')

set(gcf, 'PaperPositionMode', 'manual');
set(gcf, 'PaperUnits', 'inches');
set(gcf, 'PaperSize', [7.5 5.75]);
set(gcf, 'PaperPosition', [-0.1 -0.0 8 6]);
print
```

A.2 Single O-ring Radial Stiffness

```
% Obtain the force versus displacement curve for radial o-ring bearing

% David Cuff
% 5-30-2005
% MS Thesis

clear;clc;
```

```
% Linear resolution

res=0.0000005

peak_disp=0.0005

xdisp=0:res:peak_disp;

for i=1:length(xdisp)

    F(i)=oring_force_calc(xdisp(i));

end

figure(1)

plot(xdisp*1000,F,'b-','LineWidth',2),ylabel('Force [N]','Fontsize',16),xlabel('Displacement [mm]','Fontsize',16)

set(gca,'FontSize',14,'fontname','arial');

%title('Force versus Displacement for Single O-ring')

figure(2)

K=diff(F)/res;

plot(1000*xdisp(1,1:length(K)),K/1e6,'b-','LineWidth',2),ylabel('Stiffness [N/\mum]','Fontsize',16),xlabel('Displacement [mm]','Fontsize',16')

set(gca,'FontSize',14,'fontname','arial');

%title('Radial Stiffness of 2mm thick o-ring with 25.4mm major Dia')


figure(1)

set(gcf, 'PaperPositionMode', 'manual');

set(gcf, 'PaperUnits', 'inches');

set(gcf, 'PaperSize', [7.2 5.8]);

set(gcf, 'PaperPosition', [-.4 -.18 8.1 6.3]);

%print


figure(2)

set(gcf, 'PaperPositionMode', 'manual');

set(gcf, 'PaperUnits', 'inches');

set(gcf, 'PaperSize', [7.3 5.8]);

set(gcf, 'PaperPosition', [-.2 -.18 8.1 6.3]);
```

```
print
```

A.2.1 Function oringforcecalc.m

```
function F=oringforcecalc(xp);

% Calculate force for a given o-ring deflection



% David Cuff

% MS Research

% 5-26-2005



d=0.002;  % Seal thickness

r1=0.025/2;r2=0.029/2;  % Radii of cylinders

og=r2-r1; d=og;    % Original gap size in meters

E=7170000; % Modulus of Elasticity Shore A 70

%xp=0.00025;   % Peak displacement*******Removed when changed to function

% Discretize

n=50; % Number of steps (should be even to avoid rad = 0);

drad=pi/(n+1);

for i=1:n+2

    rad(i)=-pi/2+(i-1)*drad;   % Shown as theta1 in drawings

end

%polar(rad+pi/2,10*ones(1,length(rad)),'*')



% Find the squeeze at each point, xs

for i=1:length(rad)

[gap(i),theta2(i),theta3(i)] = squeezering(r1,r2,rad(i),xp);

end

xs=(og-gap);

%figure(2),plot(rad,xs/og),title('Squeeze'),xlabel('\theta_1')



% Calculate force at each point in vector
```

```
for i=1:length(xs)

    f(i)=d*E*(1.25*(xs(i)/d)^1.5 + 50*(xs(i)/d)^6);

end

F=trapz(f)*drad*r1;
```

A.2.2 Function squeezering.m

```
function [gap,theta2,theta3] = squeezering(r1,r2,theta1,xp)

% Written by David Cuff

% Angles are given in radians


theta3=asin(xp/r2*sin(pi-theta1));
theta2=theta1-theta3;
if theta1==0
    gap=xp;
else
    gap=r2*sin(theta2)/(sin(pi-theta1))-r1;
end


% theta=-90:90;for i=1:length(theta)
% [gap(i),theta2(i),theta3(i)] = squeezering(100,110,theta(i),5);
% end
% plot(theta,gap,theta,theta2,theta,theta3)
% legend('gap','theta2','theta3')
% xlabel('\theta_1')
```

THIS PAGE INTENTIONALLY LEFT BLANK

Appendix B

Manufacturing and Assembly Photos

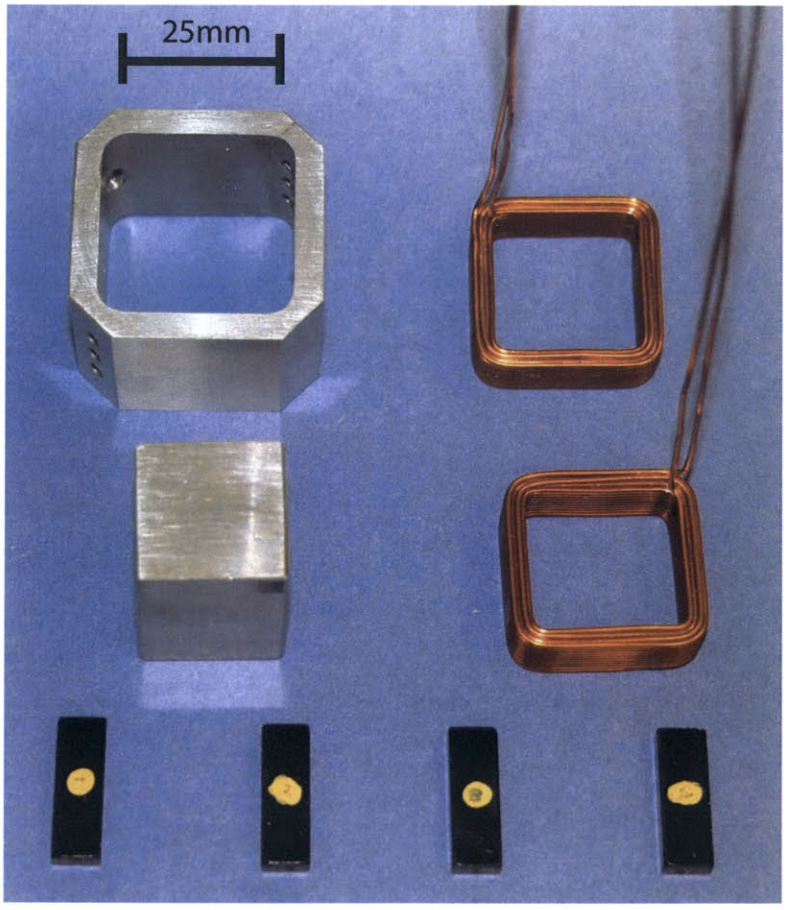

Figure B-1: All components contained in actuator body.

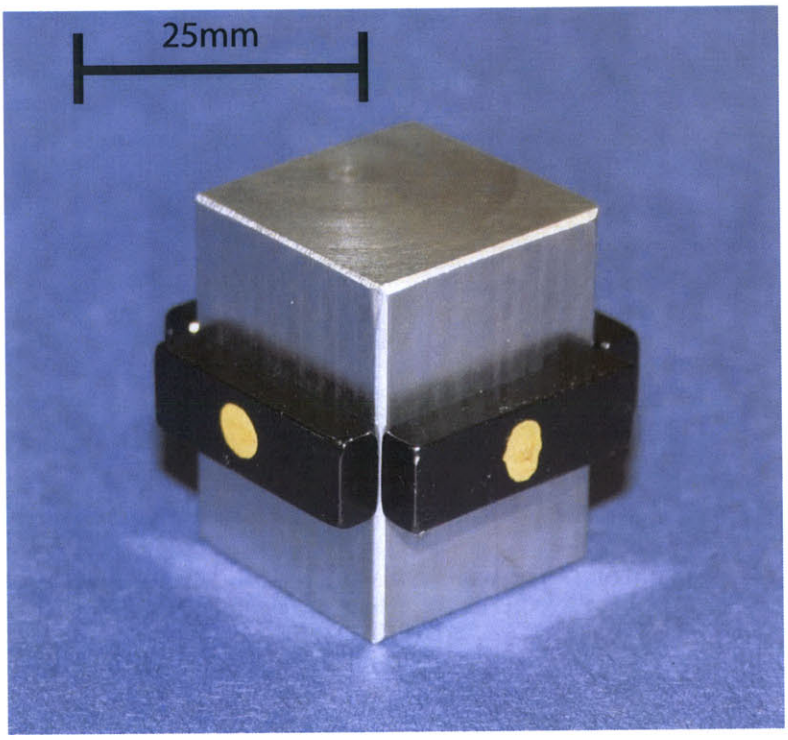

Figure B-2: Assembled inner pole piece and permanent magnets.

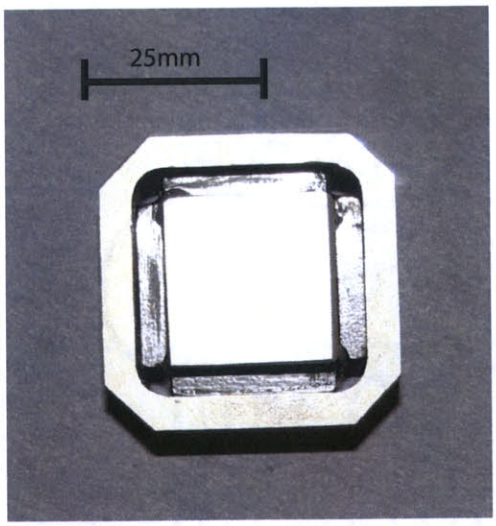

Figure B-3: Assembled inner pole, permanent magnets, and outer pole.

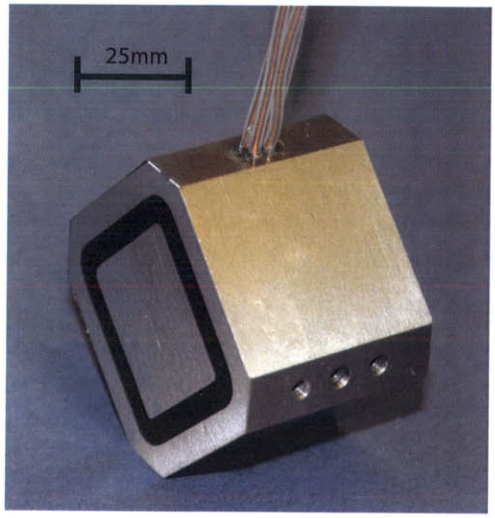

Figure B-4: Actuator body with coils potted and pole faces ground flat.

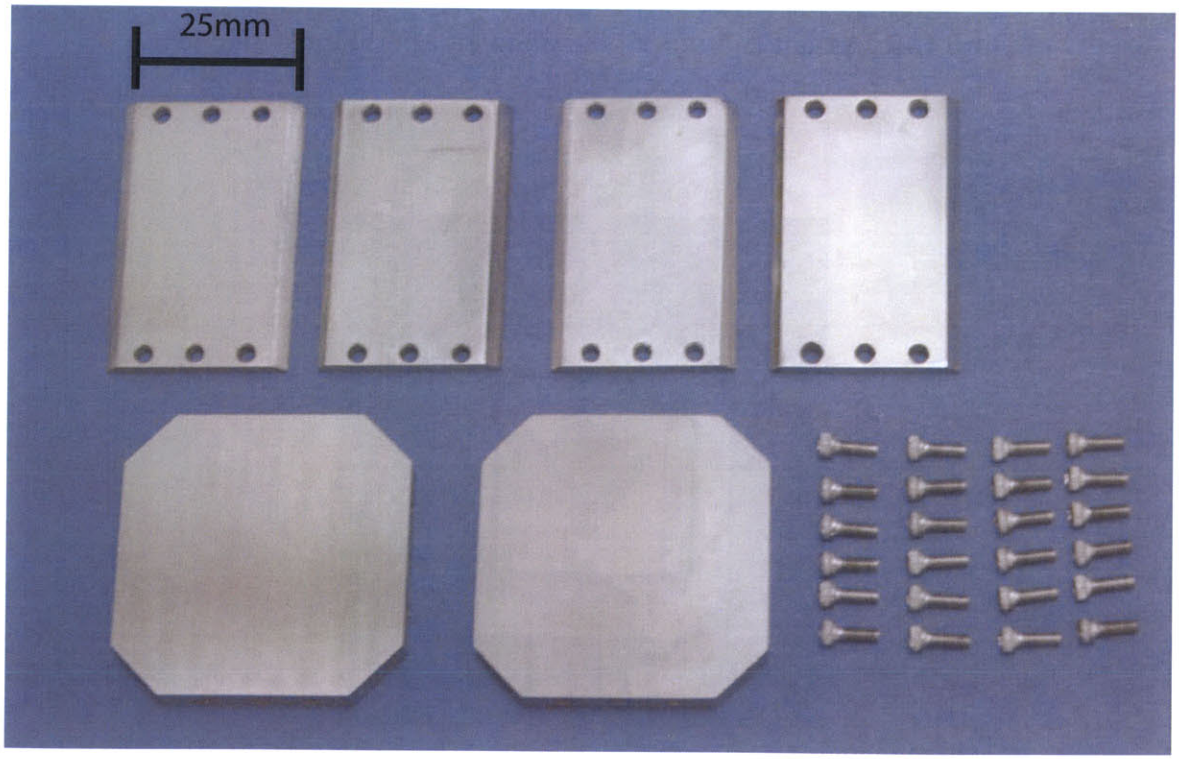

Figure B-5: All components of the stage and only moving elements.

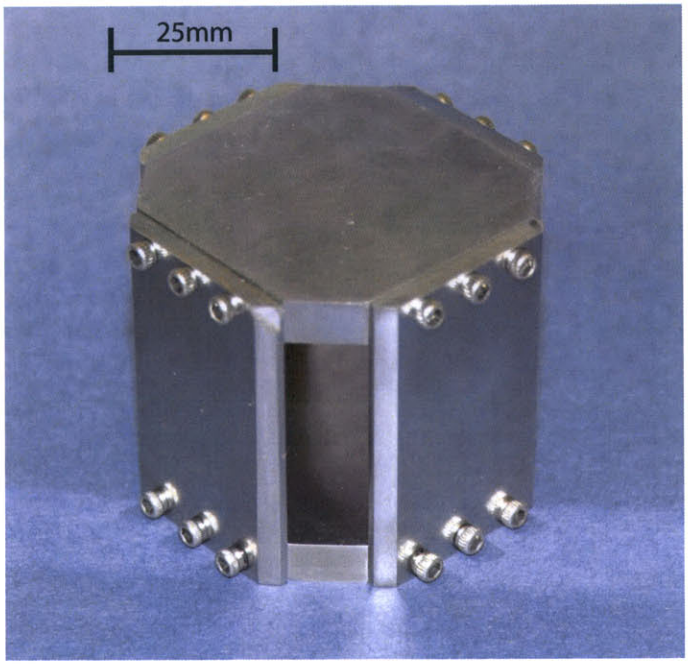

Figure B-6: Assembled stage.

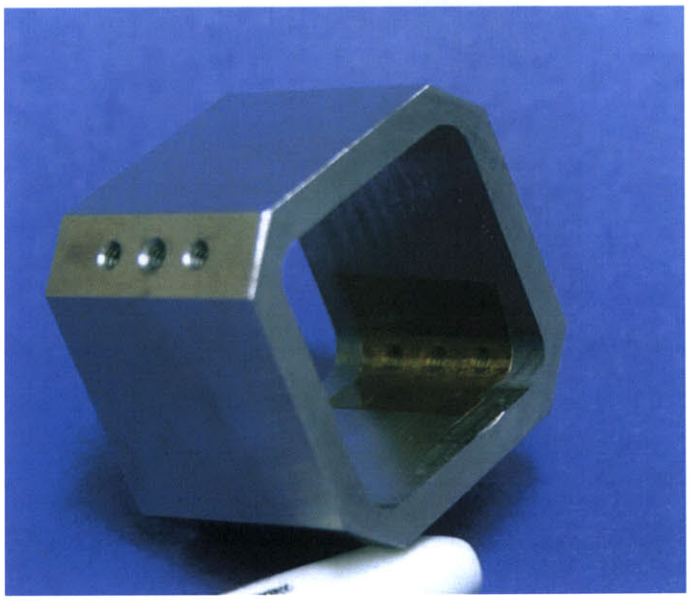

Figure B-7: Shows the layer of tape used to seal the coil slot during potting.

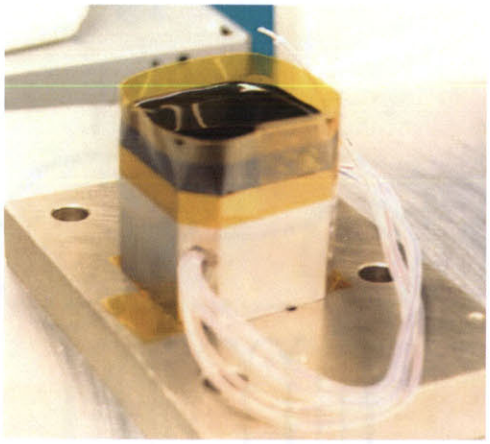

Figure B-8: Actuator after first potting attempt.

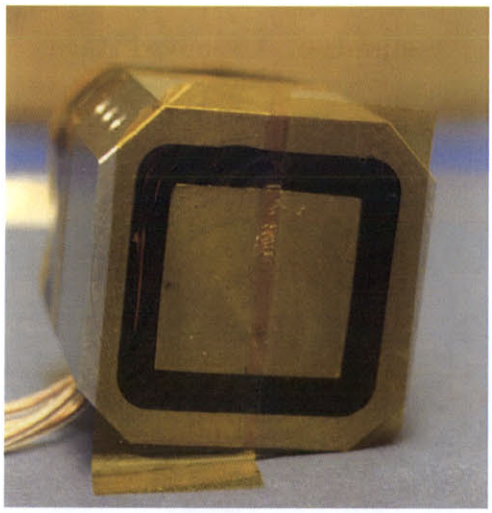

Figure B-9: Shows exposed coil on bottom side of window after first potting attempt.

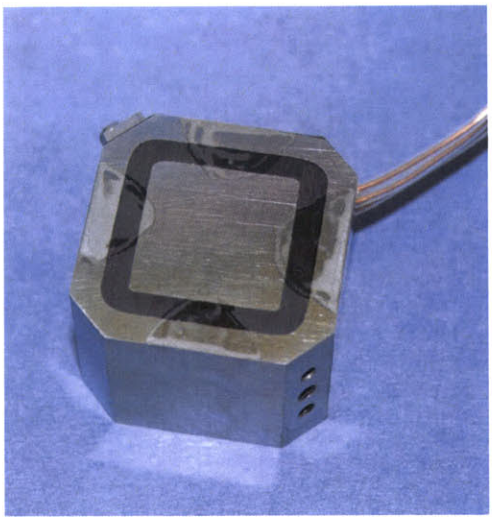

Figure B-10: Polyurethane hard stop pattern painted on ground pole faces.

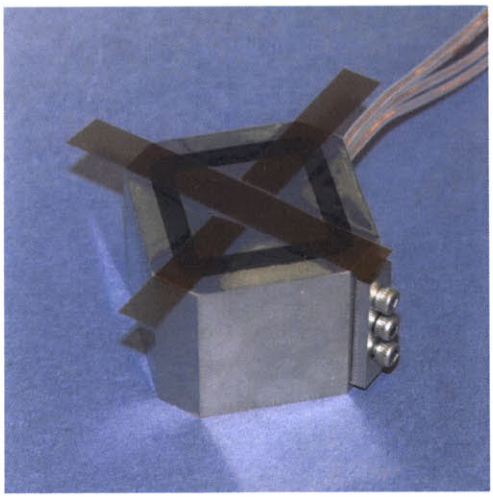

Figure B-11: Shim configuration for holding proper air gaps during assembly.

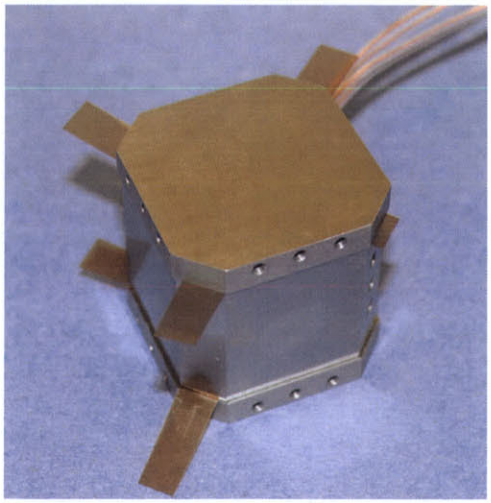

Figure B-12: End caps shimmed in place on actuator body.

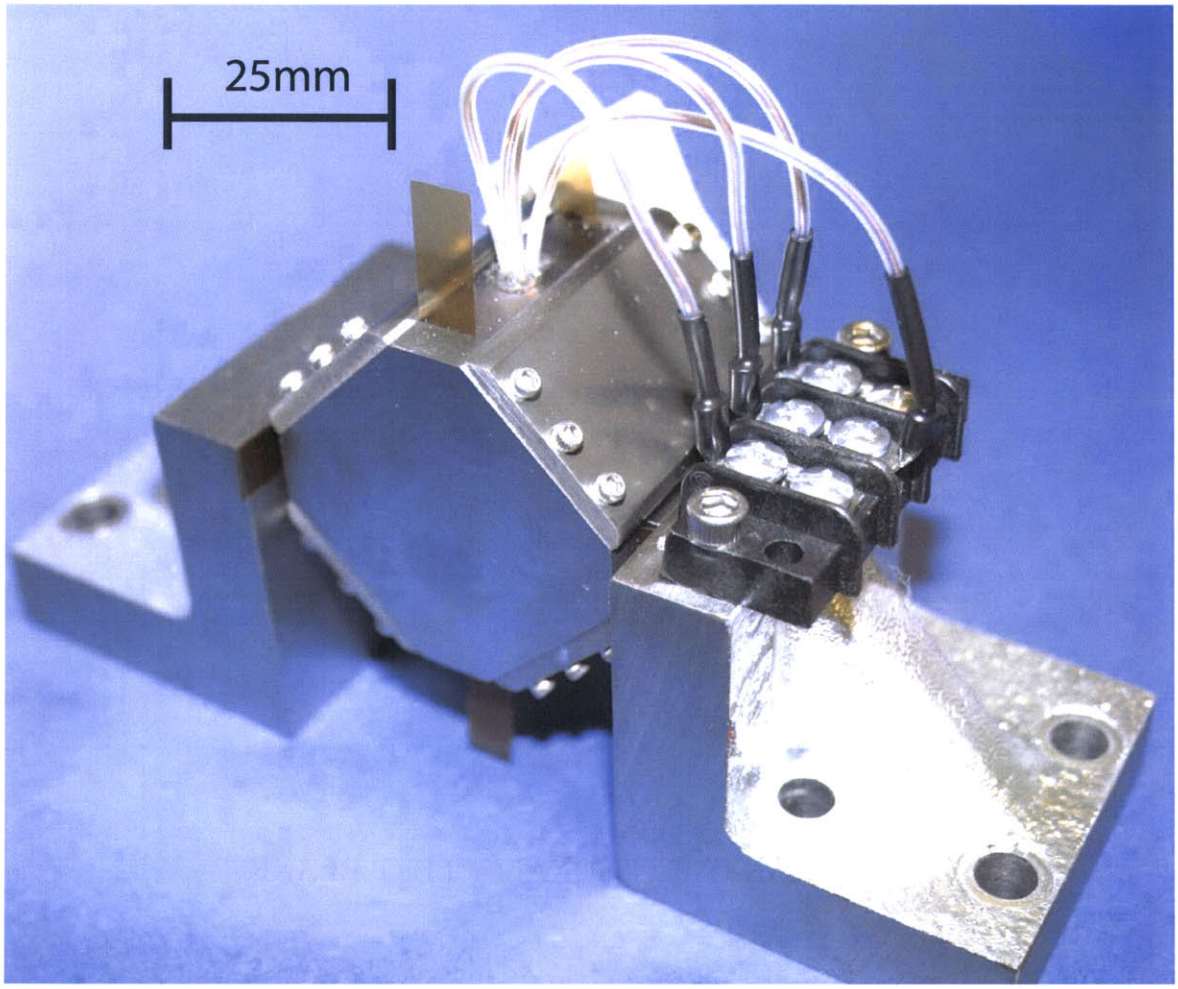

Figure B-13: Assembled nanopositioner on angle brackets.

THIS PAGE INTENTIONALLY LEFT BLANK

Bibliography

[1] John P. Henderson Ahid D. Nashif, David I.G. Jones. *Vibration Damping.* John Wiley and Sons, Inc., 1985.

[2] James Benjaminson. The 1931 plymouth pa: Walter chrysler's fistful of aces. *Plymouth Bulletin*, Reprinted at http://www.allpar.com/old/pa-plymouth.html.

[3] Gary H. Blackwood. *Active Vibration Isolation for Controlled Flexible Structures.* PhD dissertation, Massachusetts Institute of Technology, Department of Aeronautics and Astronautics, 1994.

[4] J.J.C. Busfield and C.K.L. Davies. Stiffness of simple bonded elastomer bushes part 1 - initial behaviour. *Plastics, Rubber and Composites*, 30(5):243 – 257, 2001.

[5] Kuo-Shen Chen. A spring-dominated regime design of a high load capacity, electromagnetically driven x-y-θ stage. Master's thesis, Massachusetts Institute of Technology, 1995.

[6] Shih-Chi Chen and Martin L. Culpepper. Design of a six-axis micro-scale nanopositioner-μhexflex. *Precision Engineering*, 30(3):314 – 324, 2006.

[7] Chih-Liang Chu and Sheng-Hao Fan. A novel long-travel piezoelectric-driven linear nanopositioning stage. *Precision Engineering*, 30:85 – 95, 2006.

[8] Andrew Ciesielski. *An Introduction to Rubber Technology.* Rapra Technology Limited, 1999.

[9] Peter W. Clark, Ian D. Aiken, and James M. Kelly. Ongoing studies of the foothill communities law and justice center. *Structures Congress - Proceedings*, 2:1133 – 1137, 1997.

[10] Boeing Company. *Developing Low Maintenance Rotor Hub for CH-47 Chinook.* http://www.boeing.com/news/releases/1999/newsrelease990830n.htm, 1999.

[11] Zygo Corporation. Zmi 4000 series measurement board operating manual. 2005.

[12] Martin L. Culpepper and Gordon Anderson. Design of a low-cost nano-manipulator which utilizes a monolithic, spatial compliant mechanism. *Precision Engineering*, 28(4):469 – 482, 2004.

[13] P. Donguy. Development of a helicopter rotor hub elastomeric bearing. *Journal of Aircraft*, 17:346–350, 1980.

[14] Yu Du and Ricardo Burdisso Efstratios Nikolaidis. Control of internal resonances in vibration isolators using passive and hybrid dynamic vibration absorbers. *Journal of Sound and Vibration*, 286:697–727, 2005.

[15] Fabreeka. *Isolation Technology papers.* http://www.fabreeka.com/tech/papers.htm.

[16] National Science Foundation, Committee in National Science, and Technology Council. Societal implication of nanoscience and nanotechnology. 2001.

[17] P.K. Freakley and A.R. Payne. *Theory and Practice of Engineering with Rubber.* Applied Science Publishers LTD, 1978.

[18] Alan N. Gent and Eberhard A. Meinecke. Compression, bending, and shear of bonded rubber blocks. *Polymer Engineering and Science*, 10:48–53, 1970.

[19] E.F. Göbel. *Rubber Spring Design.* Newnes-Butterworths, London, 1974.

[20] Layton C. Hale. *Principles and Techniques for Designing Precision Machines.* PhD dissertation, Massachusetts Institute of Technology, Department of Mechanical Engineering, 1999.

[21] Seymour A. Hatch. *Laminated Elastomeric Bearing Unit.* US Patent #4,365,936, 1982.

[22] Hermann A. Haus and James R. Melcher. *Electromagnetic Fields and Energy.* Prentice-Hall, 1989.

[23] Mike Holmes, Robert Hocken, and David Trumper. The long-range scanning stage: a novel platform for scanned-probe microscopy. *Precision Engineering*, vol. 24(2):191–201, 2000.

[24] Neal B. Hubbard, Martin L. Culpepper, and Larry L. Howell. Actuators for micropositioners and nanopositioners. *Applied Mechanics Review*, 59(6):324 – 34, 2006.

[25] Crosslink Technogy Inc. *Common Terms and Definitions.* http://www.crosslinktech.com/definitions.htm, 2005.

[26] Physik Instrumente. *MicroPostioning, NanaoPositioning, NanoAutomation: Solutions for Cutting-Edge Technologies.* Physik Instrument Product Catalog, 2002.

[27] Physik Instrumente. Personal communication with support engineer. February 2005.

[28] David I. G. Jones. *Handbook of Viscoelastic Vibration Damping.* John Wiley and Sons, Ltd, 2001.

[29] Won jong Kim. *High Precision Planar Magnetic Levitation.* PhD dissertation, Massachusetts Institute of Technology, Department of Electrical Engineering and Computer Science, 1997.

[30] James M. Kelly. *Earthquake-Resistant Design with Rubber.* Springer, 2nd edition, 1997.

[31] James M. Kelly and F.F. Tajirian. Testing of seismic isolation bearings for advanced liquid metal reactor prism. *Proceedings of ASME-Seismic, Shock and Vibration Isolation*, 147, 1988.

[32] P.B. Lindley. *Use of Rubber in Engineering.* Maclaren and Sons, LTD, 1966.

[33] P.B. Lindley. *Engineering Design with Natural Rubber.* Malaysian Rubber Producers' Research Association, reprinted fourth edition edition, 1978.

[34] Chris Longhurst. *The Wheel and Tyre Bible.* http://www.carbibles.com/tyre-bible.html, 2006.

[35] Xiaodong Lu. *Electromagnetically-Driven Ultra-Fast Tool Servos for Diamond Turning.* PhD dissertation, Massachusetts Institute of Technology, Department of Mechanical Engineering, 2005.

[36] Stephen J. Ludwick. Modeling and control of a six degree of freedom magnetic/fluidic motion control stage. Master's thesis, Massachusetts Institute of Technology, 1996.

[37] Augusto E. Barton Martinelli. Rubber bearings for precision positioning systems. Master's thesis, Massachusetts Institute of Technology, 2005.

[38] Richard C. Montesanti. *High Bandwidth Rotary Fast Tool Servos and a Hybrid Rotary/Linear Electromagnetic Actuator.* PhD dissertation, Massachusetts Institute of Technology, Department of Mechanical Engineering, 2005.

[39] American Society of Testing and Measurement. Astm standard a967.

[40] Edward M. Petrie. *Handbook of Adhesives and Sealants.* McGraw-Hill, first edition, 2001.

[41] E. I. Rivin. Properties and prospective applications of ultra thin layered rubber-metal laminates for limited travel bearings. *Tribology International*, 16:17–25, 1983/2.

[42] Eugene I. Rivin. *Stiffness and Damping in Mechanical Design.* CRC Press Publishing, 1999.

[43] Robert C. Rybicki and Brian Cuerden. *Elastomeric Bearing for Helicopter Rotor.* US Patent #4,142,833, 1979.

[44] Dale W. Schubert, Andrew Michael Beard, Steven Frank Shedd, Jr. Marion Richard Earles, and Andreas H. Von Flotow. *Stiff Actuator Active Vibration Isolation System.* US Patent #5,660,255, 1997.

[45] R. Singh, G. Kim, and P. V. Ravindra. Linear analysis of automotive hydro-mechanical mount with emphasis on decoupler characteristics. *Journal of Sound and Vibration*, 158:219–243, 1992.

[46] Stuart T. Smith and Richard M. Seugling. Sensor and actuator considerations for precision, small machines. *Precision Engineering*, 30(3):245 – 264, 2006.

[47] Philip A. Studer. A practical magnetic bearing. *IEEE Transactions on Magnetics*, NAG-13.

[48] Philip A. Studer. *Spring Neutralized Magnetic Vibration Isolator.* US Patent #4,710,656, 1987.

[49] Jr. Andrew B. Sweeney, Shannon K.; Swoyer. Flexible dual-rate coupling, November 1996.

[50] ADE Technology. Personal communication with support engineer. October 2005.

[51] Peter E. Tenzer and Ridha Ben Mrad. A systematic procedure for the design of piezoelectric inchworm precision positioners. *IEEE/ASME Transactions on Mechatronics*, 9(2):427 – 435, 2004.

[52] David L. Trumper. *Magnetic Suspension Techniques for Precision Motion Control.* PhD dissertation, Massachusetts Institute of Technology, Department of Electrical Engineering and Computer Science, 1990.

[53] Hsiang-Chuan Tsai and Shaw-Jiun Hsueh. Mechanical properties of isolation bearings identified by a viscoelastic model. *International Journal of Solids and Structures*, Volume 38.

[54] Wanjun Wang and Tian He. A high precision micropositioner with five degrees of freedom based on an electromagnetic driving principle. *Review of Scientific Instruments*, 67(1):312–317, 1996.